UNIVERSITY OF SOUTHERN QUEENSLAND

INTEGATED RADIAL BASIS FUNCTION METHODS FOR NEWTONIAN AND NON-NEWTONIAN FLUID FLOWS

A dissertation submitted by

DAO HO-MINH

B.Eng. (Hon.), Ho-Chi-Minh City University of Technology, Vietnam, 2000

M.Eng., Ho-Chi-Minh City University of Technology, Vietnam, 2003

For the award of the degree of

Doctor of Philosophy

February 2011

Dedication

To my family and to the memory of my father

Certification of Dissertation

I certify that the idea, experimental work, results and analyses, software and conclusions reported in this dissertation are entirely my own effort, except where otherwise acknowledged. I also certify that the work is original and has not been previously submitted for any other award.

Dao Ho-Minh, Candidate	Date

ENDORSEMENT

Associate Prof. Nam Mai-Duy, Principal supervisor	Date
Prof. Thanh Tran-Cong, Co-supervisor	Date

Acknowledgments

Firstly, I would like to express my greatest gratitude to my supervisors, Associate Prof. Nam Mai-Duy and Prof. Thanh Tran-Cong, for their instructive guidance and useful suggestions. I am also deeply grateful for their helps in editing my works and their patience over past few years.

Secondly, I wish to acknowledge the financial support provided by the University of Southern Queensland (USQ) (a USQ Research Excellence scholarship), Faculty of Engineering and Surveying (FoES) (a FoES scholarship supplement), and Computational Engineering and Science Research Centre (CESRC) (a CESRC scholarship supplement).

Next, I would like to extend my thanks to my former lecturers at Ho-Chi-Minh City University of Technology for the knowledge and encouragement that I received from them during my undergraduate study. Especially, I am grateful to Associate Prof. Le Thi Minh Nghia for introducing me to an opportunity to study for a PhD degree at USQ.

Last but not least, I would like to thank my mother and my sisters for their boundless love and unconditional supports.

Notes to Readers

Attached to this thesis is the CD-ROM containing the following files:

1. thesis.pdf: An electronic version of this thesis
2. Movie_Cavity_Isotherms.wmv: An animation showing the evolution of temperature field (Chapter 3, Problem 2: Natural convection in a square slot)
3. Movie_Cavity_Streamlines.wmv: An animation showing the evolution of streamfunction field (Chapter 3, Problem 2: Natural convection in a square slot)
4. Movie_Annulus_Isotherms.wmv: An animation showing the evolution of temperature field (Chapter 3, Problem 3: Natural convection in a concentric annulus)
5. Movie_Annulus_Streamlines.wmv: An animation showing the evolution of streamfunction field (Chapter 3, Problem 3: Natural convection in a concentric annulus)

Abstract

In this PhD thesis, one-dimensional integrated radial basis function networks (1D-IRBFNs) are further developed for the simulation of viscous and viscoelastic flows in two dimensions. The thesis consists of two main parts.

In the first part, 1D-IRBFNs are incorporated into the Galerkin formulation to simulate viscous flows. The governing equations are taken in the streamfunction-vorticity formulation and in the streamfunction formulation. Boundary conditions are effectively imposed with the help of the integration constants. The proposed 1D-IRBFN-based Galerkin methods are validated through the numerical simulation of several benchmark test problems including free convection in a square slot and in a concentric annulus.

In the second part, 1D-IRBFNs are incorporated into the Galerkin and collocation formulations to simulate viscoelastic flows. The momentum and continuity equations are taken in the streamfunction-vorticity formulation and two types of fluid, namely Oldroyd-B and CEF models, are considered. Flows in a rectangular duct and in straight and corrugated tubes are simulated to validate the proposed 1D-IRBFN-based Galerkin/Collocation methods.

Main attractive features of the proposed methods include (i) easy implementation; (ii) avoidance of the reduction in convergence rate caused by differentiation; and (iii) effective treatment of derivative boundary conditions. Numerical results show that the proposed methods are stable, high-order accurate and converge well. This study further demonstrates the great potential of using RBFs in CFD.

Papers Resulting from the Research

Book Chapters

1. Ho-Minh, D., Mai-Duy, N. and Tran-Cong, T. (2010). "A Cartesian-grid integrated-RBF Galerkin technique". In: B. Sarler and S.N. Atluri (eds.) *Recent Studies in Meshless and Other Novel Computational Methods*. Chapter VI, pp. 87–102. Tech Science Press (ISBN 978-0-9824205-4-6).

Journal Papers

1. Ho-Minh, D., Mai-Duy, N. and Tran-Cong, T. (2009). A Galerkin-RBF approach for the streamfunction-vorticity-temperature formulation of natural convection in 2D enclosured domains. *CMES: Computer Modeling in Engineering & Sciences*, vol. 44, no. 3, pp. 219–248.

2. Mai-Duy, N., Ho-Minh, D. and Tran-Cong, T. (2009). A Galerkin approach incorporating integrated radial basis function networks for the solution of 2D biharmonic equations. *International Journal of Computer Mathematics*, vol. 86, nos. 10-11, pp. 1746–1759.

3. Ho-Minh, D., Mai-Duy, N. and Tran-Cong, T. (2010). Simulation of viscous and viscoelastic flows using a RBF-Galerkin approach. Submitted

to *Australian Journal of Mechanical Engineering*.

4. Ho-Minh, D., Mai-Duy, N. and Tran-Cong, T. (2010). Galerkin/Collocation methods based on 1D-integrated-RBFNs for viscoelastic flows. *CMES: Computer Modeling in Engineering & Sciences*, vol.70, no.3, pp. 217-252.

Conference Papers

1. Ho-Minh, D., Mai Duy, N. and Tran Cong, T. (2007). Analysis of viscoelastic flow by a radial basis function networks method. In: P. Jacobs, T. McIntyre, M. Cleary, D. Buttsworth, D. Mee, R. Clements, R. Morgan and C. Lemckert (eds). *The 16th Australasian Fluid Mechanics Conference*, Gold Coast, QLD, Australia, 3-7 December 2007. *Proceedings of The 16th Australasian Fluid Mechanics Conference* (CD), pages 1321–1327. The University of Queensland (ISBN 978-1-864998-94-8).

2. Ho-Minh, D., Mai-Duy, N. and Tran-Cong, T. (2010). A Cartesian-grid integrated-RBF method for viscoelastic flows. In: N. Khalili, S. Valliappan, Q. Li and A. Russell (eds). *The 9th World Congress on Computational Mechanics* and *The 4th Asian Pacific Congress on Computational Mechanics (WCCM/APCOM 2010)*, Sydney, Australia, 19-23/Jul/2010. *IOP Conference Series: Materials Science and Engineering*, Vol. 10, Paper No. 012210, 9 pages. IOP Publishing (ISSN 1757-899X (Online) and ISSN 1757-8981 (Print)).

3. Ho-Minh, D., Le-Cao, K., Mai-Duy, N. and Tran-Cong, T. (2010). Simulation of fluid flows at high Reynolds/Rayleigh numbers using integrated radial basis function. In: G.D. Mallinson and J.E. Cater (eds). *The 17th Australasian Fluid Mechanics Conference*, Auckland, New Zealand, 5-9/Dec/2010. *Proceedings of 17th Australasian Fluid Mechanics Conference* (CD), Paper No 139, 4 pages. The University of Auckland (ISBN: 978-0-86869-129-9).

Contents

Dedication i

Certification of Dissertation ii

Acknowledgments iii

Notes to Readers iv

Abstract v

Papers Resulting from the Research vi

Acronyms & Abbreviations xiii

List of Tables xv

List of Figures xvii

Chapter 1 Introduction **1**

1.1 Overview of computational fluid mechanics 1

1.1.1 Governing equations 1

1.1.2 Discretisation methods 3

1.1.3 Radial basis function networks (RBFNs) 5

1.2 Motivation and Significance 6

1.3 Outline of the Thesis 7

Chapter 2 Reviews of the weighted residual statements and radial basis function network (RBFN) approaches **9**

2.1 Method of weighted residuals 9

2.2 Radial basis functions networks 14

2.2.1 Description 15

2.2.2 Types of RBF 17

2.3 RBFN approaches for function approximation 18

2.3.1 Differentiated RBFNs (DRBFNs) 18

2.3.2 Integrated RBFNs (IRBFNs) 20

2.4 RBFN approaches for solution of ODEs/PDEs 24

Chapter 3 1D-IRBFN-based Galerkin method for the streamfunction-vorticity formulation governing viscous flows 28

3.1 Introduction 29

3.2 Governing equations 32

3.3 1D-IRBFN-based Galerkin technique 34

3.3.1 One-dimensional IRBFN representations of the field variables 34

3.3.2 Derivation of computation boundary conditions for the vorticity 39

3.3.3 Galerkin discretisations of the PDEs 43

3.3.4 Solution procedure 45

3.4 Numerical results 46

3.4.1 Problem 1 (vorticity boundary condition) 47

3.4.2 Problem 2: Natural convection in a square slot 50

3.4.3 Problem 3: Natural convection in a concentric annulus . 61

3.5 Concluding Remarks 68

Chapter 4 1D-IRBFN-based Galerkin method for the stream-function formulation governing viscous flows 69

4.1 Introduction 70

4.2 Governing equations 72

4.3 1D-IRBFN-based Galerkin technique 73

4.3.1 One-dimensional IRBFN representations of the field variables 73

4.3.2 Imposition of boundary conditions 78

4.3.3 Galerkin discretisations 81

4.4 Numerical results 83

4.4.1 Problem 1: Equidistant interpolating points (Runge's phenomenon) 84

4.4.2 Problem 2: Extra information 86

4.4.3 Problem 3: Linear test problem 88

4.4.4 Problem 4: Nonlinear buoyancy-driven flow 91

4.5 Concluding Remarks 98

Chapter 5 1D-IRBFN-based Galerkin/Collocation methods for the streamfunction-vorticity formulation governing viscoelastic flows 99

5.1 Introduction 100

5.2 Governing equations 102

5.3 Galerkin/Collocation 1D-RBFN technique 105

5.3.1 One-dimensional IRBFN representation of the field variables 106

5.3.2 Imposition of boundary conditions 109

5.3.3 Incorporating 1D-IRBFNs into Galerkin and point-collocation formulations 111

5.4 Numerical results 114

5.4.1 Problem 1: Fully-developed flows of CEF fluid in rectangular ducts 115

5.4.2 Problem 2: Fully-developed flows of Oldroyd-B fluid in circular tubes 124

5.4.3 Problem 3: Flows of Oldroyd-B fluid in corrugated tubes 128

5.5 Concluding remarks 141

Chapter 6 Conclusions 142

Appendix A Antiderivatives of multiquadric function in one dimension 145

Appendix B Iterative methods for nonlinear equations 147

B.1 Picard methods 148

B.2 Newton-based methods 148

B.3 Time-marching methods 149

Acronyms & Abbreviations

1D-IRBFN	One-dimensional Indirect/Integrated Radial Basis Function Network
BEM	Boundary Element Method
CEF	Criminale-Ericksen-Filbey model
CFD	Computational Fluid Dynamics
DAMs	Diffuse Approximation Methods
DOF	Degrees of Freedom
DRBEM	Dual Reciprocity Boundary Element Method
DRBFN	Direct Radial Basis Function Network
DSC	Discrete Singular Convolution
EEME	Explicitly Elliptic Momentum Equation
EFG	Element-free Galerkin
EVSS	Elastic Viscous Stress Splitting
FCC	Fourier-Chebyshev Collocation
FDM	Finite Difference Method
FEM	Finite Element Method
FVM	Finite Volume Method
GFEM	Galerkin Finite Element Method
IRBFN	Indirect/Integrated Radial Basis Function Network
LHS	Left Hand Side
LRPIM	Local Radial Point Interpolation Method

MLP	Multilayer Perceptron
MLPG	Meshless Local Petrov-Galerkin method
MPTT	Modified Phan-Thien–Tanner model
MQ	Multiquadric
MWR	Method of Weighted Residuals
NN	Neural Networks
ODE	Ordinary Differential Equation
PCFD	Pseudo-spectral Cylindrical Finite Difference method
PDE	Partial Differential Equation
PSFD	Pseudo-Spectral Finite Difference method
PTT	Phan-Thien - Tanner model
RBF	Radial Basis Function
RBFN	Radial Basis Function Network
RBFCM	mesh-free local RBF Collocation Method
RBF-DQM	RBF-based Differential Quadrature Method
RHS	Right Hand Side
RKPM	Reproducing Kernel Particle Method
SM	Spectral Method
SPH	Smooth Particle Hydrodynamics
UCM	Upper-convected Maxwell

List of Tables

1.1 Definition of constants in several differential constitutive equations. It is noted that λ is the relaxation time, and ξ and ε are the material parameters. 3

3.1 Problem 1 (homogeneous boundary conditions): N_e errors of the solution ψ and ω. Notice that a(-b) means $a \times 10^{-b}$ 49

3.2 Problem 1 (inhomogeneous boundary conditions): N_e errors of the solution ψ and ω. Notice that a(-b) means $a \times 10^{-b}$ 49

3.3 Problem 2, natural convection flow in a square slot: Comparison of the Galerkin-IRBFN results with the benchmark solution of Davis (1983) for $10^3 \leq Ra \leq 10^6$ and $Pr = 0.71$ 53

3.4 Problem 2, natural convection flow in a square slot: Comparison of the Galerkin-IRBFN results with those of other techniques for the two highest values of Ra 57

3.5 Problem 3, natural convection flow in an annulus: Convergence of the computed average equivalent conductivities with grid refinement for $10^2 \leq Ra \leq 7 \times 10^4$. 64

4.1 Problem 3, linear problem: Error $N_e(\psi)$ versus the number of RBFs N. 90

4.2 Problem 4: Natural convection flow, 51×51. 94

5.1 Problem 2: Grid-convergence study at $We = 9$. 126

5.2 Problem 3, Newtonian fluid: Comparison of the flow resistance $f\mathrm{Re}$ for $Re = 0$ computed for several values of ε and N 132

5.3 Problem 3, Newtonian fluid, $\varepsilon = 0.3$, $N = 0.16$: comparison of the flow resistance $f\mathrm{Re}$ for a wide range of Re 133

List of Figures

2.1 Structure of RBFN 15

2.2 Plots of RBFs: one-dimensional version of (2.28) through (2.30). The centre is located at $x = 0$ and the value of a is chosen to be 1. 17

3.1 Problem 2, natural convection flow in a square slot: geometry definition, boundary conditions and discretisation. Note that $\partial\psi/\partial x = \partial\psi/\partial y = 0$ are used to compute the boundary conditions for ω. 50

3.2 Problem 2, natural convection flow in a square slot: Contour plots for the ψ variable at four different values of Ra using a grid of 51×51. Each plot draws 21 contour lines whose values vary uniformly from the minimum to maximum values. 54

3.3 Problem 2, natural convection flow in a square slot: Contour plots for the ω variable at four different values of Ra using a grid of 51×51. Each plot draws 21 contour lines whose values vary uniformly from the minimum to maximum values. 55

3.4 Problem 2, natural convection flow in a square slot: Contour plots for the T variable at four different values of Ra using a grid of 51×51. Each plot draws 21 contour lines whose values vary uniformly from the minimum to maximum values. 56

3.5 Problem 2, natural convection flow in a square slot: Contour plots for the ψ, ω and T variables at $Ra = 10^7$ using a grid of 91×91. Iso-values used in these plots are the same as those in (Quéré, 1991). 58

3.6 Problem 2, natural convection flow in a square slot: Contour plots for the ψ, ω and T variables at $Ra = 10^8$ using a grid of 91×91. Iso-values used in these plots are the same as those in (Quéré, 1991). 59

3.7 Problem 2, natural convection flow in a square slot: Variations of the local Nusselt number along the left and right walls. 60

3.8 Problem 3, natural convection flow in an annulus: domain of interest (upper figure), computational domain (lower figure), boundary conditions and discretisation 63

3.9 Problem 3, natural convection flow in an annulus: Contour plots for the ψ (left) and T (right) variables at $Ra = 10^3$ and $Ra = 3 \times 10^3$ using a grid of 51×51. 65

3.10 Problem 3, natural convection flow in an annulus: Contour plots for the ψ (left) and T (right) variables at $Ra = 6 \times 10^3$ and $Ra = 10^4$ using a grid of 51×51. 66

3.11 Problem 3, natural convection flow in an annulus: Contour plots for the ψ (left) and T (right) variables at $Ra = 5 \times 10^4$ and $Ra = 7 \times 10^4$ using a grid of 51×51. 67

4.1 Problem 1, function interpolation, $f(x) = 1/(1 + 25x^2)$, $-1 \leq x \leq 1$: Performances of polynomial and IRBFN interpolants using equally-spaced interpolating points denoted by $\circ$. The latter does not suffer from Runge's phenomenon. It is noted that the approximate function is plotted using 501 uniformly-distributed points. 85

4.2 Problem 2, function interpolation, $f(x) = \sin(2\pi x)$, $0 \leq x \leq 1$: Error versus the grid spacing. The domain is discretised using uniform grids made of 3 to 101 points with increment of 2. Errors are computed at a test grid of 501 uniformly-distributed points. The DRBFN's N_e is $O(h^{1.67})$ and $O(h^{1.62})$ for case 1 and 2, respectively. The corresponding IRBFN's N_e is $O(h^{3.93})$ and $O(h^{3.67})$. It is noted that the above figures have the same scaling. 87

4.3 Problem 3: Exact solution. 89

4.4 Problem 4, natural convection flow, $Ra = 10^7$: Convergence for the temperature field with respect to the MQ centre's density refinement. Iso-values used are $(-0.5 : 0.1 : 0.5)$ which are the same as those in (Quéré, 1991). The plot at 51×51 has a similar structure to that of the benchmark spectral result (Quéré, 1991). 95

4.5 Problem 4, natural convection flow, $Ra = 10^7$: Convergence for the stream function field with respect to the MQ centre's density refinement. Iso-values used are $-1/\sqrt{Pr}(0, 0.0005, 0.002, 0.004, 0.006, 0.007, 0.0075, 0.0079, 0.0083, 0.0088, 0.0092, 0.0094)$ which are the same as those in (Quéré, 1991). The plot at 51×51 has a similar structure to that of the benchmark spectral result (Quéré, 1991). 96

4.6 Problem 4, natural convection flow, 51×51: Velocity profiles on the horizontal and vertical centrelines for various Ra values. . . 97

5.1 Problem 1: Convergence behaviour of the streamfunction field with respect to grid refinement. 118

5.2 Problem 1: Convergence behaviour of the vorticity field with respect to grid refinement. 119

5.3 Problem 1: Streamlines of the secondary flow in one quarter of the cross section for several values of the aspect ratio. 120

5.4 Problem 1: Contour plots for the vorticity in one quarter of the cross-section computed for several values of the aspect ratio. . . 121

5.5 Problem 1: Contour plots for the primary velocity in one quarter of the cross-section computed for several values of the aspect ratio.122

5.6 Problem 1: Contour plots for the second normal stress difference in one quarter of the cross-section computed for several values of the aspect ratio. 123

5.7 Problem 2: Profiles of velocity and stress on the middle plane $z = 0.5$ computed at several values of We using grid of 21×21. It is noted that u_z and T_{rz} are independent of We and their corresponding computed results are indistinguishable. 127

5.8 Problem 3: problem definition 134

5.9 Problem 3, Newtonian fluid, $\varepsilon = 0.5$, $N = 0.5$, grid size of 41×41: Streamlines for $Re = 0$. Iso-values used are (0, 0.02, 0.06, 0.1, 0.14, 0.15, 0.159). For $0.159157 \leq \psi \leq 0.15933$, an increment of 5.767×10^{-5} is used to resolve the recirculation region, which are the same as those in (Pilitsis and Beris, 1991). 135

5.10 Problem 3, Newtonian fluid, $\varepsilon = 0.3$, $N = 0.16$, grid size of 41×41: Contour plots of the streamfunction and vorticity for a wide range of Re. 136

5.11 Problem 3, Oldroyd-B fluid, $\varepsilon = 0.1$, $N = 0.5$: Contour plots for u_r at $We = 2$ using several grids. The maximum and minimum values of u_r and their locations are also displayed. 137

5.12 Problem 3, Oldroyd-B fluid, $\varepsilon = 0.1$, $N = 0.5$: Contour plots for T_{rz} at four values of We using a grid of 41×41. The maximum and minimum values of T_{rz} and their locations are also displayed. 138

5.13 Problem 3, Oldroyd-B fluid, $\varepsilon = 0.1$, $N = 0.5$: Contour plots for T_{zz} at $We = 6$ using grids of 31×31 and 41×41. The maximum and minimum values of T_{zz} and their locations are also displayed. 139

5.14 Problem 3, Oldroyd-B fluid: The variation of the flow resistance with respect to the Weissenberg number for two geometrical configurations. 140

Chapter 1

Introduction

The aim of this chapter is to give an introduction to this PhD project. It begins with an overview of the numerical study of the motion of Newtonian and non-Newtonian fluids. We then present the motivation and significance of the research project. The chapter ends with the thesis outline.

1.1 Overview of computational fluid mechanics

1.1.1 Governing equations

Fluid flows, which are characterised by the evolution of physical properties such as temperature, stress, velocity, mass and energy, can be mathematically described by a set of partial differential equations (PDEs) together with a set of boundary conditions.

Conservation equations: The conservation laws for momentum and mass of

an incompressible fluid lead to

$$\rho\left(\frac{\partial \boldsymbol{u}}{\partial t}+\boldsymbol{u}\cdot\nabla\boldsymbol{u}\right) = \nabla\cdot\boldsymbol{\sigma}+\mathbf{f}, \qquad \mathbf{x}\in\Omega, \tag{1.1}$$

$$\nabla\cdot\boldsymbol{u} = 0, \qquad \mathbf{x}\in\Omega, \tag{1.2}$$

where $\boldsymbol{u}$ is the velocity vector, $\mathbf{f}$ the body force vector per unit volume, ρ the fluid density, $\boldsymbol{\sigma}$ the Cauchy stress tensor, t the time, $\mathbf{x}$ the position vector and Ω the domain of interest.
The stress tensor can be decomposed into

$$\boldsymbol{\sigma} = -p\boldsymbol{I}+\boldsymbol{\tau}, \tag{1.3}$$

where p is the pressure, $\boldsymbol{I}$ the unit tensor and $\boldsymbol{\tau}$ the extra stress tensor.

For non-isothermal problems, a set of the field equations is completed with the following energy equation

$$\rho c\left(\frac{\partial T}{\partial t}+\boldsymbol{u}\cdot\nabla T\right) = \nabla\cdot(\boldsymbol{\sigma}\cdot\boldsymbol{u})-\nabla\cdot\boldsymbol{q}+\boldsymbol{f}\cdot\boldsymbol{u}+r, \tag{1.4}$$

where T is the temperature, $\boldsymbol{q}$ the heat flux vector, c the heat capacity, r the heat source per unit of volume.

Constitutive equations: The process of establishing the mathematical relationship between the extra stress tensor $\boldsymbol{\tau}$ and the kinematic tensors leads to the constitutive equations.

One can split the tensor $\boldsymbol{\tau}$ as

$$\boldsymbol{\tau} = 2\mu_n\boldsymbol{d}+\boldsymbol{\tau}_v, \tag{1.5}$$

where $\boldsymbol{\tau}_v$ is the extra stress due to viscoelasticity, μ_n the "Newtonian-contribution"/solvent

viscosity and $\boldsymbol{d} = \left(\nabla \boldsymbol{u} + (\nabla \boldsymbol{u})^T\right)/2$ the strain rate. Many differential constitutive models can be written in the general form

$$a\boldsymbol{\tau}_v + \lambda_1 \overset{\nabla}{\boldsymbol{\tau}}_v + \lambda_2 \{\boldsymbol{d} \cdot \boldsymbol{\tau}_v + \boldsymbol{\tau}_v \cdot \boldsymbol{d}\} + \lambda_3 \{\boldsymbol{\tau}_v \cdot \boldsymbol{\tau}_v\} = 2\mu_p \boldsymbol{d}, \tag{1.6}$$

where μ_p is the "polymer-contribution" viscosity, $\{a, \lambda_1, \lambda_2, \lambda_3\}$ the constants defined in Table 1.1 for various viscoelastic models, and $\overset{\nabla}{\boldsymbol{\tau}}_v$ the upper-convected derivative defined as

$$\overset{\nabla}{\boldsymbol{\tau}}_v = \frac{\partial \boldsymbol{\tau}_v}{\partial t} + \boldsymbol{u} \cdot \nabla \boldsymbol{\tau}_v - (\nabla \boldsymbol{u})^T \cdot \boldsymbol{\tau}_v - \boldsymbol{\tau}_v \cdot \nabla \boldsymbol{u}. \tag{1.7}$$

Table 1.1: Definition of constants in several differential constitutive equations. It is noted that λ is the relaxation time, and ξ and ε are the material parameters.

Constitutive model	a	λ_1	λ_2	λ_3
Oldroyd-B	1	λ	0	0
Phan-Thien Tanner 1	$e^{\left(\frac{\lambda\varepsilon}{\mu_p}\mathrm{tr}(\boldsymbol{\tau}_v)\right)}$	λ	$\xi\lambda$	0
Phan-Thien Tanner 2	$1 + \frac{\lambda\varepsilon}{\mu_p}\mathrm{tr}\,(\boldsymbol{\tau}_v)$	λ	$\xi\lambda$	0
Giesekus-Leonov	1	λ	0	$-\frac{\lambda}{2\mu_p}$

When $\mu_n = 0$, the Oldroyd-B model reduces to a Upper-convected Maxwell (UCM) model ($\boldsymbol{\tau} = \boldsymbol{\tau}_v$).

1.1.2 Discretisation methods

Principal discrete methods for solving (1.1), (1.2) and (1.4) include finite difference (FDMs), finite element (FEMs), finite volume (FVMs) and boundary element (BEMs) methods. These methods generally require the replacement of the problem domain with a set of small subregions (elements) that are connected through a fixed topology.

FDMs have a long history (e.g. Crochet et al., 1984). They are easy to program

and work well for regular geometries. However, for irregular domains, one needs to apply coordinate transformations to convert them into regular ones. Due to this requirement, FDMs are seen to be less attractive than other methods. On the contrary, FEMs and FVMs are capable of handling complex geometries in a direct manner. FEMs have been well developed for the simulation of viscous and viscoelastic flows (e.g. Zienkiewicz and Taylor, 1991; Reddy and Gartling, 1994). In comparison with FEMs, FVMs can be seen to be more stable and efficient (time and memory) (Chang and Yang, 2001; Araujo et al., 2009). Since conventional FEMs and FVMs rely on low-order interpolation schemes (e.g. linear and quadratic variations), one generally needs to use a large number of elements for an accurate simulation. This drawback can make these methods inefficient in solving large-scale problems. Other disadvantages include (i) less accurate approximations for high-order derivatives such as velocity gradients; and (ii) difficulty in handling problems with moving boundaries and transient free surfaces. On the other hand, many fluid flow problems have been simulated using BEMs (Brebbia et al., 1984). For homogeneous problems, only the boundaries (lines/surfaces) of the domain have to be discretised, resulting in a simple preprocessing. For inhomogeneous problems, special treatments are required to transform volume integrals into boundary integrals (Brebbia et al., 1984). Clearly, the discretisation of lines/surfaces is much simpler than that of the whole domain. This is the main reason why BEMs become more attractive for certain 3D problems with complex geometry. However, they do not work well for highly-nonlinear problems, e.g. high Reynolds number and Weissenberg number flows including the steady case (Tanner and Xue, 2002).

Recently, mesh-free/meshless/element-free techniques have been developed. As the name implies, these techniques are based on a set of nodes that can be randomly distributed in a domain without any connectivity required. Examples of meshless methods include smooth particle hydrodynamics (SPH) methods (e.g. Monaghan, 1990, 1994; Ellero and Tanner, 2005), element-free Galerkin (EFG) methods (e.g. Belytschko et al., 1994; Huerta et al., 2004), reproducing

kernel particle methods (RKPM) (e.g. Liu et al., 1995), and meshless local Petrov-Galerkin (MLPG) methods (e.g. Atluri and Zhu, 1998; Atluri et al., 2004; Sladek et al., 2004, 2007). A comprehensive survey of mesh-free methods can be found in (Belytschko et al., 1996; Liu and Gu, 2005).

1.1.3 Radial basis function networks (RBFNs)

RBFNs have received a great deal of attention from both scientific and engineering research communities. RBFNs, which have the property of universal approximation, are widely used for the approximation of scattered data in high dimensions (Franke, 1982; Wendland, 1995). Unlike high-order algebraic polynomials, RBFNs do not suffer from the Runge phenomenon (Fornberg and Zuev, 2007; Mai-Duy et al., 2009; Boyd, 2010). The application of RBFNs in the context of point collocation for solving ordinary differential equations (ODEs) and PDEs was first reported by Kansa in 1990 (Kansa, 1990a). Since then, there have been many RBF publications, showing RBFN-based methods as an alternative to conventional methods. Higher levels of accuracy and efficiency were reported in many cases (e.g. Li et al., 2003; Cheng et al., 2003).

There are two basic approaches, namely direct and indirect, to construct the RBF approximations, leading to differentiated RBFNs (DRBFNs) (Kansa, 1990a) and integrated RBFNs (IRBFNs) (Mai-Duy, 2001; Mai-Duy and Tran-Cong, 2001a,b, 2003), respectively. In the former, a function is first represented by an RBFN which is then differentiated to obtain approximate expressions for its derivative functions. In the latter, the highest-order derivatives in the ODE/PDE are first decomposed into RBFs, and lower-order derivatives and the function itself are then obtained through integration. Through pioneering numerical experiments (e.g. Mai-Duy and Tran-Cong, 2001a, 2003, 2005) and subsequent theoretical analyses (e.g. Ling and Trummer, 2004; Sarra, 2006), it was shown that IRBFN collocation methods are more accurate than DRBFN

ones for both the representation of functions and the solution of ODEs/PDEs.

RBFN-based methods have been developed into their global and local versions. For global RBF methods (e.g. Kansa, 1990a,b; Mai-Duy and Tran-Cong, 2001a), the RBF approximations for the field variable at a nodal point involve every node within the problem domain. Very accurate results were reported. However, the use of these methods is limited to data sets up to a few hundreds of nodes only due to the fact that the RBF interpolation matrix is fully populated and its condition number grows rapidly with the increase of the RBF width and the number of RBFs (Schaback, 1995). For local RBF methods (e.g. Lee et al., 2003; Šarler and Vertnik, 2006; Divo and Kassab, 2007, 2008; Mai-Duy and Tran-Cong, 2009b; Stevens et al., 2009), one uses only a few nodal points to construct the approximations for the field variable at a node, resulting in a sparse system matrix. Thus, local RBF solutions were reported for discrete models with a much larger number of nodes. Further details can be found in a comprehensive survey of local RBF methods for transport phenomena (Šarler, 2007) and a comparative study of their use for diffusion-reaction equations (Yao, Islam and Šarler, 2010). In the context of IRBFNs, collocation schemes, based on one-dimensional (1D) IRBFNs and Cartesian grids, for the solution of 2D elliptic PDEs were reported in, for instance, (Mai-Duy and Tran-Cong, 2007). The 1D-IRBFN approximations at a grid node use only nodes that lie on the grid lines intersecting at that node rather than the whole set of nodes. As a result, the construction process is conducted for a series of small matrices rather than for a large single matrix.

1.2 Motivation and Significance

From the above survey, it can be seen that the development of RBFNs for the solution of ODEs/PDEs is a relatively new research area. Unlike low-order polynomials, RBFNs have the ability to produce an exponential rate of convergence

(i.e. spectral accuracy). In contrast to high-order (Chebyshev) polynomials, they can work well on uniformly-gridded and scattered data. Integrated RBFNs have several advantages over differentiated RBFNs. The use of integration to construct the approximations helps avoid the problem of reduced convergence rate caused by differentiation as well as provides a powerful means of implementing derivative boundary conditions. The use of IRBFNs constructed in one dimension for the solution in two or higher dimensions facilitates the employment of a much larger number of nodes. For most works reported, RBFNs are introduced as trial functions in the point collocation and there are so few RBF results for the simulation of non-Newtonian fluid flows.

In this research project, we have developed new numerical methods based on 1D-IRBFNs for the simulation of viscous and viscoelastic flows: (i) 1D-IRBFNs are introduced for the first time as the trial functions in the Galerkin formulation; and (ii) viscoelastic flows are simulated by Galerkin/collocation methods incorporating local RBF approximators (i.e. 1D-IRBFNs).

1.3 Outline of the Thesis

The thesis is comprised of six chapters which are organised as follows.

- Chapter 2 gives a review of weighted residual approaches including point-collocation and Galerkin formulations, and radial basis function networks including differentiated and integrated networks. A discussion on the basic application of RBFNs for numerical solution of ODEs/PDEs is also given.
- Chapter 3 presents the development of 1D-IRBFN-based Galerkin method for the discretisation of the streamfunction-vorticity formulation (a set of two second-order PDEs) governing the motion of a Newtonian fluid. Natural convection defined on 2D enclosured domains are simulated to validate the proposed method.

- Chapter 4 presents a further development of the 1D-IRBFN-based Galerkin method for the discretisation of the streamfunction formulation (fourth-order PDE) governing the motion of a Newtonian fluid. Linear and non-linear problems, including a benchmark buoyancy-driven flow in a square slot, are considered.

- Chapter 5 presents the development of 1D-IRBFN-based Galerkin/Collocation methods for the discretisation of the streamfunction-vorticity formulation governing the motion of a viscoelastic fluid. Flows in rectangular ducts and in straight and corrugated tubes are considered.

- Chapter 6 gives some concluding remarks and identifies possible future research directions.

Chapter 2

Reviews of the weighted residual statements and radial basis function network (RBFN) approaches

In this chapter, we shall attempt to give brief reviews of the weighted residual statements and RBFNs for solving ODEs/PDEs. Galerkin and point-collocation formulations, and one-dimensional integrated RBFNs will be used in subsequent chapters as basic tools.

2.1 Method of weighted residuals

Method of weighted residuals (MWR), a general approximation framework for solving ODEs/PDEs, exists for a long time. Many discretisation methods (e.g. FDMs, FEMs and BEMs) can be seen as special cases of the weighted residual statement. A review of MWR including the discussion on how principal numer-

ical methods can be derived from MWR can be found in (Brebbia et al., 1984; Zienkiewicz and Taylor, 1991; Liu and Gu, 2005).

We consider a linear boundary value problem governed by the following ODE/PDE

$$\mathcal{L}\left(\widetilde{u}(\mathbf{x})\right) = \bar{b}, \qquad \mathbf{x} \in \Omega, \tag{2.1}$$

and the boundary conditions of the form

$$\mathcal{Q}\left(\widetilde{u}(\mathbf{x})\right) = \bar{q}, \qquad \mathbf{x} \in \Gamma_{\mathcal{Q}}, \tag{2.2}$$

$$\mathcal{U}\left(\widetilde{u}(\mathbf{x})\right) = \bar{u}, \qquad \mathbf{x} \in \Gamma_{\mathcal{U}}, \tag{2.3}$$

where $\mathcal{L}$ is a prescribed differential operator; $\mathcal{U}$ and $\mathcal{Q}$ prescribed operators that represent Dirichlet and Newmann boundary condition types, respectively; $\mathbf{x}$ the position vector; $\widetilde{u}$ the field variable (scalar function); $\bar{b}$, $\bar{q}$ and $\bar{u}$ given functions; Ω the problem domain; Γ_u the Dirichlet boundary; and Γ_q the Neumann boundary ($\Gamma_{\mathcal{U}}$ and $\Gamma_{\mathcal{Q}}$ constitute the boundary of Ω, i.e. $\Gamma = \Gamma_{\mathcal{U}} \cup \Gamma_{\mathcal{Q}}$).

The exact solution $\widetilde{u}$ can be approximated by

$$\widetilde{u}(\mathbf{x}) \approx u(\mathbf{x}) = \sum_{i=1}^{N} \alpha_i \phi_i(\mathbf{x}), \tag{2.4}$$

where u is an approximation to $\widetilde{u}$, $\{\alpha_i\}_{i=1}^{N}$ the set of unknown coefficients, $\{\phi_i(\mathbf{x})\}_{i=1}^{N}$ the set of trial/basis functions and N the number of trial/basis functions. To find $u(\mathbf{x})$, one can substitute (2.4) into the governing equation (2.1) and boundary conditions (2.2)-(2.3). Because (2.4) is approximate, this substitution process produces errors or residual functions ($R_{\mathcal{L}}$, $R_{\mathcal{Q}}$ and $R_{\mathcal{U}}$) which are

defined by

$$R_{\mathcal{L}} = \mathcal{L}\left(u(\mathbf{x})\right) - \bar{b}, \tag{2.5}$$

$$R_{\mathcal{Q}} = \mathcal{Q}\left(u(\mathbf{x})\right) - \bar{q}, \tag{2.6}$$

$$R_{\mathcal{U}} = \mathcal{U}\left(u(\mathbf{x})\right) - \bar{u}. \tag{2.7}$$

The unknown coefficients α_i can then be found by constructing a scheme to minimise the following statement

$$\int_{\Omega} W R_{\mathcal{L}}(\mathbf{x}) d\Omega + \int_{\Gamma_{\mathcal{Q}}} V R_{\mathcal{Q}}(\mathbf{x}) d\Gamma_{\mathcal{Q}} + \int_{\Gamma_{\mathcal{U}}} Y R_{\mathcal{U}} d\Gamma_{\mathcal{U}} = 0, \tag{2.8}$$

or

$$\int_{\Omega} W\left(\mathcal{L}\left(u(\mathbf{x})\right) - \bar{b}\right) d\Omega + \int_{\Gamma_{\mathcal{Q}}} V\left(\mathcal{Q}\left(u(\mathbf{x})\right) - \bar{q}\right) d\Gamma_{\mathcal{Q}} + \int_{\Gamma_{\mathcal{U}}} Y\left(\mathcal{U}\left(u(\mathbf{x})\right) - \bar{u}\right) d\Gamma_{\mathcal{U}} = 0, \tag{2.9}$$

where W, V and Y are weighting functions to be chosen.

Equation (2.9) is the general form of MWR. The purpose of MWR is thus to use the weighting functions W, V and Y to control the distribution of the residuals over the domain and on the boundary ($R_{\mathcal{L}}$ in Ω, $R_{\mathcal{Q}}$ on $\Gamma_{\mathcal{Q}}$ and $R_{\mathcal{U}}$ on $\Gamma_{\mathcal{U}}$). It can be seen that, through MWR, the original ODE/PDE is replaced with a set of integral equations. Generally, the trial/basis functions in (2.4) are chosen to satisfy Dirichlet boundary conditions. In this case, the third term in (2.9) vanishes and the MWR statement reduces to

$$\int_{\Omega} W\left(\mathcal{L}\left(u(\mathbf{x})\right) - \bar{b}\right) d\Omega + \int_{\Gamma_{\mathcal{Q}}} V\left(\mathcal{Q}\left(u(\mathbf{x})\right) - \bar{q}\right) d\Gamma_{\mathcal{Q}} = 0. \tag{2.10}$$

In principle, the weighting functions W and V can be chosen from any set

of linearly independent functions. The choice of W and V leads to different numerical approximation methods. Below are four typical formulations.

Galerkin formulation:

The weighting functions are chosen from the set of trial functions, i.e.

$$W_i = \phi_i(\mathbf{x}), \tag{2.11}$$

$$V_i = -\phi_i(\mathbf{x}). \tag{2.12}$$

Equation (2.10) thus becomes

$$\int_\Omega \phi_i(\mathbf{x}) \left(\mathcal{L}(u(\mathbf{x})) - \bar{b}\right) d\Omega - \int_{\Gamma_\mathcal{Q}} \phi_i(\mathbf{x}) \left(\mathcal{Q}(u(\mathbf{x})) - \bar{q}\right) d\Gamma_\mathcal{Q} = 0. \tag{2.13}$$

The Galerkin approach has the following advantages: (i) the errors are minimised in an average sense; (ii) the system matrix is usually symmetric; and (iii) the Galerkin approach leads to a formulation which is the same as that obtained by the energy principle. This formulation is widely used in, e.g., FEMs and BEMs. If the weighting functions W_i chosen do not come from $\{\phi_i(\mathbf{x})\}_{i=1}^N$, the corresponding formulation is called the Petrov-Galerkin approach.

Point-collocation formulation:

The weighting functions are chosen as the Dirac delta function

$$W_i = \delta(\mathbf{x} - \mathbf{x}_i), \tag{2.14}$$

$$V_i = \delta(\mathbf{x} - \mathbf{x}_i). \tag{2.15}$$

Substitution of (2.14)-(2.15) into (2.10) yields

$$\int_{\Omega} \delta(\mathbf{x}-\mathbf{x}_i) \left(\mathcal{L}\left(u(\mathbf{x})\right) - \bar{b} \right) d\Omega + \int_{\Gamma_{\mathcal{Q}}} \delta(\mathbf{x}-\mathbf{x}_i) \left(\mathcal{Q}\left(u(\mathbf{x})\right) - \bar{q} \right) d\Gamma_{\mathcal{Q}} = 0, \quad (2.16)$$

or

$$\mathcal{L}\left(u(\mathbf{x}_i)\right) - \bar{b} = 0, \quad \mathbf{x}_i \in \Omega, \quad (2.17)$$

$$\mathcal{Q}\left(u(\mathbf{x}_i)\right) - \bar{q} = 0, \quad \mathbf{x}_i \in \Gamma_{\mathcal{Q}}. \quad (2.18)$$

It can be seen that the residuals are simply forced to be zero at a set of points (collocation points). This formulation requires less computational effort to form the system matrix than the Galerkin formulation. However, one should pay attention to the distribution of collocation points in order to achieve the optimal accuracy for an approximate solution (Brebbia et al., 1984).

Subdomain-collocation formulation:

The weighting function is chosen as

$$W_i = \begin{cases} 1, & \text{inside} \quad \Omega_i, \\ 0, & \text{outside} \quad \Omega_i, \end{cases} \quad (2.19)$$

where Ω_i is a subregion of the domain Ω. It is noted that Ω_is are usually non-overlapping and Ω is the union of all Ω_i.

Equation (2.10) can be rewritten as

$$\int_{\Omega_i} \left(\mathcal{L}\left(u(\mathbf{x})\right) - \bar{b} \right) d\Omega = 0, \quad \mathbf{x} \in \Omega_i, \quad (2.20)$$

$$\mathcal{Q}\left(u(\mathbf{x}_i)\right) - \bar{q} = 0, \quad \mathbf{x}_i \in \Gamma_{\mathcal{Q}}. \quad (2.21)$$

It can be seen that the residual for the PDE/ODE is forced to be zero over each and every element of a set of subregions and the residual for the boundary condition is forced to be zero at a set of collocation points on $\Gamma_{\mathcal{Q}}$.

Least squares formulation:

The weighting functions are chosen to be

$$W_i = \frac{\partial R_{\mathcal{L}}}{\partial \alpha_i} = \frac{\partial \mathcal{L}\left(u(\mathbf{x})\right)}{\partial \alpha_i}, \tag{2.22}$$

$$V_i = \frac{\partial R_{\mathcal{Q}}}{\partial \alpha_i} = \frac{\partial \mathcal{Q}\left(u(\mathbf{x})\right)}{\partial \alpha_i}. \tag{2.23}$$

Equation (2.10) becomes

$$\int_{\Omega} W_i R_{\mathcal{L}} d\Omega + \int_{\Gamma_q} V_i R_{\mathcal{Q}} d\Gamma_q = \int_{\Omega} \frac{\partial \mathcal{L}\left(u(\mathbf{x})\right)}{\partial \alpha_i} \left(\mathcal{L}\left(u(\mathbf{x})\right) - \bar{b}\right) d\Omega + \int_{\Gamma_{\mathcal{Q}}} \frac{\partial \mathcal{Q}\left(u(\mathbf{x})\right)}{\partial \alpha_i} \left(\mathcal{Q}\left(u(\mathbf{x})\right) - \bar{q}\right) d\Gamma_{\mathcal{Q}} = 0. \tag{2.24}$$

2.2 Radial basis functions networks

Neural networks (NNs) can be considered as function approximation schemes. Two popular types of NNs are multilayer perceptron networks (MLPs) and radial basis function networks (RBFNs). They can approximate any continuous function to any degree of accuracy (universal approximation). RBFNs have a simpler structure and a faster training process than MLPs. The former are considered in the present research.

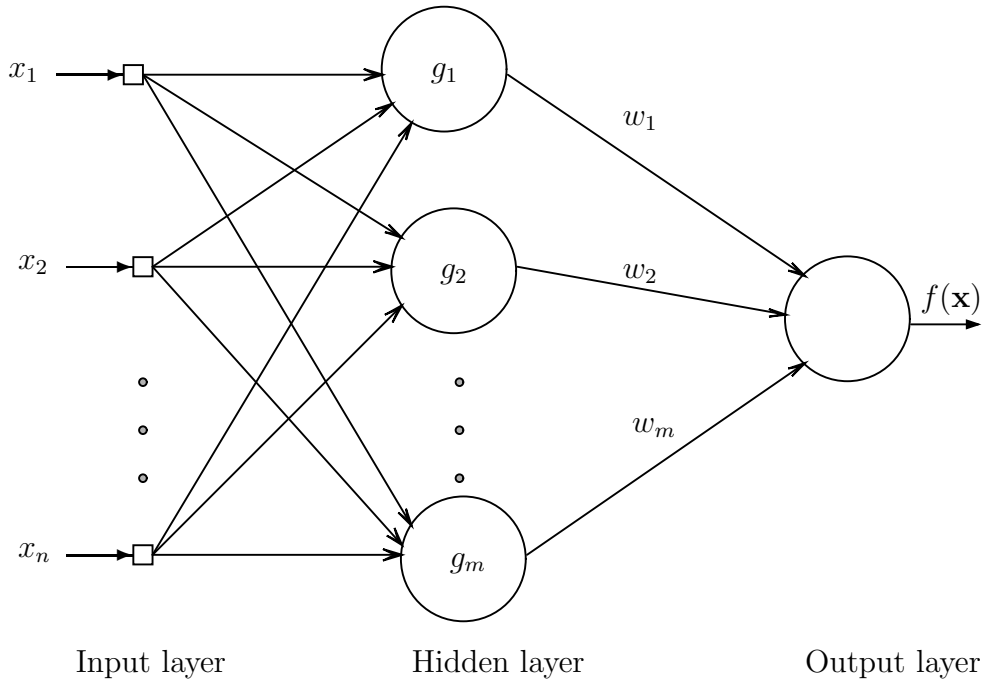

Figure 2.1: Structure of RBFN

2.2.1 Description

As shown in Figure 2.1, the structure of an RBFN consists of three layers, namely the input layer, the hidden layer and the output layer. Activation functions used in the hidden layer are RBFs, denoted by $g_i(\mathbf{x})$. There are two mappings involved: (i) nonlinear mapping from the input to the hidden layer; and (ii) linear mapping from the hidden to the output layer. The network can be described mathematically as

$$f(\mathbf{x}) = \sum_{i=1}^{m} w_i g_i \left(\|\mathbf{x} - \mathbf{c}_i\| \right), \tag{2.25}$$

where $\mathbf{x}$ is the input vector, f the output, $\{w_i\}_{i=1}^m$ the set of network weights, $\{g_i\}_{i=1}^m$ the set of RBFs, $\|\cdot\|$ the Euclidean norm, m the number of RBFs and $\mathbf{c}_i$ the centre of the ith RBF.

RBFNs (2.25) can be applied to determine the separate surfaces/lines for pattern classifications. The problem is basically solved by transforming it into a

high-dimensional space in a nonlinear way (Haykin, 1999). As stated in the Cover's theorem (Cover, 1965), the higher the dimension of the hidden layer, the more separate the classification will be.

RBFNs (2.25) can also be applied to represent an approximate function (Powell, 1988). For an interpolation problem (the input data does not contain noise), the set of input vectors is chosen to be the set of centres, i.e. $\mathbf{c}_i = \mathbf{x}_i$, and the set of network weights is found by minimising the cost function that is made up of the sum of squared nodal function errors:

$$\sum_{i=1}^{m} \left(d_i - f\left(\mathbf{x}_i\right)\right)^2 \to 0, \tag{2.26}$$

where $\{\mathbf{x}_i, d_i\}_{i=1}^{m}$ is a given set of training points. It is noted that, as shown in Micchelli's theorem (Micchelli, 1986), the interpolation matrix obtained from certain types of RBF is always invertible provided that the data points are distinct. For an approximation problem (the input data contain noise), the regularisation theory also needs be applied here to overcome the ill-conditioning of the RBF matrices (Poggio and Girosi, 1990). The number of centres is usually chosen to be less than the number of input vectors, and the set of network weights is found by minimising the cost function that is made up of the sum of squared nodal function errors and the regularisation term:

$$\sum_{i=1}^{q} \left(d_i - f\left(\mathbf{x}_i\right)\right)^2 + \sum_{i=1}^{q} \lambda_i \left(w_i\right)^2 \to 0, \qquad (q \leq m), \tag{2.27}$$

where $\{\lambda_i\}_{i=1}^{q}$ is the set of regularisation parameters.

2.2.2 Types of RBF

Many RBFs are covered by Micchelli's theorem. Some of them, which are of particular interest, are given below

$$g_i(\mathbf{x}) = \exp\left(-\frac{\|\mathbf{x}-\mathbf{c}_i\|^2}{a_i^2}\right), \quad \text{Gaussian functions} \tag{2.28}$$

$$g_i(\mathbf{x}) = \sqrt{\|\mathbf{x}-\mathbf{c}_i\|^2 + a_i^2}, \quad \text{Multiquadrics} \tag{2.29}$$

$$g_i(\mathbf{x}) = \frac{1}{\sqrt{\|\mathbf{x}-\mathbf{c}_i\|^2 + a_i^2}}, \quad \text{Inverse multiquadrics} \tag{2.30}$$

where a_i is the width/shape-parameter of the ith RBF. The variations of these RBFs in one dimension are shown in Figure 2.2.

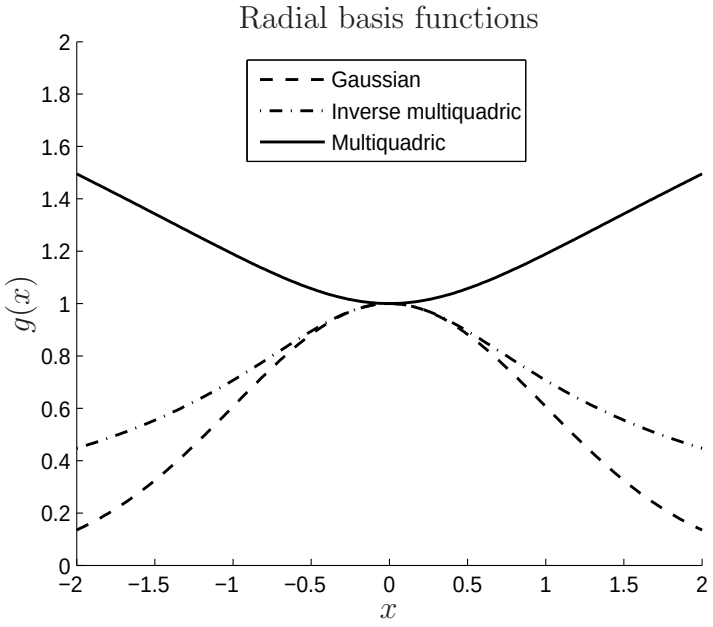

Figure 2.2: Plots of RBFs: one-dimensional version of (2.28) through (2.30). The centre is located at $x = 0$ and the value of a is chosen to be 1.

The Gaussian function (2.28) and the inverse multiquadrics (2.30) are both localised functions; their interpolation matrices are positive definite. In con-

trast, the multiquadrics (MQ) (2.29) is nonlocal and its interpolation matrix is not positive definite. Various numerical experiments showed that the MQ scheme gives the most accurate results (e.g. Franke, 1982). In this project, only MQ-RBFNs are considered.

2.3 RBFN approaches for function approximation

This section describes two basic approaches for the construction of the RBF approximations. The first (direct/differential) approach is based on differentiation, leading to differentiated RBFNs (Kansa, 1990a). The second (indirect/integral) approach is based on integration, leading to integrated RBFNs (Mai-Duy and Tran-Cong, 2001a).

2.3.1 Differentiated RBFNs (DRBFNs)

In the direct approach, an RBFN (2.25) is first used to represent the original function s, and expressions for derivative functions of s are then obtained by differentiating (2.25). It can be described mathematically as follows.

$$s(\mathbf{x}) \approx f(\mathbf{x}) = \sum_{i=1}^{m} w_i g_i(\mathbf{x}), \tag{2.31}$$

$$\frac{\partial^p s(\mathbf{x})}{\partial x_j^p} \approx \frac{\partial^p f(\mathbf{x})}{\partial x_j^p} = \frac{\partial^p \left(\sum_{i=1}^{m} w_i g_i(\mathbf{x})\right)}{\partial x_j^p} = \sum_{i=1}^{m} w_i D_i^{[x_j](p)}(\mathbf{x}), \tag{2.32}$$

where $\left\{ D_i^{[x_j](p)}(\mathbf{x}) \right\}_{i=1}^{m}$ is the set of basis functions used for the approximation of the pth-order derivative of a function s with respect to x_j, the superscript $[x_j]$ and $(\cdot)$ are used to denote the quantity associated with the x_j direction and

the order of the corresponding derivative function.

For an interpolation problem, the set of data points is chosen to be the set of centres, i.e. $\{\mathbf{c}_i\}_{i=1}^{m} \equiv \{\mathbf{x}_i\}_{i=1}^{N}$ with $m = N$ (N-the number of collocation points). Collocating (2.31) at the set of centres leads to

$$\widehat{f} = \widehat{\mathcal{G}}\widehat{w}, \tag{2.33}$$

where $\widehat{\mathcal{G}}$ is the interpolation matrix defined by

$$\mathcal{G} = \begin{pmatrix} g_1(\mathbf{x}_1) & g_2(\mathbf{x}_1) & \cdots & g_m(\mathbf{x}_1) \\ g_1(\mathbf{x}_2) & g_2(\mathbf{x}_2) & \cdots & g_m(\mathbf{x}_2) \\ \vdots & \vdots & \ddots & \vdots \\ g_1(\mathbf{x}_m) & g_2(\mathbf{x}_m) & \cdots & g_m(\mathbf{x}_m) \end{pmatrix};$$

$\widehat{f} = \{f(\mathbf{x}_i)\}_{i=1}^{m}$; and $\widehat{w} = \{w_i\}_{i=1}^{m}$.

Through solving (2.33), one can express the RBF weights in terms of nodal function values

$$\widehat{w} = \widehat{\mathcal{G}}^{-1}\widehat{f}. \tag{2.34}$$

The values of f and its derivatives at an arbitrary point $\mathbf{x}$ are computed by substituting (2.34) into (2.31)-(2.32)

$$f(\mathbf{x}) = [g_1(\mathbf{x}), g_2(\mathbf{x}), \cdots, g_m(\mathbf{x})]\,\widehat{\mathcal{G}}^{-1}\widehat{f}, \tag{2.35}$$

$$\frac{\partial^p f(\mathbf{x})}{\partial x_j^p} = \left[D_1^{[x_j](p)}(\mathbf{x}), D_2^{[x_j](p)}(\mathbf{x}), \cdots, D_m^{[x_j](p)}(\mathbf{x})\right]\widehat{\mathcal{G}}^{-1}\widehat{f}. \tag{2.36}$$

2.3.2 Integrated RBFNs (IRBFNs)

In the indirect approach, RBFNs (2.25) are used to represent the highest-order derivatives under consideration of a function s, e.g. $\partial^p s/\partial x_j^p$, and expressions for lower-order derivatives and the function itself are then obtained by integrating those RBFNs. It can be described mathematically as follows.

$$\frac{\partial^p s(\mathbf{x})}{\partial x_j^p} \approx \frac{\partial^p f(\mathbf{x})}{\partial x_j^p} = \sum_{i=1}^{m} w_i^{[x_j]} g_i(\mathbf{x}) = \sum_{i=1}^{m} w_i^{[x_j]} I_i^{[x_j](p)}(\mathbf{x}), \tag{2.37}$$

$$\frac{\partial^{p-1} s(\mathbf{x})}{\partial x_j^{p-1}} \approx \frac{\partial^{p-1} f(\mathbf{x})}{\partial x_j^{p-1}} = \sum_{i=1}^{m} w_i^{[x_j]} I_i^{[x_j](p-1)}(\mathbf{x}) + C_1^{[x_j]}, \tag{2.38}$$

$$\cdots\cdots\cdots\cdots\cdots\cdots$$

$$\begin{aligned}\frac{\partial s(\mathbf{x})}{\partial x_j} \approx \frac{\partial f(\mathbf{x})}{\partial x_j} &= \sum_{i=1}^{m} w_i^{[x_j]} I_i^{[x_j](1)}(\mathbf{x}) + \frac{x_j^{p-2}}{(p-2)!} C_1^{[x_j]} \\ &\quad + \frac{x_j^{p-3}}{(p-3)!} C_2^{[x_j]} + \cdots + x_j C_{p-2}^{[x_j]} + C_{p-1}^{[x_j]},\end{aligned} \tag{2.39}$$

$$\begin{aligned}s(\mathbf{x}) \approx f^{[x_j]}(\mathbf{x}) &= \sum_{i=1}^{m} w_i^{[x_j]} I_i^{[x_j](0)}(\mathbf{x}) + \frac{x_j^{p-1}}{(p-1)!} C_1^{[x_j]} \\ &\quad + \frac{x_j^{p-2}}{(p-2)!} C_2^{[x_j]} + \cdots + x_j C_{p-1}^{[x_j]} + C_p^{[x_j]},\end{aligned} \tag{2.40}$$

where C_ks are the constants of integration, which are functions of the independent variables other than x_j; and

$$\begin{aligned}I_i^{[x_j](p-1)} &= \int I_i^{[x_j](p)} dx_j, \\ I_i^{[x_j](p-2)} &= \int I_i^{[x_j](p-1)} dx_j, \\ &\cdots\cdots\cdots \\ I_i^{[x_j](1)} &= \int I_i^{[x_j](2)} dx_j, \\ I_i^{[x_j](0)} &= \int I_i^{[x_j](1)} dx_j\end{aligned}$$

are basis functions used for the approximation of the $(p-1)$th-order derivative, $(p-2)$th-order derivative, ..., 1st-order derivative and the original function s,

respectively.

In (Mai-Duy and Tran-Cong, 2003), these functions C_ks were represented by IRBFNs. By also using the notations $I_i^{[\cdot](\cdot)}(\mathbf{x})$ and $w_i^{[\cdot]}$ $(i > m)$ to denote basis functions and weights of these additional networks, respectively, expressions (2.37)-(2.40) can be rewritten as

$$\frac{\partial^p s(\mathbf{x})}{\partial x_j^p} \approx \frac{\partial^p f(\mathbf{x})}{\partial x_j^p} = \sum_{i=1}^{m} w_i^{[x_j]} I_i^{[x_j](p)}(\mathbf{x}), \tag{2.41}$$

$$\frac{\partial^{p-1} s(\mathbf{x})}{\partial x_j^{p-1}} \approx \frac{\partial^{p-1} f(\mathbf{x})}{\partial x_j^{p-1}} = \sum_{i=1}^{m+q^{(p-1)}} w_i^{[x_j]} I_i^{[x_j](p-1)}(\mathbf{x}), \tag{2.42}$$

$$\cdots\cdots\cdots\cdots\cdots\cdots$$

$$\frac{\partial s(\mathbf{x})}{\partial x_j} \approx \frac{\partial f(\mathbf{x})}{\partial x_j} = \sum_{i=1}^{m+q^{(1)}} w_i^{[x_j]} I_i^{[x_j](1)}(\mathbf{x}), \tag{2.43}$$

$$s(\mathbf{x}) \approx f^{[x_j]}(\mathbf{x}) = \sum_{i=1}^{m+q^{(0)}} w_i^{[x_j]} I_i^{[x_j](0)}(\mathbf{x}), \tag{2.44}$$

where $\{q^{(0)}, \ldots, q^{(p-1)}\}$ are the sizes of subnetworks used for the representation of the constants of integration $(q^{(p-2)} = 2q^{(p-1)}, \ldots, q^{(0)} = pq^{(p-1)})$.

Unlike the differential approach, the starting point of the integral approach can vary in use, depending on the particular application under consideration.

The conversion process for IRBFNs is similar to that for DRBFNs. Following the same process as used in DRBFNs, i.e. (2.33)-(2.34), the relationship between the network weight space and the physical space for IRBFNs can be established as

$$\widehat{f}^{[x_j]} = \widehat{\mathcal{I}}^{[x_j](0)} \widehat{w}^{[x_j]}, \tag{2.45}$$

$$\widehat{w}^{[x_j]} = \left(\widehat{\mathcal{I}}^{[x_j](0)}\right)^{-1} \widehat{f}, \tag{2.46}$$

where $\widehat{f}^{[x_j]} = \left\{f^{[x_j]}(\mathbf{x}_i)\right\}_{i=1}^{m}$; $\widehat{w}^{[x_j]} = \left\{w_i^{[x_j]}\right\}_{i=1}^{m+q^{(p)}}$; and $\widehat{\mathcal{I}}^{[x_j](0)}$ is the interpolation matrix given by

$$\widehat{\mathcal{I}}^{[x_j](0)} = \begin{pmatrix} I_1^{[x_j](0)}(\mathbf{x}_1) & I_2^{[x_j](0)}(\mathbf{x}_1) & \cdots & I_{m+q^{(p)}}^{[x_j](0)}(\mathbf{x}_1) \\ I_1^{[x_j](0)}(\mathbf{x}_2) & I_2^{[x_j](0)}(\mathbf{x}_2) & \cdots & I_{m+q^{(p)}}^{[x_j](0)}(\mathbf{x}_2) \\ \vdots & \vdots & \ddots & \vdots \\ I_1^{[x_j](0)}(\mathbf{x}_m) & I_2^{[x_j](0)}(\mathbf{x}_m) & \cdots & I_{m+q^{(p)}}^{[x_j](0)}(\mathbf{x}_m) \end{pmatrix}.$$

The values of f and its derivatives at an arbitrary point $\mathbf{x}$ are computed by substituting (2.46) into (2.41)-(2.44)

$$\frac{\partial^p f(\mathbf{x})}{\partial x_j^p} = \left[I_1^{[x_j](p)}(\mathbf{x}), I_2^{[x_j](p)}(\mathbf{x}), \cdots\right] \left(\widehat{\mathcal{I}}^{[x_j](0)}\right)^{-1} \widehat{f}, \tag{2.47}$$

$$\frac{\partial^{p-1} f(\mathbf{x})}{\partial x_j^{p-1}} = \left[I_1^{[x_j](p-1)}(\mathbf{x}), I_2^{[x_j](p-1)}(\mathbf{x}), \cdots\right] \left(\widehat{\mathcal{I}}^{[x_j](0)}\right)^{-1} \widehat{f}, \tag{2.48}$$

$$\cdots\cdots\cdots\cdots\cdots\cdots$$

$$\frac{\partial f(\mathbf{x})}{\partial x_j} = \left[I_1^{[x_j](1)}(\mathbf{x}), I_2^{[x_j](1)}(\mathbf{x}), \cdots\right] \left(\widehat{\mathcal{I}}^{[x_j](0)}\right)^{-1} \widehat{f}, \tag{2.49}$$

$$f^{[x_j]}(\mathbf{x}) = \left[I_1^{[x_j](0)}(\mathbf{x}), I_2^{[x_j](0)}(\mathbf{x}), \cdots\right] \left(\widehat{\mathcal{I}}^{[x_j](0)}\right)^{-1} \widehat{f}. \tag{2.50}$$

It can be seen that $f(\mathbf{x})$ can be obtained from different $[x_j]-$IRBFNs. Due to numerical error, these values are expected not to be identical. As a result, the value of f at $\mathbf{x}$ needs be taken in an average sense

$$f(\mathbf{x}) = \frac{1}{n}\sum_{j=1}^{n} f^{[x_j]}(\mathbf{x}), \tag{2.51}$$

where n is the dimension of the problem.

One-dimensional IRBFNs:

In the case of one-dimensional domain (e.g. a curved/straight line), IRBFN

expressions (2.41)-(2.44) reduce to

$$\frac{d^p f(\eta)}{d\eta^p} = \sum_{i=1}^{N_\eta} w_i g_i(\eta) = \sum_{i=1}^{N_\eta} w_i I_i^{(p)}(\eta), \tag{2.52}$$

$$\frac{d^{p-1} f(\eta)}{d\eta^{p-1}} = \sum_{i=1}^{N_\eta} w_i I_i^{(p-1)}(\eta) + C_1, \tag{2.53}$$

$$\cdots \quad \cdots \qquad \cdots \qquad \cdots \qquad \cdots$$

$$\frac{df(\eta)}{d\eta} = \sum_{i=1}^{N_\eta} w_i I_i^{(1)}(\eta) + C_1 \frac{\eta^{p-2}}{(p-2)!} + C_2 \frac{\eta^{p-3}}{(p-3)!} + \cdots + C_{p-2}\eta + C_{p-1}, \tag{2.54}$$

$$f(\eta) = \sum_{i=1}^{N_\eta} w_i I_i^{(0)}(\eta) + C_1 \frac{\eta^{p-1}}{(p-1)!} + C_2 \frac{\eta^{p-2}}{(p-2)!} + \cdots + C_{p-1}\eta + C_p, \tag{2.55}$$

where N_η is the number of nodes on the η line, $g_i(\eta)$ the RBF in one dimension (e.g. $g_i(\eta) = \sqrt{(\eta - c_i)^2 + a_i^2}$ for the multiquadrics (c_i the centre and a_i the width)), and $\{C_1, C_2, \cdots, C_p\}$ the constants of integration.

Evaluation of (2.55) at a set of collocation points $\{x_j\}_{j=1}^{N_\eta}$ leads to

$$\widehat{f} = \widehat{\mathcal{I}}^{(0)} \widehat{w}, \tag{2.56}$$

where

$$\widehat{\mathcal{I}}^{(0)} = \begin{bmatrix} I_1^{(0)}(\eta_1), & I_2^{(0)}(\eta_1), & \cdots, & I_{N_\eta}^{(0)}(\eta_1), & \frac{\eta_1^{p-1}}{(p-1)!}, & \frac{\eta_1^{p-2}}{(p-2)!}, & \cdots, & \eta_1, & 1 \\ I_1^{(0)}(\eta_2), & I_2^{(0)}(\eta_2), & \cdots, & I_{N_\eta}^{(0)}(\eta_2), & \frac{\eta_2^{p-1}}{(p-1)!}, & \frac{\eta_2^{p-2}}{(p-2)!}, & \cdots, & \eta_2, & 1 \\ \vdots & \vdots & \ddots & \vdots & \vdots & \vdots & \ddots & \vdots & \vdots \\ I_1^{(0)}(\eta_{N_\eta}), & I_2^{(0)}(\eta_{N_\eta}), & \cdots, & I_{N_\eta}^{(0)}(\eta_{N_\eta}), & \frac{\eta_{N_\eta}^{p-1}}{(p-1)!}, & \frac{\eta_{N_\eta}^{p-2}}{(p-2)!}, & \cdots, & \eta_{N_\eta}, & 1 \end{bmatrix};$$

$$\widehat{w} = \left(w_1, w_2, \cdots, w_{N_\eta}, C_1, C_2, \cdots, C_p\right)^T;$$

and

$$\widehat{f} = \left(f_1, f_2, \cdots, f_{N_\eta}\right)^T.$$

A mapping from the physical space to the network weight space is thus given by

$$\widehat{w} = \left(\widehat{\mathcal{I}}^{(0)}\right)^{-1} \widehat{f}. \tag{2.57}$$

Making use of (2.57), the values of f and its derivatives at an arbitrary point η are computed by

$$\frac{d^p f(\eta)}{d\eta^p} = \left[I_1^{(p)}(\eta), I_2^{(p)}(\eta), \cdots, I_{N_\eta}^{(p)}, 0, 0, \cdots, 0, 0\right] \left(\widehat{\mathcal{I}}^{(0)}\right)^{-1} \widehat{f}, \tag{2.58}$$

$$\frac{d^{p-1} f(\eta)}{d\eta^{p-1}} = \left[I_1^{(p-1)}(\eta), I_2^{(p-1)}(\eta), \cdots, I_{N_\eta}^{(p-1)}, 1, 0, \cdots, 0, 0\right] \left(\widehat{\mathcal{I}}^{(0)}\right)^{-1} \widehat{f}, \tag{2.59}$$

$$\cdots\cdots\cdots\cdots\cdots\cdots$$

$$\frac{df(\eta)}{d\eta} = \left[I_1^{(1)}(\eta), I_2^{(1)}(\eta), \cdots, I_{N_\eta}^{(1)}(\eta), \frac{\eta^{p-2}}{(p-2)!}, \frac{\eta^{p-3}}{(p-3)!}, \cdots, 1, 0\right] \left(\widehat{\mathcal{I}}^{(0)}\right)^{-1} \widehat{f}, \tag{2.60}$$

$$f(\eta) = \left[I_1^{(0)}(\eta), I_2^{(0)}(\eta), \cdots, I_{N_\eta}^{(0)}(\eta), \frac{\eta^{p-1}}{(p-1)!}, \frac{\eta^{p-2}}{(p-2)!}, \cdots, \eta, 1\right] \left(\widehat{\mathcal{I}}^{(0)}\right)^{-1} \widehat{f}. \tag{2.61}$$

2.4 RBFN approaches for solution of ODEs/PDEs

In this section, we briefly outline the basic use of DRBFNs/IRBFNs for solving ODEs/PDEs. To introduce these RBFN approaches, we consider a linear boundary value problem governed by the governing equation (2.1) and boundary conditions (2.2)-(2.3).

The problem domain Ω is discretised by a set of collocation points that can be randomly distributed. The field variable u can be sought by using DRBFNs

(2.31)-(2.32) or using IRBFNs (2.47)-(2.50), which can be rewritten in the following generic form

$$u(\mathbf{x}) = \sum_{i=1}^{N} \phi_i(\mathbf{x})\,\alpha_i, \tag{2.62}$$

$$\frac{\partial^p u(\mathbf{x})}{\partial x_j^p} = \sum_{i=1}^{N} \frac{\partial^p \phi_i(\mathbf{x})}{\partial x_j^p}\alpha_i, \tag{2.63}$$

where $p = \{1, 2, \cdots\}$, N is the number of collocation points, $\{\alpha_i\}_{i=1}^{N}$ the set of unknown coefficients and $\{\phi_i(\mathbf{x})\}_{i=1}^{N}$ the set of known basis functions that are linearly independent.

RBFNs (2.62)-(2.63) with their free parameters α_i and $\mathbf{c}_i$ need be trained to satisfy the governing equation (2.1) and the boundary conditions (2.2)-(2.3)

$$\sum_{\mathbf{x}_k\in\Omega}\left[\mathcal{L}(u(\mathbf{x}_k)) - \bar{b}_k\right]^2 + \sum_{\mathbf{x}_k\in\Gamma_{\mathcal{Q}}}\left[\mathcal{Q}(u(\mathbf{x}_k)) - \bar{q}_k\right]^2 + \sum_{\mathbf{x}_k\in\Gamma_{\mathcal{U}}}\left[\mathcal{U}(u(\mathbf{x}_k)) - \bar{u}_k\right]^2 \to 0. \tag{2.64}$$

In practice, the set of centres is chosen to be the same as the set of collocation points, i.e. $\{\mathbf{c}_i\}_{i=1}^{m} \equiv \{\mathbf{x}_i\}_{i=1}^{N}$ $(m = N)$. The cost function (2.64) may thus simply reduce to a determined system of linear algebraic equations

$$\mathcal{L}(u(\mathbf{x}_k)) = \bar{b}_k, \qquad (1 \le k \le N_{ip}), \tag{2.65}$$

$$\mathcal{Q}(u(\mathbf{x}_k)) = \bar{q}_k, \qquad (N_{ip}+1 \le k \le N_{ip}+N_{\Gamma_{\mathcal{Q}}}), \tag{2.66}$$

$$\mathcal{U}(u(\mathbf{x}_k)) = \bar{u}_k, \qquad (N_{ip}+N_{\Gamma_{\mathcal{Q}}}+1 \le k \le N), \tag{2.67}$$

where N_{ip} is the number of interior points, $N_{\Gamma_\mathcal{Q}}$ the number of collocated points on $\Gamma_\mathcal{Q}$.

Theoretical studies on accuracy of RBFN-based methods were reported in, e.g., (Madych and Nelson, 1988; Buhmann and Dyn, 1993; Franke and Schaback, 1998). In the case of function interpolation, spectral accuracy was shown for certain types of RBF (Madych and Nelson, 1988; Buhmann and Dyn, 1993). In the case of numerical solution of ODEs/PDEs, the reader is referred to (Franke and Schaback, 1998) for a proof of error bounds of DRBFN-based collocation methods. Numerical results for various engineering and science problems (e.g. Li et al., 2003) indicated that RBFN-based collocation methods can yield a high level of accuracy using a relatively low number of nodes. In the work of (Cheng et al., 2003; Larson and Fornberg, 2003; Fornberg et al., 2010), an RBF solution was numerically shown to converge at a rate as high as that of spectral methods. In terms of numerical stability, RBFN systems generally have high condition numbers even for only a few hundred nodes used. In order to improve the conditioning of RBFN systems, the following schemes can be applied

- compactly-supported RBFs (e.g. Wendland, 1995; Wu, 1995)
- preconditioners (e.g. Ling and Kansa, 2004, 2005)
- domain decomposition (e.g. Zhou et al., 2003; Li and Hon, 2004; Divo and Kassab, 2005, 2006)
- local RBF approximations (e.g. Shu, Ding, Chen and Wang, 2005; Kovačvić and Šarler, 2005; Šarler and Vertnik, 2006; Wright and Fornberg, 2006; El-Zahab, Divo and Kassab, 2009)

In the case of IRBFN methods, Mai-Duy and Tran-Cong (2007) proposed an one-dimensional IRBFN (1D-IRBFN) collocation approach. In this approach, the approximations for the field variable at a grid node involve only nodal points on the two associated grid lines for 2D problems or three associated grid lines

for 3D problems. As a result, some degree of local approximation is achieved. Numerical results (e.g. Mai-Duy and Tran-Cong, 2007; Le-Cao, Mai-Duy and Tran-Cong, 2009; Le, Mai-Duy, Tran-Cong and Baker, 2010) showed that 1D-IRBFNs can employ a larger number of nodes and are much more economical in terms of storage space and CPU time than global IRBFNs (e.g. Mai-Duy and Tran-Cong, 2001a).

Chapter 3

1D-IRBFN-based Galerkin method for the streamfunction-vorticity formulation governing viscous flows

This chapter reports a new discretisation technique for the streamfunction-vorticity ($\psi - \omega$) formulation governing thermally-driven viscous flows defined in 2D enclosured domains. The proposed technique combines strengths of three schemes, i.e. smooth PDE discretisations (Galerkin formulation), powerful high-order approximations (one-dimensional integrated radial-basis-function networks) and pressure-free low-order PDE system ($\psi-\omega$ formulation). In addition, a new effective way of deriving computational boundary conditions for the vorticity is proposed. Two benchmark test problems, namely free convection in a square slot and in a concentric annulus, are considered, where a convergent solution for the former is achieved up to the Rayleigh number of 10^8.

3.1 Introduction

The application of radial basis function networks (RBFNs) for solving partial differential equations (PDEs) has received a great deal of attention from both scientific and engineering research communities over the past 20 years. From a neural-network point of view, the unknown RBF weights can be found via the least-squares principle as discussed earlier in Section 2.4. From the view of the method of weighted residual (MWR) (Brebbia et al., 1984), a solution to an PDE can be found through a number of channels, including point-collocation, Galerkin and subdomain-collocation formulations (see Section 2.1). In this MWR framework, most RBFN works reported in the literature can be viewed as some sorts of a point-collocation approach, where RBFNs are used as trial functions. Owing to their meshfree feature and spectral accuracy, RBFN-based collocation methods can handle well problems defined on irregular domains and provide accurate results using relatively coarse discretisations. However, due to a fast growth of the matrix condition number, RBFN methods are generally limited to discretisations with a few hundred of nodes. In addition, RBFN-based solutions to Neumann-type boundary-value problems are much less accurate than those to Dirichlet-type ones. There have been only a few RBFN works in conjunction with the Galerkin formulation (Wendland, 1999; Mai-Duy and Tran-Cong, 2009c; and Fasshauer, 2007, chapter 45). In (Mai-Duy and Tran-Cong, 2009c), a Galerkin method incorporating IRBFNs in one dimension was shown to yield accurate results, high rates of convergence, and especially similar levels of accuracy for both types of boundary condition (i.e. Dirichlet only and Dirichlet-Neumann) for the solution of linear Poisson equations.

RBFN-based methods have been applied to simulate heat flow problems (e.g. Divo and Kassab, 2007, 2008; Kosec and Šarler, 2007). Solutions were reported not only to analytic test problems but also to complex and practical applications. For the latter, examples include (i) simulation of steady thermal flows in porous media (Šarler, Perko and Chen, 2004; Kosec and Šarler, 2008); (ii) a flow

of colder air from a plenum through a steel plate into a hotter incoming flow (Divo and Kassab, 2007); (iii) heat generation in living tissue (Erhart, Divo and Kassab, 2008); (iv) solid-solid and solid-liquid phase-change problems (Kovačvić and Šarler, 2005; Vertnik and Šarler, 2006); and (v) continuous casting of aluminium (Vertnik, Založnik and Šarler, 2006). On the other hand, RBFNs were employed in the dual reciprocity boundary element method (DRBEM) for coupled fluid flow and heat transfer problems (e.g. Rahaim and Kassab, 1996) and for transport phenomena in porous media (e.g. Šarler et al., 2000; Šarler, Perko, Gobin, Goyeau and Power, 2004).

Natural convection, which occurs in many engineering applications, presents a strong coupling of heat transfer and fluid flow. Problems of this type have been extensively studied by means of experimental and numerical simulations. Natural convection in a square slot and in an annulus are widely considered as two benchmark problems for the testing of new numerical schemes in CFD. In the context of RBFN-based methods, the two problems were simulated with (i) global approximation versions (e.g. Šarler et al., 2001; Šarler, 2005; Mai-Duy and Tran-Cong, 2001a); and (ii) local approximation versions (e.g. Shu et al., 2003; Kosec and Šarler, 2007; Divo and Kassab, 2008). Most works were reported for a range of the Rayleigh (Ra) number from 10^2 to 10^6. For the case of high Ra numbers (e.g. $Ra \geq 10^6$ for natural convection in a square slot), very thin boundary layers are formed, which presents a great challenge for any numerical method. As a result, to simulate such cases, low-order techniques such as finite-difference methods (FDMs) (e.g. Saitoh and Hirose, 1989) and finite-element methods (FEMs) (e.g Manzari, 1999; Wan et al., 2001; Mayne et al., 2000, 2001) typically require a very fine mesh. This requirement is alleviated by employing high-order methods such as pseudo-spectral methods (e.g. Quéré, 1991), discrete singular convolution (DSC) methods (e.g. Wan et al., 2001), meshless diffuse approximation methods (DAMs) (e.g. Sadat and Couturier, 2000), and mesh-free local RBF collocation methods (RBFCM) (e.g. Kosec and Šarler, 2007). However, in general, there still exist some difficult problems

associated with convergence (e.g. very few reported results for the case of $Ra > 10^6$ for natural convection in a square slot) and accuracy (e.g. some discrepancies in the prediction of the Nusselt number among published works).

In this chapter, we introduce 1D-IRBFNs as trial functions in the Galerkin formulation for the simulation of natural convection in two dimensions. The boundary conditions are satisfied in a local sense using the point collocation formulation, and the solution to the problem is satisfied in a global sense using the Galerkin formulation. Advantages of using 1D-IRBFNs over 2D-IRBFNs are (i) the construction cost is much lower ("local" approximations); and (ii) the matrix condition is greatly improved. However, tensor products are required to construct the 1D-IRBFN approximations over the whole domain. One thus needs to use coordinate transformations to handle nonrectangular domains. Unlike FD and Chebyshev interpolation schemes, IRBFNs can work well with nonuniform and uniform Cartesian grids.

The streamfunction-vorticity ($\psi - \omega$) formulation will be adopted here to take the following advantages: (i) the continuity equation is satisfied automatically; and (ii) its implementation is easier as the pressure variable is eliminated. However, when using the $\psi - \omega$ formulation, the classical difficulties lie in the treatment of boundary condition for the vorticity. A new effective boundary scheme is proposed, where computational boundary conditions for the vorticity are derived in a precise manner (i.e. approximations used on the boundary have the same order as those for the interior points, and derivative values of the streamfunction on the boundary are incorporated into the IRBFN approximations in an exact manner). The resultant system of algebraic equations is symmetric and has a relatively-low condition number, which facilitate the employment of much larger numbers of nodes. The present method is verified through the simulation of natural convection in 2D enclosed domains. Two different geometries are considered: (i) a square slot; and (ii) a concentric annulus. It will be shown that convergent solutions are achieved for very high values of the

Rayleigh number (i.e. up to 10^8 for the former and 7×10^4 for the latter). Numerical results obtained are compared with those by other techniques available in the literature.

The remainder of this chapter is organised as follows. Section 3.2 briefly describes the governing equations in both Cartesian and cylindrical coordinates. Our proposed technique is presented in detail in section 3.3, including 1D-IRBFN representations of the field variables, Galerkin discretisations of the PDEs and a new treatment for the vorticity boundary condition. In section 3.4, the technique is verified through the simulation of several benchmark test problems. Section 3.5 concludes this chapter.

3.2 Governing equations

The governing equations (1.1), (1.2) and (1.4) for viscous flows are written in the streamfunction-vorticity-temperature form. Both Cartesian and cylindrical coordinate systems are employed here. Using the Boussinesq approximation, their 2D dimensionless forms can be written as

$$\frac{\partial^2 \psi}{\partial x^2} + \frac{\partial^2 \psi}{\partial y^2} = -\omega, \tag{3.1}$$

$$\frac{\partial \omega}{\partial t} + u_x \frac{\partial \omega}{\partial x} + u_y \frac{\partial \omega}{\partial y} = \sqrt{\frac{Pr}{Ra}} \left(\frac{\partial^2 \omega}{\partial x^2} + \frac{\partial^2 \omega}{\partial y^2} \right) + \frac{\partial T}{\partial x}, \tag{3.2}$$

$$\frac{\partial T}{\partial t} + u_x \frac{\partial T}{\partial x} + u_y \frac{\partial T}{\partial y} = \frac{1}{\sqrt{RaPr}} \left(\frac{\partial^2 T}{\partial x^2} + \frac{\partial^2 T}{\partial y^2} \right), \tag{3.3}$$

for Cartesian coordinates, where

$$u_x = \frac{\partial \psi}{\partial y}, \quad u_y = -\frac{\partial \psi}{\partial x},$$

and

$$\frac{\partial^2\psi}{\partial r^2}+\frac{1}{r}\frac{\partial\psi}{\partial r}+\frac{1}{r^2}\frac{\partial^2\psi}{\partial\theta^2}=-\omega, \tag{3.4}$$

$$\frac{\partial\omega}{\partial t}+\left(u_r\frac{\partial\omega}{\partial r}+\frac{u_\theta}{r}\frac{\partial\omega}{\partial\theta}\right)=\sqrt{\frac{Pr}{Ra}}\left(\frac{\partial^2\omega}{\partial r^2}+\frac{1}{r}\frac{\partial\omega}{\partial r}+\frac{1}{r^2}\frac{\partial^2\omega}{\partial\theta^2}\right)-\left(\sin\theta\frac{\partial T}{\partial r}+\frac{1}{r}\cos\theta\frac{\partial T}{\partial\theta}\right), \tag{3.5}$$

$$\frac{\partial T}{\partial t}+\left(u_r\frac{\partial T}{\partial r}+\frac{u_\theta}{r}\frac{\partial T}{\partial\theta}\right)=\frac{1}{\sqrt{RaPr}}\left(\frac{\partial^2T}{\partial r^2}+\frac{1}{r}\frac{\partial T}{\partial r}+\frac{1}{r^2}\frac{\partial^2T}{\partial\theta^2}\right), \tag{3.6}$$

for cylindrical coordinates, where

$$u_r=\frac{1}{r}\frac{\partial\psi}{\partial\theta},\quad u_\theta=-\frac{\partial\psi}{\partial r}.$$

In (3.3) and (3.6), Pr and Ra are the Prandtl and Rayleigh numbers defined as $Pr=\nu/\alpha$ and $Ra=\beta g\Delta TL^3/\alpha\nu$, respectively in which ν is the kinematic viscosity, α the thermal diffusivity, β the thermal expansion coefficient, g the gravity, and L and ΔT the characteristic length and temperature difference, respectively. In this dimensionless scheme, the velocity scale is taken as $U=\sqrt{gL\beta\Delta T}$ for the purpose of balancing the buoyancy and inertial forces.

The given velocity boundary conditions can be transformed into two boundary conditions on the streamfunction and its normal derivative

$$\psi=A, \tag{3.7}$$

$$\frac{\partial\psi}{\partial n}=B, \tag{3.8}$$

where n is the direction normal to the boundary, and A and B given functions which are simply zero here. For problems presented in this chapter, the boundary conditions for the energy equation are prescribed with both Dirichlet and

Neumann types.

3.3 1D-IRBFN-based Galerkin technique

Let the problem domain be rectangular and represented by a Cartesian grid. On each grid line, 1D-IRBFNs are employed to approximate the field variables (i.e. ψ, ω and T). The governing equations are discretised by means of Galerkin approximations (i.e. the residuals are set to zero in the mean). Vorticity boundary conditions are derived globally.

3.3.1 One-dimensional IRBFN representations of the field variables

The system of PDEs under consideration here is of second order. Consider an η grid line. Making use of (2.52)-(2.55) with $p = 2$, a function f and its derivatives with respect to η can be represented as follows

$$\frac{d^2 f(\eta)}{d\eta^2} = \sum_{i=1}^{N_\eta} w_i g_i(\eta) = \sum_{i=1}^{N_\eta} w_i I_i^{(2)}(\eta), \tag{3.9}$$

$$\frac{df(\eta)}{d\eta} = \sum_{i=1}^{N_\eta} w_i I_i^{(1)}(\eta) + C_1, \tag{3.10}$$

$$f(\eta) = \sum_{i=1}^{N_\eta} w_i I_i^{(0)}(\eta) + C_1\eta + C_2, \tag{3.11}$$

where N_η is the number of nodes on the grid line, $\{w_i\}_{i=1}^{N_\eta}$ the set of network weights, and $\{g_i(\eta)\}_{i=1}^{N_\eta} \equiv \left\{I_i^{(2)}(\eta)\right\}_{i=1}^{N_\eta}$ the set of RBFs, $I_i^{(1)}(\eta) = \int I_i^{(2)}(\eta)d\eta$, $I_i^{(0)}(\eta) = \int I_i^{(1)}(\eta)\,d\eta$, and C_1 and C_2 are the constants of integration. In (3.9) - (3.11), the function f can be used to represent the streamfunction, the

vorticity or the temperature, while the variable η is employed to denote the (x, y) coordinate (Cartesian system), or (r, θ) coordinate (cylindrical system).

Evaluation of equations (3.9) - (3.11) at the grid nodes leads to

$$\widehat{\frac{d^2 f}{d\eta^2}} = \widehat{\mathcal{I}}^{(2)}\widehat{\alpha}, \tag{3.12}$$

$$\widehat{\frac{df}{d\eta}} = \widehat{\mathcal{I}}^{(1)}\widehat{\alpha}, \tag{3.13}$$

$$\widehat{f} = \widehat{\mathcal{I}}^{(0)}\widehat{\alpha}, \tag{3.14}$$

where the superscript (.) is used to denote the order of the corresponding derivative function;

$$\widehat{\mathcal{I}}^{(2)} = \begin{bmatrix} I_1^{(2)}(\eta_1), & I_2^{(2)}(\eta_1), & \cdots, & I_{N_\eta}^{(2)}(\eta_1), & 0, & 0 \\ I_1^{(2)}(\eta_2), & I_2^{(2)}(\eta_2), & \cdots, & I_{N_\eta}^{(2)}(\eta_2), & 0, & 0 \\ \vdots & \vdots & \ddots & \vdots & \vdots & \vdots \\ I_1^{(2)}(\eta_{N_\eta}), & I_2^{(2)}(\eta_{N_\eta}), & \cdots, & I_{N_\eta}^{(2)}(\eta_{N_\eta}), & 0, & 0 \end{bmatrix};$$

$$\widehat{\mathcal{I}}^{(1)} = \begin{bmatrix} I_1^{(1)}(\eta_1), & I_2^{(1)}(\eta_1), & \cdots, & I_{N_\eta}^{(1)}(\eta_1), & 1, & 0 \\ I_1^{(1)}(\eta_2), & I_2^{(1)}(\eta_2), & \cdots, & I_{N_\eta}^{(1)}(\eta_2), & 1, & 0 \\ \vdots & \vdots & \ddots & \vdots & \vdots & \vdots \\ I_1^{(1)}(\eta_{N_\eta}), & I_2^{(1)}(\eta_{N_\eta}), & \cdots, & I_{N_\eta}^{(1)}(\eta_{N_\eta}), & 1, & 0 \end{bmatrix};$$

$$\widehat{\mathcal{I}}^{(0)} = \begin{bmatrix} I_1^{(0)}(\eta_1), & I_2^{(0)}(\eta_1), & \cdots, & I_{N_\eta}^{(0)}(\eta_1), & \eta_1, & 1 \\ I_1^{(0)}(\eta_2), & I_2^{(0)}(\eta_2), & \cdots, & I_{N_\eta}^{(0)}(\eta_2), & \eta_2, & 1 \\ \vdots & \vdots & \ddots & \vdots & \vdots & \vdots \\ I_1^{(0)}(\eta_{N_\eta}), & I_2^{(0)}(\eta_{N_\eta}), & \cdots, & I_{N_\eta}^{(0)}(\eta_{N_\eta}), & \eta_{N_\eta}, & 1 \end{bmatrix};$$

$$\widehat{\alpha} = \left(w_1, w_2, \cdots, w_{N_\eta}, C_1, C_2\right)^T;$$

and

$$\begin{aligned}\widehat{\frac{d^2f}{d\eta^2}} &= \left(\frac{d^2f_1}{d\eta^2}, \frac{d^2f_2}{d\eta^2}, \cdots, \frac{d^2f_{N_\eta}}{d\eta^2}\right)^T; \\ \widehat{\frac{df}{d\eta}} &= \left(\frac{df_1}{d\eta}, \frac{df_2}{d\eta}, \cdots, \frac{df_{N_\eta}}{d\eta}\right)^T; \\ \widehat{f} &= \left(f_1, f_2, \cdots, f_{N_\eta}\right)^T,\end{aligned}$$

in which $d^2f_j/d\eta^2 = d^2f(\eta_j)/d\eta^2$, $df_j/d\eta = df(\eta_j)/d\eta$ and $f_j = f(\eta_j)$ with $j = \{1, 2, \cdots, N_\eta\}$.

The relations between the RBF-coefficient space $\widehat{\alpha}$ and the physical space $\widehat{f}$ are given by

$$\begin{pmatrix} \widehat{f} \\ \widehat{e} \end{pmatrix} = \begin{bmatrix} \widehat{\mathcal{I}}^{(0)} \\ \widehat{\mathcal{K}} \end{bmatrix} \widehat{\alpha} = \widehat{\mathcal{C}}\widehat{\alpha}, \tag{3.15}$$

$$\widehat{\alpha} = \widehat{\mathcal{C}}^{-1} \begin{pmatrix} \widehat{f} \\ \widehat{e} \end{pmatrix}, \tag{3.16}$$

where $\widehat{e} = \widehat{\mathcal{K}}\widehat{\alpha}$ represents the extra information (e.g. normal derivative values at the two end-points) and $\widehat{\mathcal{C}}$ the conversion matrix.

Expressions for computing the values of f and its derivatives at an arbitrary

point η on the grid line will be obtained by substituting (3.16) into (3.9)-(3.11)

$$f(\eta) = \left(I_1^{(0)}(\eta), I_2^{(0)}(\eta), \cdots, I_{N_\eta}^{(0)}(\eta), \eta, 1\right) \widehat{\mathcal{C}}^{-1} \begin{pmatrix} \widehat{f} \\ \widehat{e} \end{pmatrix}, \tag{3.17}$$

$$\frac{\partial f(\eta)}{\partial \eta} = \left(I_1^{(1)}(\eta), I_2^{(1)}(\eta), \cdots, I_{N_\eta}^{(1)}(\eta), 1, 0\right) \widehat{\mathcal{C}}^{-1} \begin{pmatrix} \widehat{f} \\ \widehat{e} \end{pmatrix}, \tag{3.18}$$

$$\frac{\partial^2 f(\eta)}{\partial \eta^2} = \left(I_1^{(2)}(\eta), I_2^{(2)}(\eta), \cdots, I_{N_\eta}^{(2)}(\eta), 0, 0\right) \widehat{\mathcal{C}}^{-1} \begin{pmatrix} \widehat{f} \\ \widehat{e} \end{pmatrix}. \tag{3.19}$$

They can be rewritten in compact form

$$f(\eta) = \sum_{i=1}^{N_\eta} \varphi_i(\eta) f_i + \varphi_{N_\eta+1}(\eta) e_1 + \varphi_{N_\eta+2}(\eta) e_2, \tag{3.20}$$

$$\frac{\partial f(\eta)}{\partial \eta} = \sum_{i=1}^{N_\eta} \frac{\partial \varphi_i(\eta)}{\partial \eta} f_i + \frac{\partial \varphi_{N_\eta+1}(\eta)}{\partial \eta} e_1 + \frac{\partial \varphi_{N_\eta+2}(\eta)}{\partial \eta} e_2, \tag{3.21}$$

$$\frac{\partial^2 f(\eta)}{\partial \eta^2} = \sum_{i=1}^{N_\eta} \frac{\partial^2 \varphi_i(\eta)}{\partial \eta^2} f_i + \frac{\partial^2 \varphi_{N_\eta+1}(\eta)}{\partial \eta^2} e_1 + \frac{\partial^2 \varphi_{N_\eta+2}(\eta)}{\partial \eta^2} e_2, \tag{3.22}$$

where $\{\varphi_i\}_{i=1}^{N_\eta+2}$ is the set of IRBFN basis functions in the physical space.

One can take products of integrated RBFs in each direction as basis functions for the interpolation of f over the entire 2D domain. The IRBFN approximation is defined everywhere in the domain. It is easy to get the value of f at any point in the domain. Since the streamfunction and vorticity transport equations are subject to Dirichlet boundary conditions only, the matrix $\widehat{\mathcal{K}}$ and the vector $\widehat{e}$ in equation (3.15) are simply set to null.

In the case of Cartesian coordinate system, approximate expressions for ψ and

ω will take the form

$$\psi(x,y) = \sum_{i=1}^{N_x}\sum_{j=1}^{N_y}\varphi_i^{[x]}(x)\varphi_j^{[y]}(y)\,\psi_{i,j}, \tag{3.23}$$

$$\omega(x,y) = \sum_{i=1}^{N_x}\sum_{j=1}^{N_y}\varphi_i^{[x]}(x)\varphi_j^{[y]}(y)\,\omega_{i,j}, \tag{3.24}$$

where $\psi_{i,j}$ and $\omega_{i,j}$ are the values of the ψ and ω variables at the intersection of the ith horizontal grid line and jth vertical grid line; the products $\varphi_i^{[x]}\varphi_j^{[y]}$ are usually referred to as the trial/basis/approximating functions; and N_x and N_y are the numbers of grid lines in the y and x directions, respectively.

The energy equation is subject to both types of boundary conditions. Assume that Dirichlet and Neumann boundary conditions are prescribed on the two vertical and two horizontal walls, respectively. The integral approach allows one to incorporate Neumann boundary conditions into the IRBFN approximations through integration constants. For each y grid line, the matrix $\widehat{\mathcal{K}}$ and the vector $\widehat{e}$ in (3.15) will become

$$\widehat{\mathcal{K}} = \begin{bmatrix} I_1^{(1)}(y_1), & I_2^{(1)}(y_1), & \cdots, & I_{N_y}^{(1)}(y_1), & 1, & 0 \\ I_1^{(1)}\left(y_{N_y}\right), & I_2^{(1)}\left(y_{N_y}\right), & \cdots, & I_{N_y}^{(1)}\left(y_{N_y}\right), & 1, & 0 \end{bmatrix},$$

$$\widehat{e} = \begin{pmatrix} \frac{\partial T_1}{\partial y} \\ \frac{\partial T_{N_y}}{\partial y} \end{pmatrix},$$

leading to

$$T(x,y) = \sum_{i=1}^{N_x}\varphi_i^{[x]}(x)\left(\sum_{j=1}^{N_y}\varphi_j^{[y]}(y)\,T_{i,j} + \varphi_{N_y+1}^{[y]}(y)\,\frac{\partial T_{i,1}}{\partial y} + \varphi_{N_y+2}^{[y]}(y)\,\frac{\partial T_{i,N_y}}{\partial y}\right). \tag{3.25}$$

In (3.25), $T_{i,j}$ is the values of the T variables at the intersection of the ith horizontal grid line and jth vertical grid line; and $\partial T_{i,1}/\partial y$ and $\partial T_{i,N_y}/\partial y$ are nodal derivative boundary conditions.

In the case of cylindrical coordinates, the independent variables x and y in (3.23) - (3.25) will be replaced with r and θ.

3.3.2 Derivation of computation boundary conditions for the vorticity

This section presents a new treatment for the vorticity boundary condition in the discretisation of the $\psi - \omega$ formulation. Boundary conditions are over-specified for the streamfunction equation (3.1)/(3.4), but under-specified for the vorticity transport equation (3.2)/(3.5). There is the need to derive boundary conditions for the vorticity. In practice, the vorticity boundary values are usually derived from their definitions (3.1)/(3.4) and boundary conditions for the streamfunction. Satisfaction of computational boundary conditions for the vorticity will have a strong influence on the accuracy of the final solution.

In the context of FDMs, Thom's formula and its variations have been widely used to obtain the vorticity boundary condition (e.g. Roache, 1982; Weinan and Liu, 1996; Spotz, 1998). These formulae are derived according to a local relation of the vorticity at the boundary. Although their implementations are quite straightforward, results by these formulae are observed to be uncertain in some cases (e.g. lower-order formulae may give better accuracy than high-order ones (Spotz, 1998)). Many other techniques such as the local radial point interpolation method (LRPIM) (Wu and Liu, 2003) and the local RBF-based differential quadrature method (RBF-DQM) (Shu et al., 2003) have also applied these boundary FD schemes, where grids near and including the boundary are required to be orthogonal.

In this study, two boundary vorticity schemes, which are global, are discussed. Taking into account the streamfunction boundary values (i.e. $\psi = 0$), expressions for the vorticity on the boundaries will reduce to

$$\omega = \frac{\partial^2 \psi}{\partial n^2}, \tag{3.26}$$

where n is the local direction normal to the wall. The two schemes presented below are different in the sense that $\partial\psi/\partial n$ is incorporated differently into the RHS of (3.26).

Approach 1: Consider an x grid line. Firstly, the RHS of (3.26) is expressed in terms of $\partial\psi/\partial x$

$$\widehat{\frac{\partial^2 \psi}{\partial x^2}} = \widehat{\mathcal{I}}^{(2)} \left(\widehat{\mathcal{I}}^{(1)}\right)^{-1} \widehat{\frac{\partial \psi}{\partial x}} = \widehat{\mathcal{I}}^{(2)} \left(\widehat{\mathcal{I}}^{(1)}\right)^{-1} \begin{pmatrix} \widehat{\frac{\partial \psi_{ip}}{\partial x}} \\ \frac{\partial \psi_1}{\partial x} \\ \frac{\partial \psi_{N_x}}{\partial x} \end{pmatrix}, \tag{3.27}$$

in which $\widehat{\partial\psi_{ip}}/\partial x$ and $(\partial\psi_1/\partial x, \partial\psi_{N_x}/\partial x)$ are the values of $\partial\psi/\partial x$ at the interior points $(x_2, \cdots, x_{N_x-1})$ and at the two boundary points (x_1, x_{N_x}), respectively. Secondly, the given values of $\partial\psi_1/\partial x$ and $\partial\psi_{N_x}/\partial x$ are substituted into (3.27), leading to

$$\widehat{\frac{\partial^2 \psi}{\partial x^2}} = \widehat{G}_x \widehat{\frac{\partial \psi_{ip}}{\partial x}} + \widehat{k}_x, \tag{3.28}$$

where $\widehat{G}_x$ is a known differentiation matrix in the physical space, and $\widehat{k}_x$ is a known vector whose components are functions of derivative boundary conditions. Thirdly, the first derivative values are written in terms of the nodal

streamfunction values

$$\widehat{\frac{\partial \psi}{\partial x}} = \widehat{\mathcal{I}}^{(1)} \left(\widehat{\mathcal{I}}^{(0)}\right)^{-1} \widehat{\psi} = \widehat{\mathcal{I}}^{(1)} \left(\widehat{\mathcal{I}}^{(0)}\right)^{-1} \begin{pmatrix} \widehat{\psi}_{ip} \\ \psi_1 \\ \psi_{N_x} \end{pmatrix}, \tag{3.29}$$

in which $\widehat{\psi}_{ip}$ and (ψ_1, ψ_{N_x}) are the values of the streamfunction at the interior points and at the boundary points, respectively. Finally, by substituting (3.29) into (3.28), one will obtain computational boundary conditions for the vorticity, which are dependent on the nodal values of ψ at the interior points and at the two end-points of the grid line. For more details, the reader is referred to (Mai-Duy, Mai-Cao and Tran-Cong, 2007).

Approach 2: Here, we propose that the incorporation of $\partial\psi/\partial n$ into the RHS of (3.26) is carried out with the help of the constants of integration. Consider an x grid line. Owing to the fact that the present coefficient vector is larger ($\widehat{\alpha}$ in (3.12)-(3.14) contains two constants of integration), one can add two extra equations representing $\partial\psi_1/\partial x$ and $\partial\psi_{N_x}/\partial x$ to the conversion process

$$\begin{pmatrix} \widehat{\psi} \\ \frac{\partial \psi_1}{\partial x} \\ \frac{\partial \psi_{N_x}}{\partial x} \end{pmatrix} = \begin{bmatrix} \widehat{\mathcal{I}}^{(0)} \\ \widehat{\mathcal{K}} \end{bmatrix} \widehat{\alpha} = \widehat{\mathcal{C}} \widehat{\alpha}, \tag{3.30}$$

in which $\widehat{\mathcal{K}}$ is the matrix made up of the first and last rows of $\widehat{\mathcal{I}}^{(1)}$, i.e.

$$\widehat{\mathcal{K}} = \begin{bmatrix} I_1^{(1)}(x_1), & I_2^{(1)}(x_1), & \cdots, & I_{N_x}^{(1)}(x_1), & 1, & 0 \\ I_1^{(1)}(x_{N_x}), & I_2^{(1)}(x_{N_x}), & \cdots, & I_{N_x}^{(1)}(x_{N_x}), & 1, & 0 \end{bmatrix}.$$

It can be seen from (3.30) that, despite the presence of nodal derivative values, the 1D-IRBFN for ψ is collocated at the whole set of centres on the grid line.

The second derivatives of ψ at the two boundary points can now be expressed in terms of the values of ψ at every point on the grid line and the values of $\partial\psi/\partial x$ at the two boundary points (x_1, x_{N_x})

$$\begin{pmatrix} \frac{\partial^2\psi_1}{\partial x^2} \\ \frac{\partial^2\psi_{N_x}}{\partial x^2} \end{pmatrix} = \widehat{\mathcal{D}}\widehat{\mathcal{C}}^{-1} \begin{pmatrix} \widehat{\psi} \\ \frac{\partial\psi_1}{\partial x} \\ \frac{\partial\psi_{N_x}}{\partial x} \end{pmatrix}, \tag{3.31}$$

where $\widehat{\mathcal{D}}$ is a sub-matrix of $\widehat{\mathcal{I}}^{(2)}$ given by the first and last rows as

$$\widehat{\mathcal{D}} = \begin{bmatrix} I_1^{(2)}(x_1), & I_2^{(2)}(x_1), & \cdots, & I_N^{(2)}(x_1), & 0, & 0 \\ I_1^{(2)}(x_{N_x}), & I_2^{(2)}(x_{N_x}), & \cdots, & I_N^{(2)}(x_{N_x}), & 0, & 0 \end{bmatrix},$$

and $\widehat{\mathcal{C}}$ is defined in (3.30).

It can be seen that the IRBFN approximations for $\partial^2\psi/\partial x^2$ at the boundaries satisfy exactly the prescribed derivative boundary values. With equation (3.31), one can obtain the computational boundary conditions for the vorticity. On a y grid line, the process can be taken in a similar fashion. These boundary condition derivation processes are also applicable to the cylindrical coordinate system.

3.3.3 Galerkin discretisations of the PDEs

The discretisation process for (3.1) - (3.3) is similar to that for (3.4) - (3.6). For brevity, only the former is presented in detail here.

A distinguishing feature of the present method is that the IRBFNs approximations satisfy a priori not only the Dirichlet boundary conditions but also the Neumann boundary conditions. As a result, the Galerkin weighting process applied to (3.1) - (3.3) over the domain Ω simply produces the following results (without the boundary-integral terms)

$$\int_\Omega W\left(\frac{\partial^2\psi}{\partial x^2}+\frac{\partial^2\psi}{\partial y^2}+\omega\right)d\Omega=0, \tag{3.32}$$

$$\int_\Omega W\frac{\partial\omega}{\partial t}d\Omega+\int_\Omega W\left(u_x\frac{\partial\omega}{\partial x}+u_y\frac{\partial\omega}{\partial y}\right)d\Omega - \sqrt{\frac{Pr}{Ra}}\int_\Omega W\left(\frac{\partial^2\omega}{\partial x^2}+\frac{\partial^2\omega}{\partial y^2}\right)d\Omega-\int_\Omega W\frac{\partial T}{\partial x}d\Omega=0, \tag{3.33}$$

$$\int_\Omega W\frac{\partial T}{\partial t}d\Omega+\int_\Omega W\left(u_x\frac{\partial T}{\partial x}+u_y\frac{\partial T}{\partial y}\right)d\Omega - \frac{1}{\sqrt{RaPr}}\int_\Omega W\left(\frac{\partial^2 T}{\partial x^2}+\frac{\partial^2 T}{\partial y^2}\right)d\Omega=0, \tag{3.34}$$

where W are the weighting/test functions which are taken from the set of trial functions (i.e. $W=\varphi_i^{[x]}\varphi_j^{[y]}$, where the values of i and j depend on the equation under consideration as will be shown later). Substituting (3.23) - (3.25) into (3.32) - (3.34), one will obtain the following three sets of algebraic equations

$$A_\psi\{\psi\}+M_\omega\{\omega\} = 0, \tag{3.35}$$

$$M_\omega\{\dot\omega\}+(KU_\omega+KV_\omega)\{\omega\}-\sqrt{\frac{Pr}{Ra}}A_\omega\{\omega\}+\{F_\omega\} = 0, \tag{3.36}$$

$$M_T\left\{\dot T\right\}+(KU_T+KV_T)\{T\}-\frac{1}{\sqrt{RaPr}}A_T\{T\} = 0, \tag{3.37}$$

where $\dot{\omega} = \partial\omega/\partial t$, $\dot{T} = \partial T/\partial t$, $\{\psi\}$ and $\{\omega\}$ the vectors of interior nodal values of ψ and ω, respectively, $\{T\}$ the vector of nodal values of T at the interior points and the Neumann boundary points, and

$$(A_\psi)_{m,n} = \int_\Omega \varphi_m^{[x]}(x)\,\varphi_n^{[y]}(y)\left(\sum_{i=1}^{N_x}\sum_{j=1}^{N_y}\frac{\partial^2\varphi_i^{[x]}(x)}{\partial x^2}\varphi_j^{[y]}(y) + \sum_{i=1}^{N_x}\sum_{j=1}^{N_y}\varphi_i^{[x]}(x)\,\frac{\partial^2\varphi_j^{[y]}(y)}{\partial y^2}\right)d\Omega, \tag{3.38}$$

$$(M_\omega)_{m,n} = \int_\Omega \varphi_m^{[x]}(x)\,\varphi_n^{[y]}(y)d\Omega, \tag{3.39}$$

$$(KU_\omega)_{m,n} = (u_x)_{m,n}\int_\Omega \varphi_m^{[x]}(x)\,\varphi_n^{[y]}(y)\left(\sum_{i=1}^{N_x}\sum_{j=1}^{N_y}\frac{\partial\varphi_i^{[x]}(x)}{\partial x}\varphi_j^{[y]}(y)\right)d\Omega, \tag{3.40}$$

$$(KV_\omega)_{m,n} = (u_y)_{m,n}\int_\Omega \varphi_m^{[x]}(x)\,\varphi_n^{[y]}(y)\left(\sum_{i=1}^{N_x}\sum_{j=1}^{N_y}\varphi_i^{[x]}(x)\,\frac{\partial\varphi_j^{[y]}(y)}{\partial y}\right)d\Omega, \tag{3.41}$$

$$(A_\omega)_{m,n} = \int_\Omega \varphi_m^{[x]}(x)\,\varphi_n^{[y]}(y)\left(\sum_{i=1}^{N_x}\sum_{j=1}^{N_y}\frac{\partial^2\varphi_i^{[x]}(x)}{\partial x^2}\varphi_j^{[y]}(y) + \sum_{i=1}^{N_x}\sum_{j=1}^{N_y}\varphi_i^{[x]}(x)\,\frac{\partial^2\varphi_j^{[y]}(y)}{\partial y^2}\right)d\Omega, \tag{3.42}$$

$$\{F_\omega\}_{m,n} = \frac{\partial T_{m,n}}{\partial x}\int_\Omega \varphi_m^{[x]}(x)\,\varphi_n^{[y]}(y)d\Omega, \tag{3.43}$$

$$(KU_T)_{m,l} = (u_x)_{m,l}\int_\Omega \varphi_m^{[x]}(x)\,\varphi_l^{[y]}(y)\left(\sum_{i=1}^{N_x}\sum_{j=1}^{N_y}\frac{\partial\varphi_i^{[x]}(x)}{\partial x}\varphi_j^{[y]}(y)\right)d\Omega, \tag{3.44}$$

$$(KV_T)_{m,l} = (u_y)_{m,l}\int_\Omega \varphi_m^{[x]}(x)\,\varphi_l^{[y]}(y)\left(\sum_{i=1}^{N_x}\sum_{j=1}^{N_y}\varphi_i^{[x]}(x)\,\frac{\partial\varphi_j^{[y]}(y)}{\partial y}\right)d\Omega, \tag{3.45}$$

$$(A_T)_{m,l} = \int_\Omega \varphi_m^{[x]}(x)\,\varphi_l^{[y]}(y)\left(\sum_{i=1}^{N_x}\sum_{j=1}^{N_y}\frac{\partial^2\varphi_i^{[x]}(x)}{\partial x^2}\varphi_j^{[y]}(y)+\sum_{i=1}^{N_x}\sum_{j=1}^{N_y}\varphi_i^{[x]}(x)\,\frac{\partial^2\varphi_j^{[y]}(y)}{\partial y^2}\right)d\Omega, \tag{3.46}$$

$$(M_T)_{m,l} = \int_\Omega \varphi_m^{[x]}(x)\,\varphi_l^{[y]}(y)d\Omega, \tag{3.47}$$

in which $m = (2, 3, ..., N_x-1)$ (Dirichlet boundary conditions), $n = (2, 3, ..., N_y-1)$ (Dirichlet boundary conditions) and $l = (1, 2, ..., N_y)$ (Neumann boundary conditions). It is noted that this discretisation process leads to symmetric matrices.

The volume integrals above can be evaluated using repeated integrals, for which Gauss quadratures are employed along the grid lines.

3.3.4 Solution procedure

Due to the presence of convection terms (KU_ω, KV_ω, KU_T and KV_T) in the vorticity transport and energy equations, the resultant coupled sets of equations are nonlinear. We will adopt a time-marching approach, where the diffusion and convection terms are treated implicitly and explicitly, respectively. All equations involve the Laplacian term and their discrete form remains unchanged during the solution process. Moreover, the two matrices A_ψ and A_ω are identical. At each time level, the three equations are solved separately for efficiency purposes. The solution procedure can be summarised as follows.

1. Guess values of T, ψ, ω and their first-order spatial derivatives at time $t = 0$

2. Discretise spatial derivatives using 1D-IRBFNs, resulting in a high-order

approximation scheme in space

3. Discretise time derivatives using Euler (forward difference) method, resulting in a first-order accurate scheme in time

4. Compute the boundary conditions for ω and the convective terms

5. Solve the energy equation (3.37) for T, subject to Dirichlet and Neumann conditions

   Solve the vorticity equation (3.36) for ω, subject to Dirichlet conditions

   Solve the streamfunction equation (3.35) for ψ, subject to Dirichlet conditions

6. Check to see whether the solution has reached a steady state

$$\frac{\sqrt{\sum_{i=1}^{N}\left(T_i^{(k)}-T_i^{(k-1)}\right)^2}}{\sqrt{\sum_{i=1}^{N}\left(T_i^{(k)}\right)^2}}<\epsilon, \tag{3.48}$$

   where k is the time level and ϵ is a prescribed tolerance

7. If it is not satisfied, advance time step and repeat from step 3. Otherwise, stop the computation and output the results.

3.4 Numerical results

Several test problems are considered to validate the proposed technique. The first problem is for the treatment of the vorticity boundary condition, while the last two problems, namely natural convection in a square slot and in a concentric annulus, are employed to study the accuracy of the method. For all numerical examples, uniform rectangular grids are used to represent the computational

domain, and 1D-IRBFNs are implemented with the MQ function

$$g_i(\eta) = \sqrt{(\eta - c_i)^2 + a_i^2},$$

where c_i and a_i are the centre and the width/shape-parameter of the ith MQ-RBF. The MQ width is simply chosen to be the grid size.

3.4.1 Problem 1 (vorticity boundary condition)

The two approaches, namely Approach 1 and Approach 2, for the treatment of boundary conditions for the vorticity are investigated here numerically by employing test problems whose solutions are available in analytic form. Errors, which can be measured exactly, are computed using the relative discrete L_2 norm of the error (denoted by N_e). Consider the following governing equations

$$\frac{\partial^2 \psi}{\partial x^2} + \frac{\partial^2 \psi}{\partial y^2} = -\omega, \tag{3.49}$$

$$\frac{\partial^2 \omega}{\partial x^2} + \frac{\partial^2 \omega}{\partial y^2} = f(x, y), \tag{3.50}$$

with two cases of boundary condition.

Homogeneous boundary conditions: For this case, the problem domain is a unit square ($\Omega = [0, 1] \times [0, 1]$) and the exact solution is taken as

$$\widetilde{\psi}(x, y) = [1 - \cos(2\pi x)][1 - \cos(2\pi y)], \tag{3.51}$$

from which one can easily derive analytic forms for $\omega(x, y)$ and $f(x, y)$ on the RHSs of (3.49) and (3.50), respectively. Values of ψ and $\partial\psi/\partial n$ are all zero along the boundaries.

Numerical results for the solutions ψ and ω shown in Table 3.1 indicate that the

proposed treatment (Approach 2) results in a significant improvement in accuracy. It can be seen that one order of magnitude better is generally observed for all grids used. For example, at a grid of 61×61, the N_e errors of ω are 2.0×10^{-4} and 3.9×10^{-5} for Approach 1 and Approach 2, respectively. Computational boundary conditions for the vorticity thus have a strong influence on the accuracy of the final solutions.

Inhomogeneous boundary conditions: For this case, the exact solution is taken as

$$\widetilde{\psi}(x, y) = \sin(2\pi x)\cos(2y) - \cos(2\pi x)\sinh(2y), \tag{3.52}$$

on domain $\Omega = [-1, 1] \times [-1, 1]$. Results obtained are given in Table 3.2. Again, Approach 2 outperforms Approach 1 regarding accuracy. Approach 2 is recommended for use in practice. In the following, only Approach 2 is employed.

Table 3.1: Problem 1 (homogeneous boundary conditions): N_e errors of the solution ψ and ω. Notice that a(-b) means $a \times 10^{-b}$

	Errors of ω		Errors of ψ	
Grid	Approach 1	Approach 2	Approach 1	Approach 2
6×6	1.168(-1)	2.808(-2)	1.460(-1)	3.547(-2)
11×11	1.687(-2)	2.985(-3)	2.238(-2)	3.835(-3)
21×21	2.680(-3)	5.075(-4)	3.712(-3)	6.951(-4)
31×31	9.917(-4)	1.903(-4)	1.401(-3)	2.671(-4)
41×41	5.034(-4)	9.718(-5)	7.187(-4)	1.381(-4)
51×51	3.016(-4)	5.840(-5)	4.334(-4)	8.363(-5)
61×61	1.999(-4)	3.879(-5)	2.887(-4)	5.584(-5)

Table 3.2: Problem 1 (inhomogeneous boundary conditions): N_e errors of the solution ψ and ω. Notice that a(-b) means $a \times 10^{-b}$

	Errors of ω		Errors of ψ	
Grid	Approach 1	Approach 2	Approach 1	Approach 2
6×6	6.096(-1)	1.845(-1)	2.137(0)	6.046(-1)
11×11	3.788(-2)	1.271(-2)	7.389(-2)	2.406(-2)
21×21	8.719(-3)	2.986(-3)	1.088(-2)	3.639(-3)
31×31	4.189(-3)	1.433(-3)	4.337(-3)	1.454(-3)
41×41	2.518(-3)	8.605(-4)	2.325(-3)	7.804(-4)
51×51	1.701(-3)	5.807(-4)	1.449(-3)	4.866(-4)
61×61	1.235(-3)	4.212(-4)	9.894(-4)	3.324(-4)

3.4.2 Problem 2: Natural convection in a square slot

This problem is schematically defined in Figure 3.1. The direction of gravity is parallel to the vertical walls. The problem is solved in Cartesian coordinates with the governing equations being (3.1) - (3.3). All walls are stationary, leading to $\psi = \partial\psi/\partial n = 0$ on the boundaries. The two horizontal walls are adiabatic (i.e. $\partial T/\partial y = 0$), while the two vertical walls are maintained at constant temperatures (i.e. $T = +0.5$ (left wall) and $T = -0.5$ (right wall)).

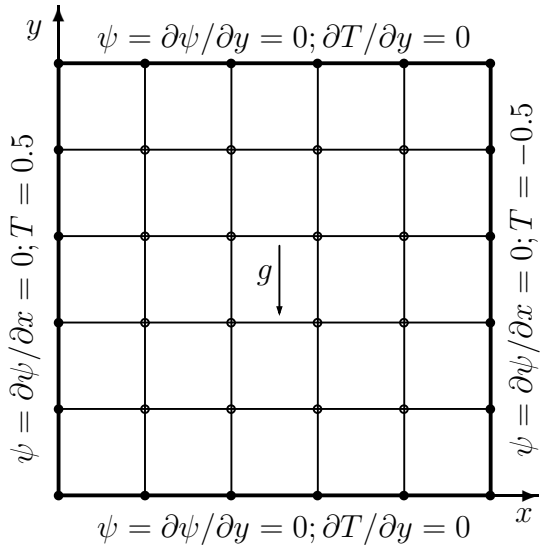

Figure 3.1: Problem 2, natural convection flow in a square slot: geometry definition, boundary conditions and discretisation. Note that $\partial\psi/\partial x = \partial\psi/\partial y = 0$ are used to compute the boundary conditions for ω.

Numerical results for this problem are extensive. A range of Ra from 10^3 to 10^6 has been widely used for the validation of new numerical schemes. Davis (1983) provided finite-difference results which are often cited in the literature for comparison purposes. Later on, there are increased levels of interest for higher values of Ra, namely 10^7 and 10^8. Works reported include the pseudo-spectral method (Quéré, 1991), FEM (Wan et al., 2001), $h-$adaptive FEM (Mayne et al., 2000, 2001), discrete singular convolution (DSC) method (Wan et al., 2001), mesh-

less diffuse approximation method (DAM) (Sadat and Couturier, 2000), and mesh-free local RBF collocation method (RBFCM) (Kosec and Šarler, 2007). For this higher range of Ra values, it has been generally observed that (i) the strength of boundary layers is significantly increased; (ii) convergence becomes much more difficult; and (iii) significant discrepancies in the Nusselt number occur in some cases (e.g. between the pseudo-spectral technique (Quéré, 1991) and the DSC method (Wan et al., 2001)).

The Galerkin-IRBFN method is employed to study this problem for $10^3 \leq Ra \leq 10^8$. Results are presented in the form of contour plots for ψ, ω and T and through the values of the following quantities

- The average Nusselt numbers on the vertical plane at $x = 0$ (left wall) and at $x = 1/2$ (middle cross-section), which are defined by

$$\begin{aligned} Nu_0 &= Nu(x = 0, y), \\ Nu_{1/2} &= Nu(x = 1/2, y), \end{aligned}$$

  in which

$$Nu\,(x, y) = \int_0^1 \left(u_x T - \frac{\partial T}{\partial x} \right) dy. \tag{3.53}$$

- The average Nusselt number throughout the cavity, which is defined by

$$\overline{Nu} = \int_0^1 Nu(x, y) dx. \tag{3.54}$$

- Maximum Nusselt number, Nu_{max}, on the plane $x = 0$ and its location
- Minimum Nusselt number, Nu_{min}, on the plane $x = 0$ and its location

It is noted that integrals (3.53) and (3.54) are computed here using Simpson's rule.

Results for Ra from 10^3 to 10^6 are presented in Table 3.3 and Figures 3.2 - 3.4, and they are compared with those of Davis (1983). Denser grids are needed for higher values of Ra. When compared with low-order methods, the proposed technique requires relatively-coarse grids for the same level of accuracy. Results concerning the Nusselt numbers are shown in Table 3.3, where a fast convergence is observed. Figures 3.2 - 3.4 show the distributions of the streamfunction, vorticity and temperature fields, which are all in good qualitative agreement with the benchmark results. For example, the three fields are skew-symmetric with respect to the centre of the slot, and the isotherms are nearly horizontal in the core flow as the Rayleigh number increases.

Results for Ra from 10^7 to 10^8 are presented in Table 3.4, Figure 3.5 and Figure 3.6. Table 3.4 shows a comparison of the average Nusselt numbers between the present method and several other methods. It can be seen that there are significant discrepancies among various numerical techniques. For the case of $Ra = 10^7$, the DSC (Wan et al., 2001) and FEM (Manzari, 1999) produced values of 13.86 and 13.99 for the average Nusselt number, while the pseudo-spectral (Quéré, 1991), FE (Wan et al., 2001), DA (Sadat and Couturier, 2000) and RBFCM (Kosec and Šarler, 2007) techniques yielded the following values: 16.523, 16.656, 16.59 and 16.92. The differences between the two groups are much wider for the case of $Ra = 10^8$: 23.67 for the DSC method, and (30.225, 31.486, 30.94, 32.12) for the second group. The Galerkin-IRBFN results are in close agreement with the second group, particularly with the pseudo-spectral technique (Quéré, 1991). Variations of the local Nusselt number on the left and right walls are presented in Figure 3.7. It is clearly shown that the proposed technique is able to capture very steep changes of the local Nusselt number in the region close to the boundary. It can be seen from Figures 3.5 - 3.6 that the present contour plots for the streamfunction, vorticity and temperature variables look feasible when compared with those of the pseudo-spectral technique (Quéré, 1991). Very thin boundary layers are formed at these high values of Ra. It is noted that iso-values used in these plots are the same as those used in (Quéré, 1991).

Table 3.3: Problem 2, natural convection flow in a square slot: Comparison of the Galerkin-IRBFN results with the benchmark solution of Davis (1983) for $10^3 \leq Ra \leq 10^6$ and $Pr = 0.71$

		Characteristic values						
Ra	Grid size	$\overline{Nu}$	$Nu_{1/2}$	Nu_0	Nu_{max}	y	Nu_{min}	y
10^3	21×21	1.118	1.119	1.117	1.503	0.094	0.693	1
	(Davis, 1983)	1.118	1.118	1.117	1.505	0.092	0.692	1
10^4	21×21	2.254	2.258	2.242	3.514	0.149	0.592	1
	31×31	2.249	2.251	2.244	3.526	0.147	0.588	1
	41×41	2.247	2.248	2.244	3.529	0.146	0.587	1
	(Davis, 1983)	2.243	2.243	2.238	3.528	0.143	0.586	1
10^5	31×31	4.552	4.555	4.521	7.682	0.083	0.744	1
	41×41	4.539	4.540	4.519	7.689	0.086	0.736	1
	51×51	4.533	4.534	4.520	7.706	0.084	0.733	1
	61×61	4.529	4.530	4.521	7.712	0.083	0.731	1
	(Davis, 1983)	4.519	4.519	4.509	7.717	0.081	0.729	1
10^6	41×41	8.934	8.935	9.023	18.506	0.046	1.025	1
	51×51	8.899	8.900	8.872	17.794	0.041	1.008	1
	61×61	8.877	8.878	8.835	17.523	0.039	1.000	1
	71×71	8.864	8.865	8.827	17.458	0.040	0.993	1
	(Davis, 1983)	8.8	8.799	8.817	17.925	0.038	0.989	1

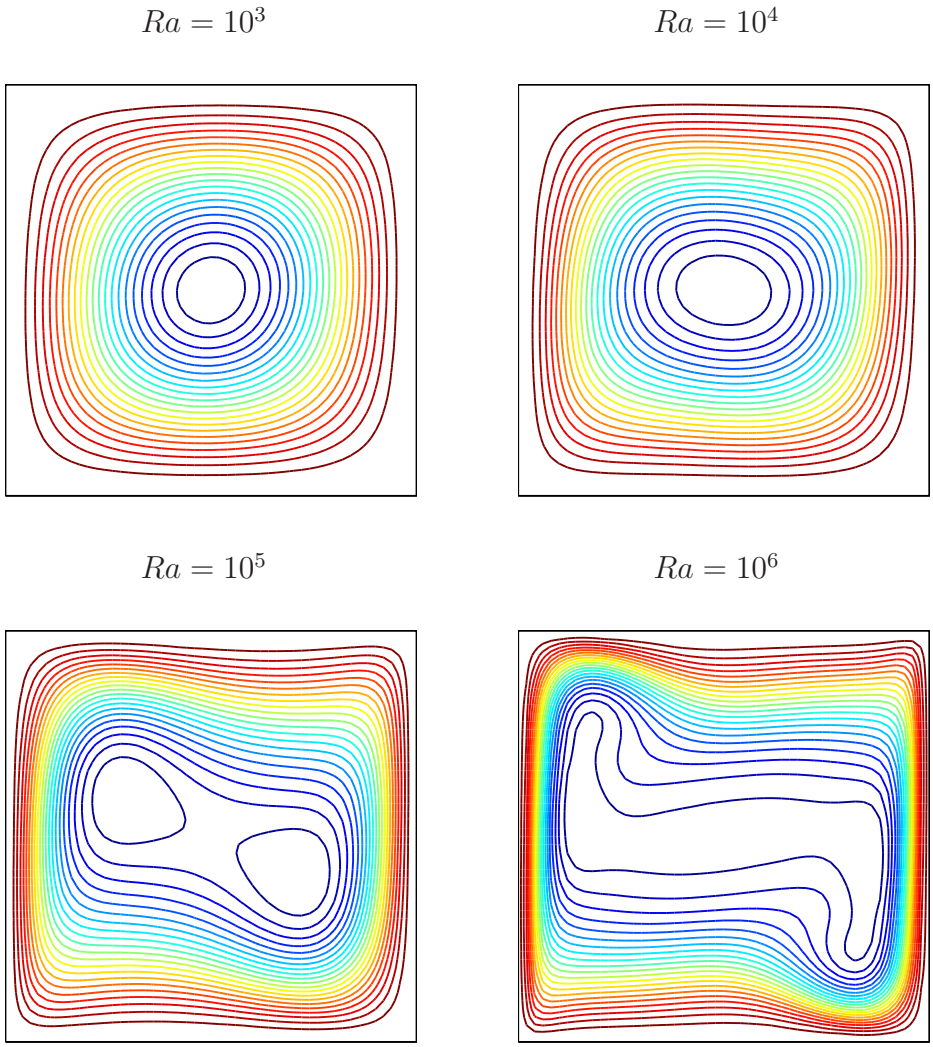

Figure 3.2: Problem 2, natural convection flow in a square slot: Contour plots for the ψ variable at four different values of Ra using a grid of 51×51. Each plot draws 21 contour lines whose values vary uniformly from the minimum to maximum values.

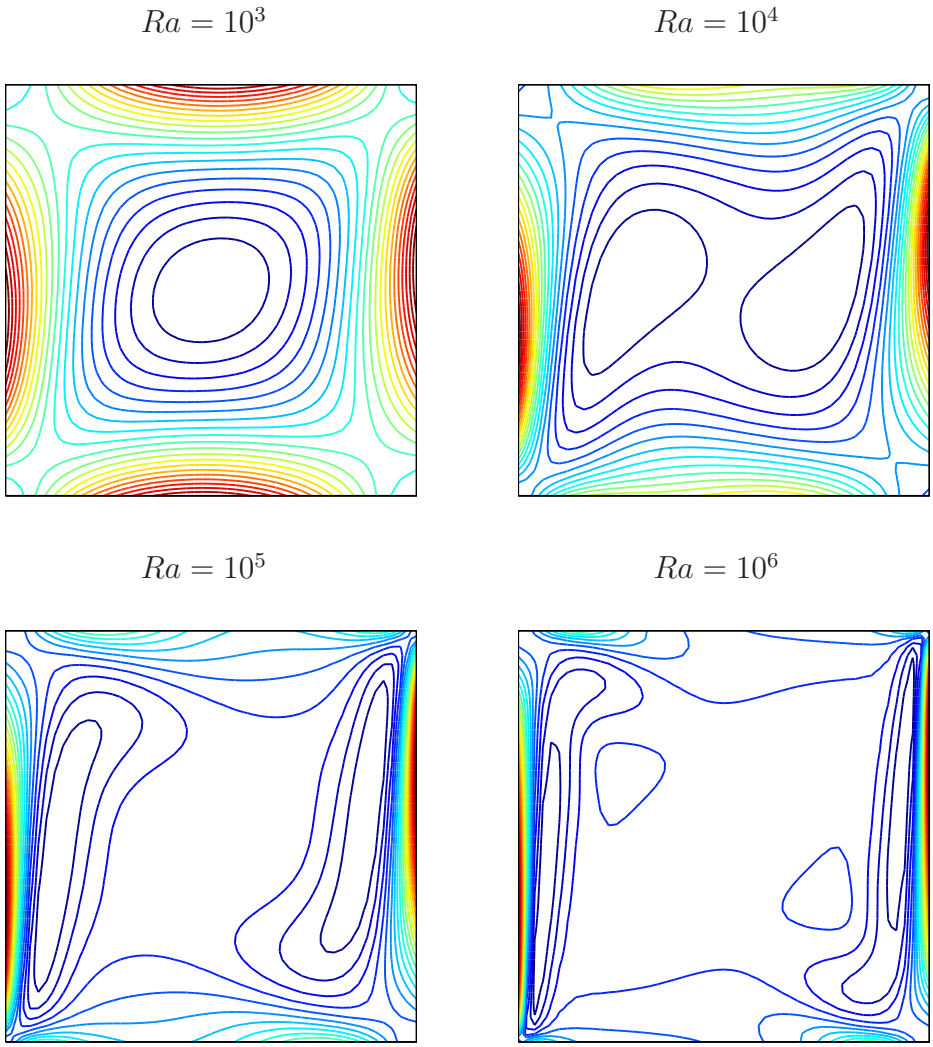

Figure 3.3: Problem 2, natural convection flow in a square slot: Contour plots for the ω variable at four different values of Ra using a grid of 51×51. Each plot draws 21 contour lines whose values vary uniformly from the minimum to maximum values.

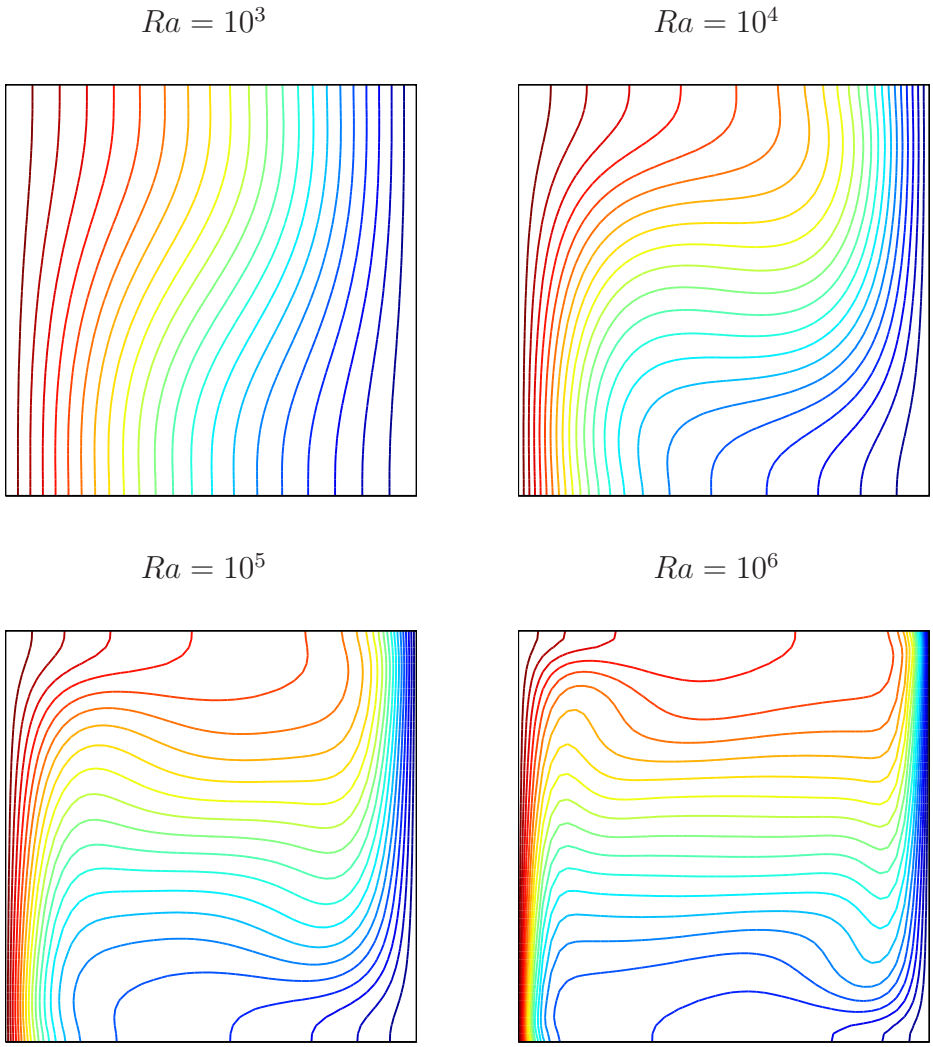

Figure 3.4: Problem 2, natural convection flow in a square slot: Contour plots for the T variable at four different values of Ra using a grid of 51×51. Each plot draws 21 contour lines whose values vary uniformly from the minimum to maximum values.

Table 3.4: Problem 2, natural convection flow in a square slot: Comparison of the Galerkin-IRBFN results with those of other techniques for the two highest values of Ra

Ra	Technique	$\overline{Nu}$	$Nu_{1/2}$
10^7	Present study	16.661	16.661
	(Grid size: 91×91)		
	(Quéré, 1991)	16.523	16.523
	(Manzari, 1999)	13.99	
	(Sadat and Couturier, 2000)	16.59	
	(Wan et al., 2001) (FEM)	16.656	
	(Wan et al., 2001) (DSC)	13.86	
	(Kosec and Šarler, 2007)	16.92	
10^8	Present study	30.548	30.525
	(Grid size: 91×91)		
	(Quéré, 1991)	30.225	30.225
	(Sadat and Couturier, 2000)	30.94	
	(Wan et al., 2001) (FEM)	31.486	
	(Wan et al., 2001) (DSC)	23.67	
	(Kosec and Šarler, 2007)	32.12	

Streamlines

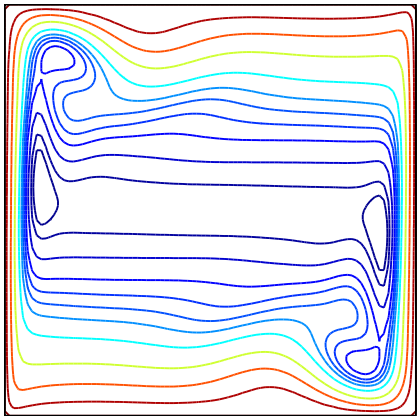

Iso-vorticity lines

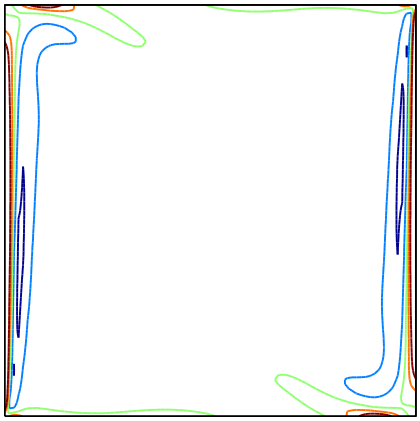

Isotherms

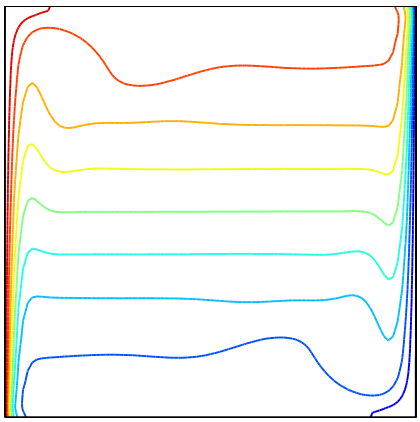

Figure 3.5: Problem 2, natural convection flow in a square slot: Contour plots for the ψ, ω and T variables at $Ra = 10^7$ using a grid of 91×91. Iso-values used in these plots are the same as those in (Quéré, 1991).

Streamlines

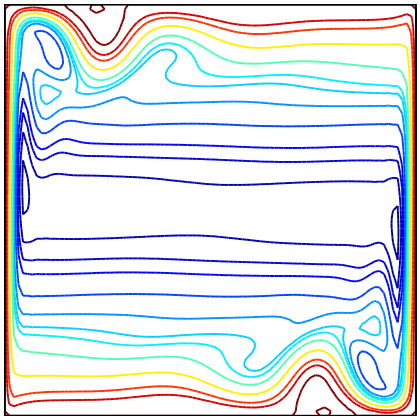

Iso-vorticity lines

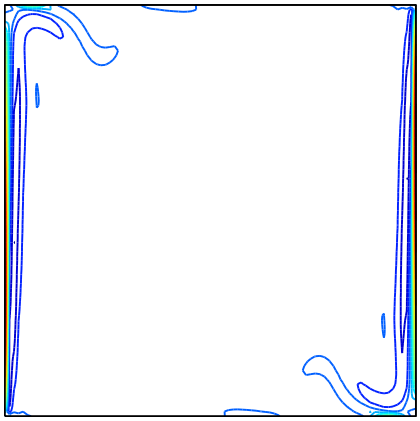

Isotherms

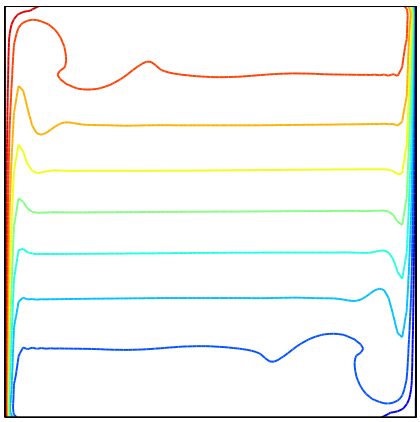

Figure 3.6: Problem 2, natural convection flow in a square slot: Contour plots for the ψ, ω and T variables at $Ra = 10^8$ using a grid of 91×91. Iso-values used in these plots are the same as those in (Quéré, 1991).

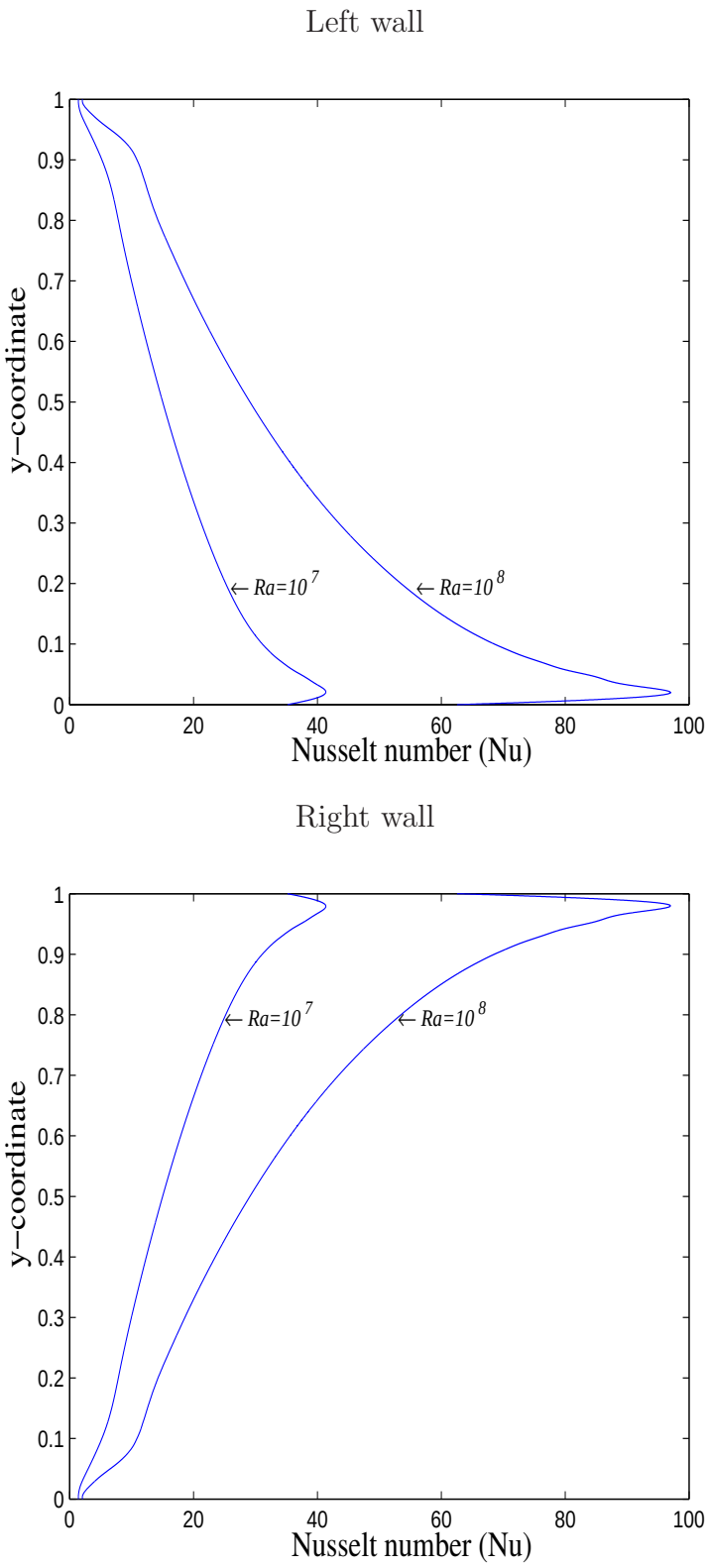

Figure 3.7: Problem 2, natural convection flow in a square slot: Variations of the local Nusselt number along the left and right walls.

3.4.3 Problem 3: Natural convection in a concentric annulus

Consider natural convection between two concentric cylinders that are separated by a distance L, the inner cylinder is heated and the outer cylinder cooled. Most reported cases have been for $Pr = 0.71$ and $L/D_i = 0.8$, in which D_i is the diameter of the inner cylinder. These conditions are also employed in the present work.

Since the flow is symmetric with respect to the vertical centreline, only half of the domain needs be discretised. We employ cylindrical coordinates to solve this problem. Figure 3.8 schematically shows the domain of analysis, the computational domain, a typical dicretisation used and the boundary conditions. The governing equations are employed in the form of (3.4) - (3.6), subject to the following boundary conditions

- on the symmetry plane: $\psi = 0,\ \omega = 0 \quad \text{and} \quad \partial T/\partial\theta = 0,$
- on the outer cylinder: $\psi = 0,\ \partial\psi/\partial r = 0 \quad \text{and} \quad T = 0,$
- on the inner cylinder: $\psi = 0,\ \partial\psi/\partial r = 0 \quad \text{and} \quad T = 1.$

This problem was studied in detail by various techniques. Among them are FDM (Kuehn and Glodstein, 1976), the differential quadrature (DQ) method (Shu, 1999) and the RBF-based DQ method (Shu et al., 2003; Shu and Wu, 2007) whose results are utilised here for comparison purposes.

This problem is studied for the following values of Ra: $10^2, 10^3, 3 \times 10^3, 6 \times 10^3, 10^4, 5 \times 10^4$ and 7×10^4. Contour plots for the streamfunction and temperature are shown in Figures 3.9–3.11, which look feasible in comparison with those of Kuehn and Glodstein (1976). When the Rayleigh number increases, the centre of rotation of the flows is observed to shift upward and the pattern of

the temperature field becomes more complicated. At high values of Ra (5×10^4 and 7×10^4), thermal boundary layers appear near the lower portion of the inner cylinder and the top of the outer cylinder.

Another important result is the average equivalent conductivity denoted by $\overline{k}_{eq}$. This quantity is defined as the actual heat flux divided by the heat flux that would occur by pure conduction in the absence of the fluid motion:

$$\overline{k}_{eqi} = \frac{-\ln\left(R_o/R_i\right)}{\pi\left(R_o/R_i - 1\right)} \int_0^{\pi} \frac{\partial T}{\partial r} d\theta, \tag{3.55}$$

for the inner cylinder, and

$$\overline{k}_{eqo} = \frac{-\left(R_o/R_i\right)\ln\left(R_o/R_i\right)}{\pi\left(R_o/R_i - 1\right)} \int_0^{\pi} \frac{\partial T}{\partial r} d\theta, \tag{3.56}$$

for the outer cylinder, in which R_i and R_o are the radii of the inner and outer cylinders, respectively. Table 3.5 summarises the Galerkin-IRBFN results for various Rayleigh numbers using several grids and those of FDM (Kuehn and Glodstein, 1976) and DQM (Shu, 1999), which shows good agreement between the methods for both the outer and inner cylinders.

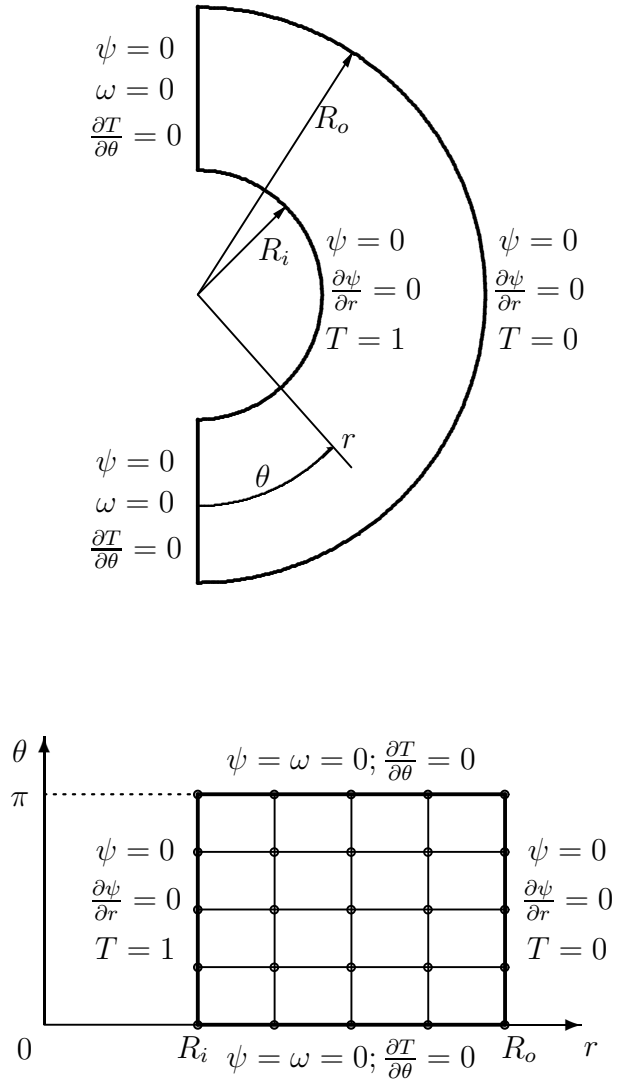

Figure 3.8: Problem 3, natural convection flow in an annulus: domain of interest (upper figure), computational domain (lower figure), boundary conditions and discretisation

Table 3.5: Problem 3, natural convection flow in an annulus: Convergence of the computed average equivalent conductivities with grid refinement for $10^2 \leq Ra \leq 7 \times 10^4$.

Ra	Grid size	Outer cylinder $\overline{k}_{eqo}$	Inner cylinder $\overline{k}_{eqi}$
10^2	11×11	1.000	1.000
	21×21	1.001	1.001
	(Kuehn and Glodstein, 1976)	1.002	1.000
	(Shu, 1999)	1.001	1.001
10^3	31×31	1.077	1.079
	41×41	1.078	1.080
	51×51	1.079	1.080
	(Kuehn and Glodstein, 1976)	1.084	1.081
	(Shu, 1999)	1.082	1.082
3×10^3	31×31	1.373	1.379
	41×41	1.378	1.384
	51×51	1.381	1.387
	(Kuehn and Glodstein, 1976)	1.402	1.404
	(Shu, 1999)	1.397	1.397
6×10^3	31×31	1.676	1.689
	41×41	1.684	1.697
	51×51	1.690	1.701
	(Kuehn and Glodstein, 1976)	1.735	1.736
	(Shu, 1999)	1.715	1.715
10^4	41×41	1.937	1.959
	51×51	1.945	1.964
	61×61	1.953	1.967
	(Kuehn and Glodstein, 1976)	2.005	2.010
	(Shu, 1999)	1.979	1.979
5×10^4	41×41	2.794	2.938
	51×51	2.835	2.943
	61×61	2.866	2.946
	(Kuehn and Glodstein, 1976)	2.973	3.024
	(Shu, 1999)	2.958	2.958
7×10^4	41×41	2.970	3.174
	51×51	3.027	3.180
	61×61	3.070	3.182
	(Kuehn and Glodstein, 1976)	3.226	3.308

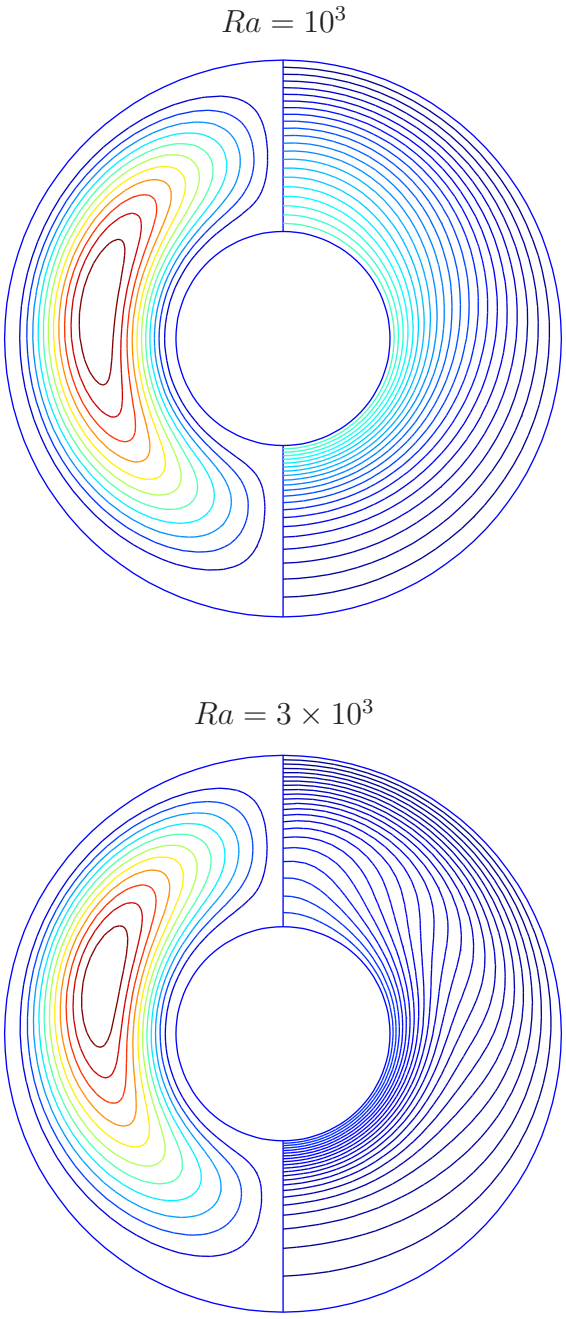

Figure 3.9: Problem 3, natural convection flow in an annulus: Contour plots for the ψ (left) and T (right) variables at $Ra = 10^3$ and $Ra = 3 \times 10^3$ using a grid of 51×51.

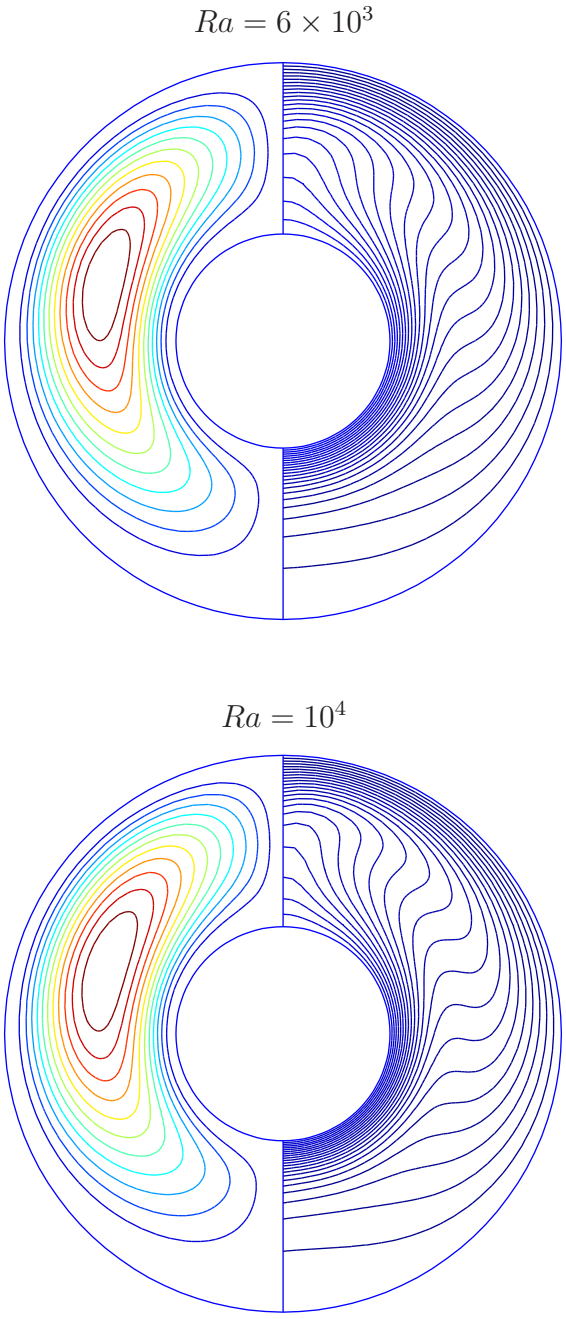

Figure 3.10: Problem 3, natural convection flow in an annulus: Contour plots for the ψ (left) and T (right) variables at $Ra = 6 \times 10^3$ and $Ra = 10^4$ using a grid of 51×51.

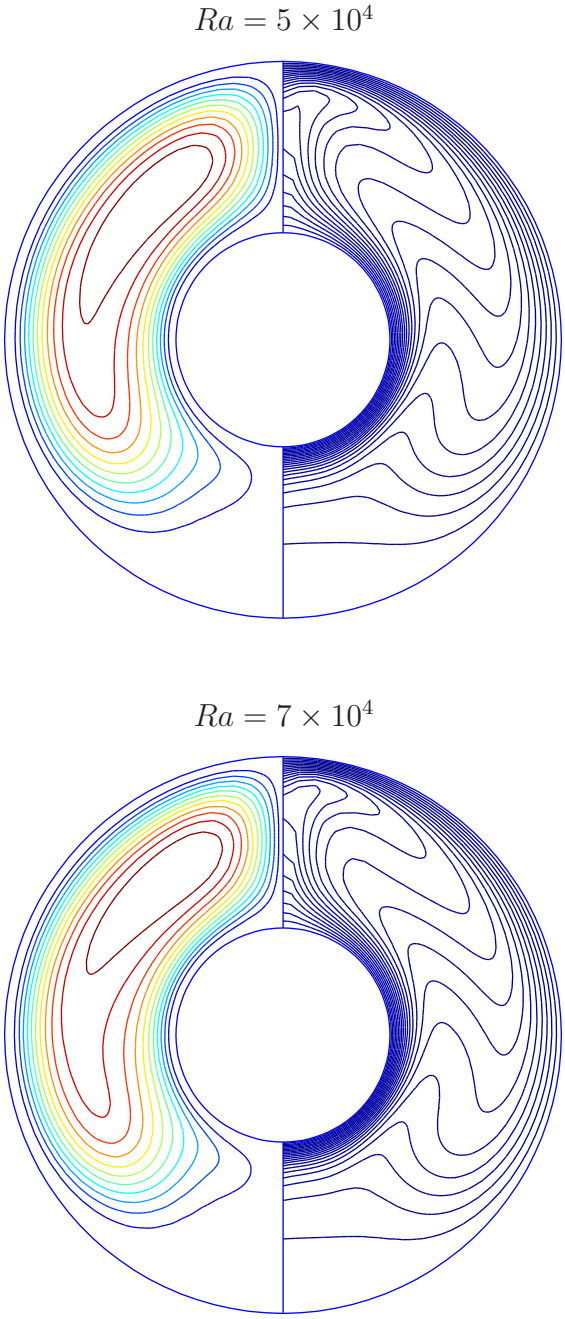

Figure 3.11: Problem 3, natural convection flow in an annulus: Contour plots for the ψ (left) and T (right) variables at $Ra = 5 \times 10^4$ and $Ra = 7 \times 10^4$ using a grid of 51×51.

3.5 Concluding Remarks

We have successfully implemented a Galerkin-IRBFN method for the simulation of natural convection governed by the streamfunction-vorticity formulation in two dimensions. Its attractive features include: (i) easy implementation; (ii) effective treatment of the vorticity boundary condition; (iii) effective handling of the Neumann boundary condition; and (iv) ability to capture very thin boundary layers using relatively-coarse grids. Numerical experiments show that the proposed method achieves very high Ra solutions. It appears that this work is one of the earliest RBF reports which have successfully simulated the flow in a square slot at $Ra = 10^8$.

Chapter 4

1D-IRBFN-based Galerkin method for the streamfunction formulation governing viscous flows

The 1D-IRBFN-based Galerkin method is now further developed for the discretisation of thermally-driven flows of a Newtonian fluid, which are governed by a set of the biharmonic equation for the streamfunction variable and the harmonic equation for the temperature variable. The field variables are approximated by global high-order 1D-IRBFNs on uniform grids without suffering from Runge's phenomenon. All boundary conditions including double boundary conditions, which can be of complicated shapes, for the streamfunction equation are imposed in an exact manner (they are satisfied identically). The proposed technique is validated through the solution of several test problems, including a benchmark buoyancy-driven flow in a square slot. Good accuracy and fast convergence are obtained.

4.1 Introduction

Many science and engineering problems including the deformation of thin plates, the motion of fluids, the transport of chemicals in porous media and the combination of fundamental processes (e.g. particulate suspensions) can be governed by the biharmonic equation (Selvadurai, 2000, 2002). Solving biharmonic problems numerically typically involves significant challenges with respect to the approximation of high-order derivatives and the imposition of double boundary conditions.

A Galerkin formulation is a powerful approach for the discretisation of differential problems. The weighting functions are chosen from a set of trial functions, usually leading to a symmetric system of algebraic equations. Owing to its integral nature, another attractive feature of the Galerkin formulation lies in its smoothing capability. The literature on Galerkin solutions to biharmonic problems is extensive.

In the context of Galerkin finite-element methods (Zienkiewicz and Taylor, 1991), the discretisations of the Galerkin formulation for Dirichlet biharmonic problems require C^1 continuity of the shape functions. The field variable and its first partial derivatives need to be continuous over the problem domain. Such shape functions are much more difficult to construct than those needed for C^0 continuity. As a result, alternative approaches have been developed, including the use of non-conforming/incompatible finite elements and mixed formulations. For the latter, for example, (i) one can approximate the field variable and its gradient using independent interpolations with their relation imposed as a special constraint; and (ii) one can introduce a new variable such as the one involving second derivatives to avoid the necessity of C^1 continuity.

In the context of Galerkin spectral methods (Canuto et al., 1988), the trial functions are required to individually satisfy the boundary conditions. It is difficult

to hold this property for the case of non-homogeneous boundary conditions. In such a case, the tau method is a preferred option. Some equations in the final system are set to use for the imposition of boundary conditions. The Galerkin equation is thus not considered for all weighting functions (the highest-order equations are dropped), leading to a supplementary error. Solutions by both Galerkin and tau methods are approximated in terms of the expansion coefficients.

In this chapter, we present a Galerkin approach, in which IRBFNs in one dimension are utilised as trial functions, for natural convection flows. For conventional interpolation schemes, the order of accuracy for the approximation of a derivative function is known to be a decreasing function of derivative order. It is expected that the use of integration to construct the RBF approximations (i.e. IRBFNs) overcomes the problem of reduced convergence rate caused by differentiation. The employment of IRBFNs in one dimension is much more economical than that in higher dimensions as the number of RBFs used to construct the approximations for a nodal point is significantly reduced. A distinguishing feature of the proposed method is that the 1D-IRBFN trial functions are constructed to identically satisfy (i) not only function values but also normal derivative values at the boundary points (i.e. double boundary conditions) for the streamfunction equation; and (ii) derivative/function values at the boundary points for the temperature equation. Moreover, Cartesian grids made of equally-spaced points can be used to generate the trial and test spaces. By applying tensor products, all derivatives derived from 1D-IRBFNs are defined and continuous throughout the entire problem domain. The unknown vectors in the present 1D-IRBFN-Galerkin method consists of nodal values of the field variable (streamfunction/temperature) at the interior nodes. Numerical results indicate that the present technique yields a high level of accuracy and a fast rate of convergence with increasing number of RBFs.

The remainder of the chapter is organised as follows. A brief description of

the governing equations expressed in terms of the streamfunction and temperature variables only (the streamfunction-temperature formulation) is given in Section 4.2. Section 4.3 presents the proposed 1D-IRBFN-Galerkin method for the simulation of thermally-driven viscous flows. Special attention is given to the discretisation of the biharmonic equation. The accuracy of the method is numerically studied by considering several test problems in Section 4.4. Section 4.5 concludes the chapter.

4.2 Governing equations

The governing equations (1.1), (1.2) and (1.4) for viscous flows are written in the streamfunction-temperature form in two dimensions. Using the Boussinesq approximation, the dimensionless form of the governing equations can be written in the Cartesian coordinates as

$$\begin{aligned} \frac{\partial^4\psi}{\partial x^4} + 2\frac{\partial^4\psi}{\partial x^2\partial y^2} + \frac{\partial^4\psi}{\partial y^4} &= \sqrt{\frac{Ra}{Pr}}\left(\frac{\partial\psi}{\partial y}\left(\frac{\partial^3\psi}{\partial x^3} + \frac{\partial^3\psi}{\partial x\partial y^2}\right)\right. \\ &- \left.\frac{\partial\psi}{\partial x}\left(\frac{\partial^3\psi}{\partial x^2\partial y} + \frac{\partial^3\psi}{\partial y^3}\right) + \frac{\partial T}{\partial x}\right), \qquad (4.1) \\ \frac{\partial^2 T}{\partial x^2} + \frac{\partial^2 T}{\partial y^2} &= \sqrt{RaPr}\left(\frac{\partial\psi}{\partial y}\frac{\partial T}{\partial x} - \frac{\partial\psi}{\partial x}\frac{\partial T}{\partial y}\right), \qquad (4.2) \end{aligned}$$

where ψ is the stream function, T the temperature, and Pr and Ra the Prandtl and Rayleigh numbers, respectively. Pr and Ra are defined as $Pr = \nu/\alpha$ and $Ra = \beta g \Delta T L^3/\alpha\nu$, in which ν is the kinematic viscosity, α the thermal diffusivity, β the thermal expansion coefficient, g the gravity, and L and ΔT the characteristic length and temperature difference, respectively. It is noted that the velocity components u_x and u_y are defined in terms of the streamfunction

as

$$u_x = \frac{\partial \psi}{\partial y}, \quad u_y = -\frac{\partial \psi}{\partial x}.$$

4.3 1D-IRBFN-based Galerkin technique

Let the problem domain Ω be rectangular. We employ a Cartesian grid of $N_x \times N_y$ to represent Ω and 1D-IRBFNs to approximate the streamfunction and temperature variables on each grid line. The governing equations (4.1) and (4.2) are discretised by means of the Galerkin formulation. In the following, details are presented for three main parts: (i) 1D-IRBFN representations of the field variables; (ii) Imposition of boundary conditions; and (iii) Galerkin discretisation of the governing equations.

4.3.1 One-dimensional IRBFN representations of the field variables

The governing equations for thermally-driven flows contain one fourth order PDE (i.e. (4.1)) and one second order PDE (i.e. (4.2)). We employ 1D-IRBFNs of fourth and second order to discretise (4.1) and (4.2), respectively. Consider an η grid line (η represents x or y).

Fourth-order 1D-IRBFNs

Making use of (2.52)-(2.55) with $p = 4$ and $f \equiv \psi$, the following approximate expressions are obtained

$$\frac{d^4\psi(\eta)}{d\eta^4} = \sum_{i=1}^{N_\eta} w_i g_i(\eta) = \sum_{i=1}^{N_\eta} w_i I_i^{(4)}(\eta), \tag{4.3}$$

$$\frac{d^3\psi(\eta)}{d\eta^3} = \sum_{i=1}^{N_\eta} w_i I_i^{(3)}(\eta) + C_1, \tag{4.4}$$

$$\frac{d^2\psi(\eta)}{d\eta^2} = \sum_{i=1}^{N_\eta} w_i I_i^{(2)}(\eta) + C_1\eta + C_2, \tag{4.5}$$

$$\frac{d\psi(\eta)}{d\eta} = \sum_{i=1}^{N_\eta} w_i I_i^{(1)}(\eta) + C_1\frac{\eta^2}{2} + C_2\eta + C_3, \tag{4.6}$$

$$\psi(\eta) = \sum_{i=1}^{N_\eta} w_i I_i^{(0)}(\eta) + C_1\frac{\eta^3}{6} + C_2\frac{\eta^2}{2} + C_3\eta + C_4, \tag{4.7}$$

where $\{w_i\}_{i=1}^{N_\eta}$ is the set of network weights, and $\{g_i(\eta)\}_{i=1}^{N_\eta} \equiv \left\{I_i^{(4)}(\eta)\right\}_{i=1}^{N_\eta}$ the set of RBFs, N_η the number of points, $I_i^{(3)}(\eta) = \int I_i^{(4)}(\eta)d\eta$, $I_i^{(2)}(\eta) = \int I_i^{(3)}(\eta)d\eta$, $I_i^{(1)}(\eta) = \int I_i^{(2)}(\eta)d\eta$, $I_i^{(0)}(\eta) = \int I_i^{(1)}(\eta)d\eta$, and $\{C_1, C_2, C_3, C_4\}$ the constants of integration.

Evaluation of (4.3)-(4.7) at a set of collocation points $\{\eta_j\}_{j=1}^{N_\eta}$ leads to

$$\widehat{\frac{d^4\psi}{d\eta^4}} = \widehat{\mathcal{I}}_{[4]}^{(4)}\widehat{\alpha}_{[4]}, \tag{4.8}$$

$$\widehat{\frac{d^3\psi}{d\eta^3}} = \widehat{\mathcal{I}}_{[4]}^{(3)}\widehat{\alpha}_{[4]}, \tag{4.9}$$

$$\widehat{\frac{d^2\psi}{d\eta^2}} = \widehat{\mathcal{I}}_{[4]}^{(2)}\widehat{\alpha}_{[4]}, \tag{4.10}$$

$$\widehat{\frac{d\psi}{d\eta}} = \widehat{\mathcal{I}}_{[4]}^{(1)}\widehat{\alpha}_{[4]}, \tag{4.11}$$

$$\widehat{\psi} = \widehat{\mathcal{I}}_{[4]}^{(0)}\widehat{\alpha}_{[4]}, \tag{4.12}$$

where subscript [.] and superscript (.) are used to denote the order of IRBFN

scheme and the order of the corresponding derivative function, respectively;

$$\widehat{\mathcal{I}}^{(4)}_{[4]} = \begin{bmatrix} I^{(4)}_1(\eta_1), & I^{(4)}_2(\eta_1), & \cdots, & I^{(4)}_{N_\eta}(\eta_1), & 0, & 0, & 0, & 0 \\ I^{(4)}_1(\eta_2), & I^{(4)}_2(\eta_2), & \cdots, & I^{(4)}_{N_\eta}(\eta_2), & 0, & 0, & 0, & 0 \\ \vdots & \vdots & \ddots & \vdots & \vdots & \vdots & \vdots & \vdots \\ I^{(4)}_1(\eta_{N_\eta}), & I^{(4)}_2(\eta_{N_\eta}), & \cdots, & I^{(p)}_{N_\eta}(\eta_{N_\eta}), & 0, & 0, & 0, & 0 \end{bmatrix},$$

$$\widehat{\mathcal{I}}^{(3)}_{[4]} = \begin{bmatrix} I^{(3)}_1(\eta_1), & I^{(3)}_2(\eta_1), & \cdots, & I^{(3)}_{N_\eta}(\eta_1), & 1, & 0, & 0, & 0 \\ I^{(3)}_1(\eta_2), & I^{(3)}_2(\eta_2), & \cdots, & I^{(3)}_{N_\eta}(\eta_2), & 1, & 0, & 0, & 0 \\ \vdots & \vdots & \ddots & \vdots & \vdots & \vdots & \vdots & \vdots \\ I^{(3)}_1(\eta_{N_\eta}), & I^{(3)}_2(\eta_{N_\eta}), & \cdots, & I^{(3)}_{N_\eta}(\eta_{N_\eta}), & 1, & 0, & 0, & 0 \end{bmatrix},$$

$$\widehat{\mathcal{I}}^{(2)}_{[4]} = \begin{bmatrix} I^{(2)}_1(\eta_1), & I^{(2)}_2(\eta_1), & \cdots, & I^{(2)}_{N_\eta}(\eta_1), & \eta_1, & 1, & 0, & 0 \\ I^{(2)}_1(\eta_2), & I^{(2)}_2(\eta_2), & \cdots, & I^{(2)}_{N_\eta}(\eta_2), & \eta_2, & 1, & 0, & 0 \\ \vdots & \vdots & \ddots & \vdots & \vdots & \vdots & \vdots & \vdots \\ I^{(2)}_1(\eta_{N_\eta}), & I^{(2)}_2(\eta_{N_\eta}), & \cdots, & I^{(2)}_{N_\eta}(\eta_{N_\eta}), & \eta_{N_\eta}, & 1, & 0, & 0 \end{bmatrix},$$

$$\widehat{\mathcal{I}}^{(1)}_{[4]} = \begin{bmatrix} I^{(1)}_1(\eta_1), & I^{(1)}_2(\eta_1), & \cdots, & I^{(1)}_{N_\eta}(\eta_1), & \eta_1^2/2, & \eta_1, & 1, & 0 \\ I^{(1)}_1(\eta_2), & I^{(1)}_2(\eta_2), & \cdots, & I^{(1)}_{N_\eta}(\eta_2), & \eta_2^2/2, & \eta_2, & 1, & 0 \\ \vdots & \vdots & \ddots & \vdots & \vdots & \vdots & \vdots & \vdots \\ I^{(1)}_1(\eta_{N_\eta}), & I^{(1)}_2(\eta_{N_\eta}), & \cdots, & I^{(1)}_{N_\eta}(\eta_{N_\eta}), & \eta_{N_\eta}^2/2, & \eta_{N_\eta}, & 1, & 0 \end{bmatrix},$$

$$\widehat{\mathcal{I}}^{(0)}_{[4]} = \begin{bmatrix} I^{(0)}_1(\eta_1), & I^{(0)}_2(\eta_1), & \cdots, & I^{(0)}_N(\eta_1), & \eta_1^3/6, & \eta_1^2/2, & \eta_1, & 1 \\ I^{(0)}_1(\eta_2), & I^{(0)}_2(\eta_2), & \cdots, & I^{(0)}_N(\eta_2), & \eta_2^3/6, & \eta_2^2/2, & \eta_2, & 1 \\ \vdots & \vdots & \ddots & \vdots & \vdots & \vdots & \vdots & \vdots \\ I^{(0)}_1(\eta_{N_\eta}), & I^{(0)}_2(\eta_{N_\eta}), & \cdots, & I^{(0)}_N(\eta_{N_\eta}), & \eta_{N_\eta}^3/6, & \eta_{N_\eta}^2/2, & \eta_{N_\eta}, & 1 \end{bmatrix};$$

$$\widehat{\alpha}_{[4]} = \left(w_1, w_2, \cdots, w_{N_\eta}, C_1, C_2, C_3, C_4\right)^T;$$

and

$$\widehat{\frac{d^k\psi}{d\eta^k}} = \left(\frac{d^k\psi_1}{d\eta^k}, \frac{d^k\psi_2}{d\eta^k}, \cdots, \frac{d^k\psi_{N_\eta}}{d\eta^k}\right)^T, \quad k = \{1, 2, 3, 4\},$$

$$\widehat{\psi} = \left(\psi_1, \psi_2, \cdots, \psi_{N_\eta}\right)^T,$$

in which $d^k\psi_j/d\eta^k = d^k\psi(\eta_j)/d\eta^k$ and $\psi_j = \psi(\eta_j)$ with $j = \{1, 2, \cdots, N_\eta\}$.

Second-order 1D-IRBFNs

Making use of (2.52)-(2.55) with $p = 2$ and $f \equiv T$, the following approximate expressions are obtained

$$\frac{d^2T(\eta)}{d\eta^2} = \sum_{i=1}^{N_\eta} w_i g_i(\eta) = \sum_{i=1}^{N_\eta} w_i I_i^{(2)}(\eta), \tag{4.13}$$

$$\frac{dT(\eta)}{d\eta} = \sum_{i=1}^{N_\eta} w_i I_i^{(1)}(\eta) + C_1, \tag{4.14}$$

$$T(\eta) = \sum_{i=1}^{N_\eta} w_i I_i^{(0)}(\eta) + C_1\eta + C_2. \tag{4.15}$$

where N_η is the number of nodes on the grid line, $\{w_i\}_{i=1}^{N_\eta}$ the set of network weights, and $\{g_i(\eta)\}_{i=1}^{N_\eta} \equiv \left\{I_i^{(2)}(\eta)\right\}_{i=1}^{N_\eta}$ the set of RBFs, $I_i^{(1)}(\eta) = \int I_i^{(2)}(\eta)d\eta$, $I_i^{(0)}(\eta) = \int I_i^{(1)}(\eta)\,d\eta$, and C_1 and C_2 are the constants of integration.

Evaluation of (4.13) - (4.15) at the grid nodes leads to

$$\widehat{\frac{d^2T}{d\eta^2}} = \widehat{\mathcal{I}}_{[2]}^{(2)}\widehat{\alpha}_{[2]}, \tag{4.16}$$

$$\widehat{\frac{dT}{d\eta}} = \widehat{\mathcal{I}}_{[2]}^{(1)}\widehat{\alpha}_{[2]}, \tag{4.17}$$

$$\widehat{T} = \widehat{\mathcal{I}}_{[2]}^{(0)}\widehat{\alpha}_{[2]}, \tag{4.18}$$

where

$$
\begin{aligned}
\widehat{\mathcal{I}}_{[2]}^{(2)} &= \begin{bmatrix} I_1^{(2)}(\eta_1), & I_2^{(2)}(\eta_1), & \cdots, & I_{N_\eta}^{(2)}(\eta_1), & 0, & 0 \\ I_1^{(2)}(\eta_2), & I_2^{(2)}(\eta_2), & \cdots, & I_{N_\eta}^{(2)}(\eta_2), & 0, & 0 \\ \vdots & \vdots & \ddots & \vdots & \vdots & \vdots \\ I_1^{(2)}(\eta_{N_\eta}), & I_2^{(2)}(\eta_{N_\eta}), & \cdots, & I_{N_\eta}^{(2)}(\eta_{N_\eta}), & 0, & 0 \end{bmatrix}; \\
\widehat{\mathcal{I}}_{[2]}^{(1)} &= \begin{bmatrix} I_1^{(1)}(\eta_1), & I_2^{(1)}(\eta_1), & \cdots, & I_{N_\eta}^{(1)}(\eta_1), & 1, & 0 \\ I_1^{(1)}(\eta_2), & I_2^{(1)}(\eta_2), & \cdots, & I_{N_\eta}^{(1)}(\eta_2), & 1, & 0 \\ \vdots & \vdots & \ddots & \vdots & \vdots & \vdots \\ I_1^{(1)}(\eta_{N_\eta}), & I_2^{(1)}(\eta_{N_\eta}), & \cdots, & I_{N_\eta}^{(1)}(\eta_{N_\eta}), & 1, & 0 \end{bmatrix}; \\
\widehat{\mathcal{I}}_{[2]}^{(0)} &= \begin{bmatrix} I_1^{(0)}(\eta_1), & I_2^{(0)}(\eta_1), & \cdots, & I_{N_\eta}^{(0)}(\eta_1), & \eta_1, & 1 \\ I_1^{(0)}(\eta_2), & I_2^{(0)}(\eta_2), & \cdots, & I_{N_\eta}^{(0)}(\eta_2), & \eta_2, & 1 \\ \vdots & \vdots & \ddots & \vdots & \vdots & \vdots \\ I_1^{(0)}(\eta_{N_\eta}), & I_2^{(0)}(\eta_{N_\eta}), & \cdots, & I_{N_\eta}^{(0)}(\eta_{N_\eta}), & \eta_{N_\eta}, & 1 \end{bmatrix}; \\
\widehat{\alpha}_{[2]} &= \left(w_1, w_2, \cdots, w_{N_\eta}, C_1, C_2\right)^T;
\end{aligned}
$$

and

$$
\begin{aligned}
\widehat{\frac{d^2T}{d\eta^2}} &= \left(\frac{d^2T_1}{d\eta^2}, \frac{d^2T_2}{d\eta^2}, \cdots, \frac{d^2T_{N_\eta}}{d\eta^2}\right)^T; \\
\widehat{\frac{dT}{d\eta}} &= \left(\frac{dT_1}{d\eta}, \frac{dT_2}{d\eta}, \cdots, \frac{dT_{N_\eta}}{d\eta}\right)^T; \\
\widehat{T} &= \left(T_1, T_2, \cdots, T_{N_\eta}\right)^T,
\end{aligned}
$$

in which $d^2T_j/d\eta^2 = d^2T(\eta_j)/d\eta^2$, $dT_j/d\eta = dT(\eta_j)/d\eta$ and $T_j = T(\eta_j)$ with $j = \{1, 2, \cdots, N_\eta\}$.

4.3.2 Imposition of boundary conditions

Unlike conventional interpolation schemes, the present integral interpolation scheme produces some extra arbitrary constant values (i.e. the integration constants) which can be treated like the RBF weights. These additional coefficients can be utilised to include derivative boundary conditions in the 1D-IRBFN approximations. Details are as follows.

Double boundary conditions for the streamfunction

Double boundary conditions (ψ and $\partial\psi/\partial\eta$ given at η_1 and at η_{N_η}) are incorporated into the 1D-IRBFN approximations through the process of conversion of the network-weight space into the physical space

$$\begin{pmatrix} \widehat{\psi} \\ \widehat{e}_\psi \end{pmatrix} = \begin{bmatrix} \widehat{\mathcal{I}}^{(0)}_{[4]} \\ \widehat{\mathcal{K}}_{[4]} \end{bmatrix} \widehat{\alpha}_{[4]} = \widehat{\mathcal{C}}_{[4]} \widehat{\alpha}_{[4]}, \tag{4.19}$$

where $\widehat{e}_\psi = (\partial\psi_1/\partial\eta,\, \partial\psi_{N_\eta}/\partial\eta)^T$; $\widehat{\psi}$, $\widehat{\alpha}_{[4]}$ and $\widehat{\mathcal{I}}^{(0)}_{[4]}$ defined as before; $\widehat{\mathcal{C}}_{[4]}$ the conversion matrix; and $\widehat{\mathcal{K}}_{[4]}$ is the matrix made of the first and last rows of $\widehat{\mathcal{I}}^{(1)}_{[4]}$:

$$\widehat{\mathcal{K}}_{[4]} = \begin{bmatrix} I^{(1)}_1(\eta_1), & I^{(1)}_2(\eta_1), & \cdots, & I^{(1)}_{N_\eta}(\eta_1), & \eta_1^2/2, & \eta_1, & 1, & 0 \\ I^{(1)}_1(\eta_{N_\eta}), & I^{(1)}_2(\eta_{N_\eta}), & \cdots, & I^{(1)}_{N_\eta}(\eta_{N_\eta}), & \eta_{N_\eta}^2/2, & \eta_{N_\eta}, & 1, & 0 \end{bmatrix}.$$

It can be seen from (4.19) that, despite the presence of nodal derivative boundary conditions, the approximate solution ψ is still collocated at the whole set of centres and the obtained system is not over-determined. Solving (4.19) for $\widehat{\alpha}_{[4]}$ yields

$$\widehat{\alpha}_{[4]} = \widehat{\mathcal{C}}^{-1}_{[4]} \begin{pmatrix} \widehat{\psi} \\ \widehat{e}_\psi \end{pmatrix}, \tag{4.20}$$

where $\widehat{\mathcal{C}}_{[4]}^{-1}$ is the pseudo-inverse of $\widehat{\mathcal{C}}_{[4]}$. Substitution of (4.20) into (4.3)-(4.7) leads to

$$\psi(\eta) = \left(I_1^{(0)}(\eta), I_2^{(0)}(\eta), \cdots, I_{N_\eta}^{(0)}(\eta), \eta^3/6, \eta^2/2, \eta, 1\right) \widehat{\mathcal{C}}_{[4]}^{-1} \begin{pmatrix} \widehat{\psi} \\ \widehat{e}_\psi \end{pmatrix}, \tag{4.21}$$

$$\frac{\partial \psi(\eta)}{\partial \eta} = \left(I_1^{(1)}(\eta), I_2^{(1)}(\eta), \cdots, I_{N_\eta}^{(1)}(\eta), \eta^2/2, \eta, 1, 0\right) \widehat{\mathcal{C}}_{[4]}^{-1} \begin{pmatrix} \widehat{\psi} \\ \widehat{e}_\psi \end{pmatrix}, \tag{4.22}$$

$$\frac{\partial^2 \psi(\eta)}{\partial \eta^2} = \left(I_1^{(2)}(\eta), I_2^{(2)}(\eta), \cdots, I_{N_\eta}^{(2)}(\eta), \eta, 1, 0, 0\right) \widehat{\mathcal{C}}_{[4]}^{-1} \begin{pmatrix} \widehat{\psi} \\ \widehat{e}_\psi \end{pmatrix}, \tag{4.23}$$

$$\frac{\partial^3 \psi(\eta)}{\partial \eta^3} = \left(I_1^{(3)}(\eta), I_2^{(3)}(\eta), \cdots, I_{N_\eta}^{(3)}(\eta), 1, 0, 0, 0\right) \widehat{\mathcal{C}}_{[4]}^{-1} \begin{pmatrix} \widehat{\psi} \\ \widehat{e}_\psi \end{pmatrix}, \tag{4.24}$$

$$\frac{\partial^4 \psi(\eta)}{\partial \eta^4} = \left(I_1^{(4)}(\eta), I_2^{(4)}(\eta), \cdots, I_{N_\eta}^{(4)}(\eta), 0, 0, 0, 0\right) \widehat{\mathcal{C}}_{[4]}^{-1} \begin{pmatrix} \widehat{\psi} \\ \widehat{e}_\psi \end{pmatrix}, \tag{4.25}$$

or

$$\psi(\eta) = \sum_{i=1}^{N_\eta} \varphi_i^{[\eta]}(\eta)\psi_i + \varphi_{N_\eta+1}^{[\eta]}(\eta)\frac{\partial \psi_1}{\partial \eta} + \varphi_{N_\eta+2}^{[\eta]}(\eta)\frac{\partial \psi_{N_\eta}}{\partial \eta}, \tag{4.26}$$

$$\frac{\partial \psi(\eta)}{\partial \eta} = \sum_{i=1}^{N_\eta} \frac{\partial \varphi_i^{[\eta]}(\eta)}{\partial \eta}\psi_i + \frac{\partial \varphi_{N_\eta+1}^{[\eta]}(\eta)}{\partial \eta}\frac{\partial \psi_1}{\partial \eta} + \frac{\partial \varphi_{N_\eta+2}^{[\eta]}(\eta)}{\partial \eta}\frac{\partial \psi_{N_\eta}}{\partial \eta}, \tag{4.27}$$

$$\frac{\partial^2 \psi(\eta)}{\partial \eta^2} = \sum_{i=1}^{N_\eta} \frac{\partial^2 \varphi_i^{[\eta]}(\eta)}{\partial \eta^2}\psi_i + \frac{\partial^2 \varphi_{N_\eta+1}^{[\eta]}(\eta)}{\partial \eta^2}\frac{\partial \psi_1}{\partial \eta} + \frac{\partial^2 \varphi_{N_\eta+2}^{[\eta]}(\eta)}{\partial \eta^2}\frac{\partial \psi_{N_\eta}}{\partial \eta}, \tag{4.28}$$

$$\frac{\partial^3 \psi(\eta)}{\partial \eta^3} = \sum_{i=1}^{N_\eta} \frac{\partial^3 \varphi_i^{[\eta]}(\eta)}{\partial \eta^3}\psi_i + \frac{\partial^3 \varphi_{N_\eta+1}^{[\eta]}(\eta)}{\partial \eta^3}\frac{\partial \psi_1}{\partial \eta} + \frac{\partial^3 \varphi_{N_\eta+2}^{[\eta]}(\eta)}{\partial \eta^3}\frac{\partial \psi_{N_\eta}}{\partial \eta}, \tag{4.29}$$

$$\frac{\partial^4 \psi(\eta)}{\partial \eta^4} = \sum_{i=1}^{N_\eta} \frac{\partial^4 \varphi_i^{[\eta]}(\eta)}{\partial \eta^4}\psi_i + \frac{\partial^4 \varphi_{N_\eta+1}^{[\eta]}(\eta)}{\partial \eta^4}\frac{\partial \psi_1}{\partial \eta} + \frac{\partial^4 \varphi_{N_\eta+2}^{[\eta]}(\eta)}{\partial \eta^4}\frac{\partial \psi_{N_\eta}}{\partial \eta}, \tag{4.30}$$

where $\{\varphi_i^{[\eta]}\}_{i=1}^{N_\eta+2}$ is the set of 1D-IRBFN basis functions in the physical space for ψ.

Boundary conditions for the temperature

Case 1: Neuman-Neumann boundary conditions

Assume that boundary conditions for T at the two ends of the grid line are of Neumann type (i.e. $\partial T_1/\partial\eta$ and $\partial T_{N_\eta}/\partial\eta$). Those values are also incorporated into the 1D-IRBFN approximations through the process of conversion as in the case of double boundary conditions. Through such a mapping, the value of T and its derivatives at an arbitrary point η on the grid line can then be computed by

$$T(\eta) = \left(I_1^{(0)}(\eta), I_2^{(0)}(\eta), \cdots, I_{N_\eta}^{(0)}(\eta), \eta, 1\right) \widehat{\mathcal{C}}_{[2]}^{-1} \begin{pmatrix} \widehat{T} \\ \widehat{e}_T \end{pmatrix}, \tag{4.31}$$

$$\frac{\partial T(\eta)}{\partial\eta} = \left(I_1^{(1)}(\eta), I_2^{(1)}(\eta), \cdots, I_{N_\eta}^{(1)}(\eta), 1, 0\right) \widehat{\mathcal{C}}_{[2]}^{-1} \begin{pmatrix} \widehat{T} \\ \widehat{e}_T \end{pmatrix}, \tag{4.32}$$

$$\frac{\partial^2 T(\eta)}{\partial\eta^2} = \left(I_1^{(2)}(\eta), I_2^{(2)}(\eta), \cdots, I_{N_\eta}^{(2)}(\eta), 0, 0\right) \widehat{\mathcal{C}}_{[2]}^{-1} \begin{pmatrix} \widehat{T} \\ \widehat{e}_T \end{pmatrix}, \tag{4.33}$$

where

$$\widehat{e}_T = \begin{bmatrix} \frac{\partial T_1}{\partial\eta} \\ \frac{\partial T_{N_\eta}}{\partial\eta} \end{bmatrix},$$

$$\widehat{\mathcal{C}}_{[2]} = \begin{bmatrix} \widehat{\mathcal{I}}_{[2]}^{(0)} \\ \widehat{\mathcal{K}}_{[2]} \end{bmatrix},$$

in which $\widehat{\mathcal{I}}_{[2]}^{(0)}$ is defined as before, and

$$\widehat{\mathcal{K}}_{[2]} = \begin{bmatrix} I_1^{(1)}(\eta_1), & I_2^{(1)}(\eta_1), & \cdots, & I_{N_\eta}^{(1)}(\eta_1), & 1, & 0 \\ I_1^{(1)}(\eta_{N_\eta}), & I_2^{(1)}(\eta_{N_\eta}), & \cdots, & I_{N_\eta}^{(1)}(\eta_{N_\eta}), & 1, & 0 \end{bmatrix}.$$

Expressions (4.31)-(4.33) can be rewritten in the compact form

$$T(\eta) = \sum_{i=1}^{N_\eta} \vartheta_i^{[\eta]}(\eta) T_i + \vartheta_{N_\eta+1}^{[\eta]}(\eta) \frac{\partial T_1}{\partial \eta} + \vartheta_{N_\eta+2}^{[\eta]}(\eta) \frac{\partial T_{N_\eta}}{\partial \eta}, \tag{4.34}$$

$$\frac{\partial T(\eta)}{\partial \eta} = \sum_{i=1}^{N_\eta} \frac{\partial \vartheta_i^{[\eta]}(\eta)}{\partial \eta} T_i + \frac{\partial \vartheta_{N_\eta+1}^{[\eta]}(\eta)}{\partial \eta} \frac{\partial T_1}{\partial \eta} + \frac{\partial \vartheta_{N_\eta+2}^{[\eta]}(\eta)}{\partial \eta} \frac{\partial T_{N_\eta}}{\partial \eta}, \tag{4.35}$$

$$\frac{\partial^2 T(\eta)}{\partial \eta^2} = \sum_{i=1}^{N_\eta} \frac{\partial^2 \vartheta_i^{[\eta]}(\eta)}{\partial \eta^2} T_i + \frac{\partial^2 \vartheta_{N_\eta+1}^{[\eta]}(\eta)}{\partial \eta^2} \frac{\partial T_1}{\partial \eta} + \frac{\partial^2 \vartheta_{N_\eta+2}^{[\eta]}(\eta)}{\partial \eta^2} \frac{\partial T_{N_\eta}}{\partial \eta}, \tag{4.36}$$

where $\{\vartheta_i^{[\eta]}\}_{i=1}^{N_\eta+2}$ is the set of 1D-IRBFN basis functions in the physical space for T.

Case 2: Dirichlet-Dirichlet boundary conditions

Assume that boundary conditions for T at the two ends of the grid line are of Dirichlet type. Unlike Case 1, the extra information vector $\widehat{e}_T$ in the conversion process here is simply set to null. Expressions (4.34)-(4.36) thus reduce to

$$T(\eta) = \sum_{i=1}^{N_\eta} \vartheta_i^{[\eta]}(\eta) T_i, \tag{4.37}$$

$$\frac{\partial T(\eta)}{\partial \eta} = \sum_{i=1}^{N_\eta} \frac{\partial \vartheta_i^{[\eta]}(\eta)}{\partial \eta} T_i, \tag{4.38}$$

$$\frac{\partial^2 T(\eta)}{\partial \eta^2} = \sum_{i=1}^{N_\eta} \frac{\partial^2 \vartheta_i^{[\eta]}(\eta)}{\partial \eta^2} T_i. \tag{4.39}$$

4.3.3 Galerkin discretisations

Assume that (i) Dirichlet boundary conditions are prescribed on the two vertical lines and Neumann boundary conditions on the two horizontal lines for the energy equation (4.2); and (ii) double boundary conditions are prescribed on all boundary lines for the streamfunction equation (4.1).

We utilise 1D-IRBFN expressions (4.26)-(4.30) to construct the approximations for ψ on the x and y grid lines (i.e. $\eta \equiv x$ and $\eta \equiv y$), (4.34)-(4.36) for T on the y grid lines (i.e. $\eta \equiv y$), and (4.37)-(4.39) for T on the x grid lines (i.e. $\eta \equiv x$). One can then take products of those in each direction as basis functions for the interpolation of ψ and T over the whole domain Ω. The 1D-IRBFN approximations are thus defined everywhere in the domain through tensor products, which allows one to get the value of ψ and T at any point of the domain

$$\psi(x,y) = \sum_{i=1}^{N_x} \varphi_i^{[x]}(x) \left(\sum_{j=1}^{N_y} \varphi_j^{[y]}(y)\, \psi_{i,j} + \varphi_{N_y+1}^{[y]}(y) \frac{\partial \psi_{i,1}}{\partial y} + \varphi_{N_y+2}^{[y]}(y) \frac{\partial \psi_{i,N_y}}{\partial y} \right) + \sum_{j=1}^{N_y} \varphi_j^{[y]} \left(\varphi_{N_x+1}^{[x]}(x) \frac{\partial \psi_{1,j}}{\partial x} + \varphi_{N_x+2}^{[x]}(x) \frac{\partial \psi_{N_x,j}}{\partial x} \right), \tag{4.40}$$

$$T(x,y) = \sum_{i=1}^{N_x} \vartheta_i^{[x]}(x) \left(\sum_{j=1}^{N_y} \vartheta_j^{[y]}(y)\, T_{i,j} + \vartheta_{N_y+1}^{[y]}(y) \frac{\partial T_{i,1}}{\partial y} + \vartheta_{N_y+2}^{[y]}(y) \frac{\partial T_{i,N_y}}{\partial y} \right). \tag{4.41}$$

In (4.40) - (4.41), $\psi_{i,j}$, and $T_{i,j}$ are the values of the ψ and T variables at the intersection of the ith horizontal grid line and jth vertical grid line; the products $\varphi_i^{[x]}\varphi_j^{[y]}$ and the products $\vartheta_i^{[x]}\vartheta_j^{[y]}$ are usually referred to as the trial/basis/approximating functions; $\partial T_{i,1}/\partial y$ and $\partial T_{i,N_y}/\partial y$ are nodal derivative boundary conditions for T; and $\partial \psi_{i,1}/\partial y$, $\partial \psi_{i,N_y}/\partial y$, $\partial \psi_{1,j}/\partial x$ and $\partial \psi_{N_x,j}/\partial x$ are nodal derivative boundary conditions for ψ.

Discretisation of the streamfunction equation

Since expressions (4.40)-(4.41) over Ω are constructed to satisfy all boundary conditions, only the residual term for the governing equation in the integral weighted residual statement needs be considered. The Galerkin weighting pro-

cess applied to (4.1) over Ω produces the results

$$\int_\Omega W\left(\frac{\partial^4\psi}{\partial x^4}+2\frac{\partial^4\psi}{\partial x^2\partial y^2}+\frac{\partial^4\psi}{\partial y^4}\right)d\Omega-\sqrt{\frac{Ra}{Pr}}\int_\Omega W\left(\frac{\partial\psi}{\partial y}\left(\frac{\partial^3\psi}{\partial x^3}+\frac{\partial^3\psi}{\partial x\partial y^2}\right)-\frac{\partial\psi}{\partial x}\left(\frac{\partial^3\psi}{\partial x^2\partial y}+\frac{\partial^3\psi}{\partial y^3}\right)+\frac{\partial T}{\partial x}\right)d\Omega=0, \tag{4.42}$$

where W is the weighting/test functions which are taken from the set of trial functions (i.e. $W=\varphi_i^{[x]}\varphi_j^{[y]}$, $2\leq i\leq(N_x-1)$ and $2\leq j\leq(N_y-1)$). The above volume integrals can be evaluated using repeated integrals, for which Gauss quadratures are employed along the grid lines. The determinate system of equations, (4.42), can then be used to solve for the nodal value of the variable ψ.

Discretisation of of the energy equation

In the same manner, the Galerkin weighting process applied to (4.2) over domain Ω produces the results

$$\int_\Omega W\left(\frac{\partial^2T}{\partial x^2}+\frac{\partial^2T}{\partial y^2}\right)d\Omega-\sqrt{RaPr}\int_\Omega W\left(\frac{\partial\psi}{\partial y}\frac{\partial T}{\partial x}-\frac{\partial\psi}{\partial x}\frac{\partial T}{\partial y}\right)d\Omega=0, \tag{4.43}$$

where $W=\vartheta_i^{[x]}\vartheta_j^{[y]}$, $2\leq i\leq(N_x-1)$ and $1\leq j\leq N_y$.

4.4 Numerical results

1D-IRBFNs are implemented with the multiquadric (MQ) function $g_i(\eta)=\sqrt{(\eta-\eta_i)^2+a_i^2}$ in which η_i and a_i are the centre and width of the ith MQ, respectively. The MQ centres are distributed uniformly, from which the trial and test spaces are generated. The MQ width is simply taken to be the grid size h. Furthermore, the collocation points are the centres themselves. We

employ the discrete relative L_2 norm of the error, denoted by N_e, to measure the accuracy of a numerical scheme. Some properties of 1D-IRBFNs of fourth and second order are first studied through the interpolation of a function (the first two problems), and they are then utilised in the solution of the biharmonic equation (third problem) and the streamfunction-temperature formulation (last problem).

4.4.1 Problem 1: Equidistant interpolating points (Runge's phenomenon)

When using algebraic polynomials to represent certain functions that are sampled at equally-spaced points, the error between the function and the interpolating polynomial can grow quickly as the number of sample points increases, which is called Runge's phenomenon. Figure 4.1a illustrates this phenomenon for the interpolation of a function $f(x) = 1/(1 + 25x^2)$ with $-1 \leq x \leq 1$. The oscillation between the interpolating points, especially in the region close to the boundaries, is significantly magnified when changing from 6 to 11 points. To minimise/eliminate the oscillation, it is necessary to employ Chebyshev nodes that cluster at the boundaries of the domain or to use piecewise low-order polynomials. For the latter, the quality of the interpolation is improved by increasing the number of polynomial pieces.

It is interesting to see the behaviour of 1D-IRBFNs when they are applied to interpolate the above function. As shown in Figure 4.1b, there is no oscillation between the interpolating points for the IRBFN scheme. Indeed, the interpolation error is reduced with increasing the number of equidistant points. 1D-IRBFNs can thus work well with the equidistant points.

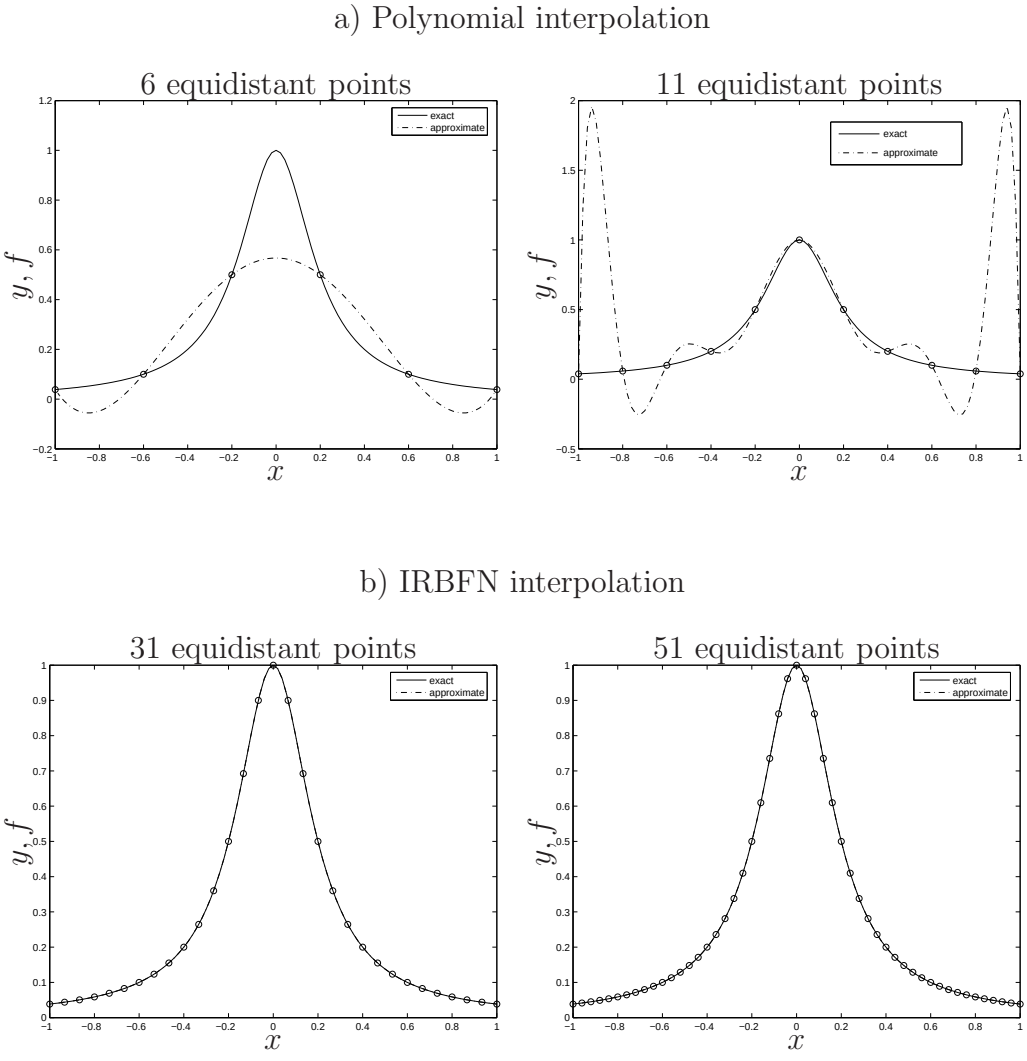

Figure 4.1: Problem 1, function interpolation, $f(x) = 1/(1 + 25x^2)$, $-1 \leq x \leq 1$: Performances of polynomial and IRBFN interpolants using equally-spaced interpolating points denoted by $\circ$. The latter does not suffer from Runge's phenomenon. It is noted that the approximate function is plotted using 501 uniformly-distributed points.

4.4.2 Problem 2: Extra information

When interpolating a function, in some cases, one is also given some extra information apart from nodal function values. Extra information can be derivative function values at some interpolating points. It will be shown that the 1D-IRBFN scheme can handle such cases very well.

Consider a function $f(x) = \sin(2\pi x)$ with $0 \leq x \leq 1$. The domain is represented by a set of uniformly-distributed points. At the two endpoints, first derivative values are also given. To provide a useful basis for comparison, conventional RBFNs (DRBFNs) are also employed. There are two basic cases to be studied here.

Case 1: the data input consists of function values only (Legend "function values only" in Figure 4.2). We use DRBFN and IRBFNs (IRBFN interpolation for second-order PDEs). In both of cases, the approximate function is collocated at all centres.

Case 2: the data input consists of function values at the set of points and derivative values at the two boundary points (Legend "function and derivative values" in Figure 4.2). For DRBFNs, the function is not collocated at the two centres adjacent to the boundaries in favor of the imposition of two derivative values. For IRBFN, the presence of two integration constants allows the addition of two extra equations to represent the two derivative values.

The results are given in Figure 4.2. When changing from the first to second case, the accuracy is reduced for DRBFNs (Figure 4.2a), but enhanced for IRBFNs (Figure 4.2b). This capability of IRBFNs will be utilised to implement double boundary conditions in solving biharmonic problems.

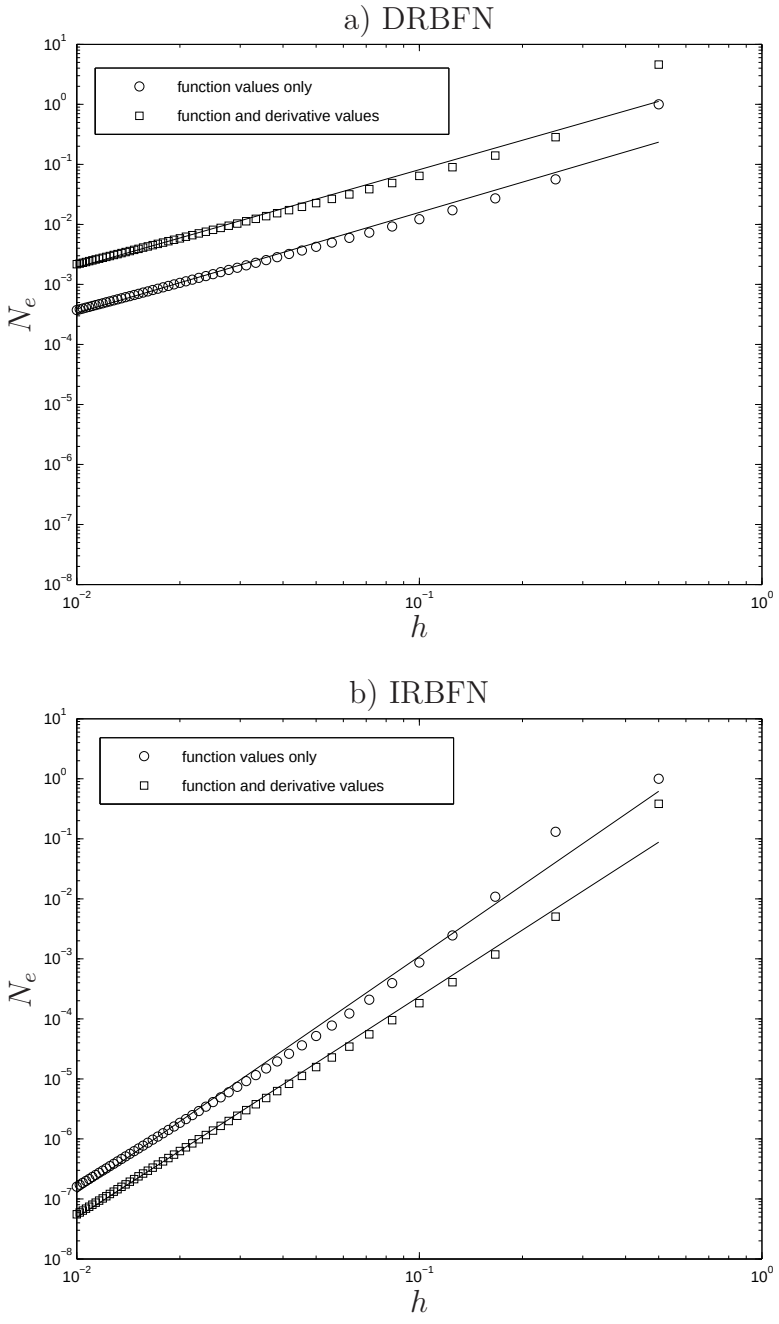

Figure 4.2: Problem 2, function interpolation, $f(x) = \sin(2\pi x)$, $0 \leq x \leq 1$: Error versus the grid spacing. The domain is discretised using uniform grids made of 3 to 101 points with increment of 2. Errors are computed at a test grid of 501 uniformly-distributed points. The DRBFN's N_e is $O(h^{1.67})$ and $O(h^{1.62})$ for case 1 and 2, respectively. The corresponding IRBFN's N_e is $O(h^{3.93})$ and $O(h^{3.67})$. It is noted that the above figures have the same scaling.

4.4.3 Problem 3: Linear test problem

The proposed 1D-IRBFN-based Galerkin technique is first verified through a linear biharmonic problem, of which the exact solution is available. In this example, we consider the following equation

$$\frac{\partial^4\psi}{\partial x^4} + 2\frac{\partial^4\psi}{\partial x^2\partial y^2} + \frac{\partial^4\psi}{\partial y^4} = \frac{4\pi^4}{1+2\pi^2}\cos(\pi x)\cos(\pi y - \pi/2), \tag{4.44}$$

which is defined on a square $-1 \leq x, y \leq 1$ and the boundary conditions are of Dirichlet type (i.e. ψ and $\partial\psi/\partial n$). The exact solution can be verified to be

$$\widetilde{\psi}(x,y) = \frac{1}{1+2\pi^2}\cos(\pi x)\cos(\pi y - \pi/2), \tag{4.45}$$

whose variation is shown in Figure 4.3. It can be seen that the boundary data are nonhomogeneous. An attractive feature of the present technique is that it can work directly with the prescribed boundary conditions of complicated shapes.

The trial and test spaces are generated from a set of N centres ($N = N_x N_y$). To study the convergence behaviour of the proposed method, we employ a number of uniform grids for the MQ centres. Results concerning N_e are given in Table 4.1. It can be seen that a very fast rate of convergence (indicated by N_e of $O(h^{6.07})$) is achieved. At $N = 961$ that corresponds to a density of 31×31, the approximate solution is accurate up to at least 8 significant digits.

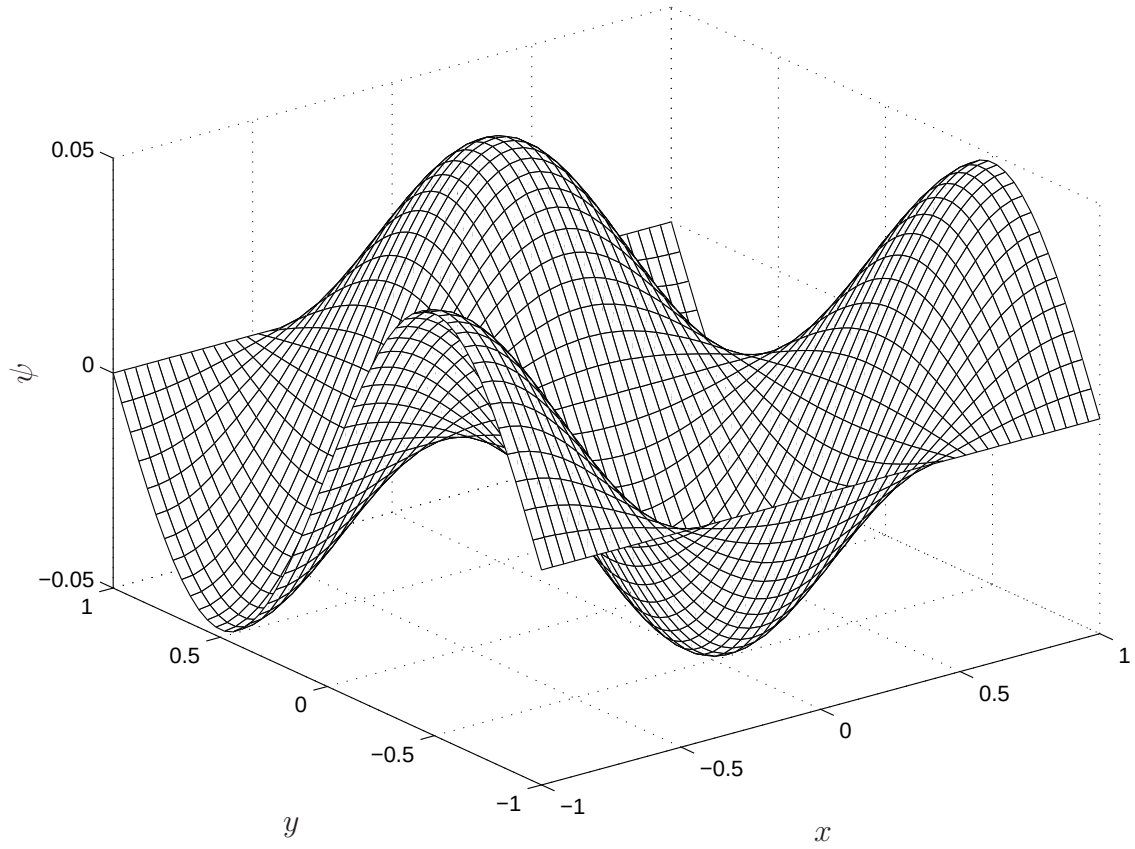

Figure 4.3: Problem 3: Exact solution.

Table 4.1: Problem 3, linear problem: Error $N_e(\psi)$ versus the number of RBFs N.

N	$N_e(\psi)$
9	1.52e+1
25	8.34e-2
49	2.89e-3
81	3.77e-4
121	9.82e-5
169	3.70e-5
225	1.73e-5
289	9.37e-6
361	5.56e-6
441	3.53e-6
529	2.36e-6
625	1.64e-6
729	1.17e-6
841	8.67e-7
961	6.47e-7
	$O(h^{6.07})$

4.4.4 Problem 4: Nonlinear buoyancy-driven flow

The proposed method is further validated with a nonlinear test, namely a buoyancy-driven flow problem. This problem is governed by (4.1) and (4.2). The domain of interest is an enclosed square cavity with insulated top and bottom walls and heated vertical walls:

- $\psi = 0$ and $\partial\psi/\partial n = 0$ ($u = 0$ and $v = 0$) on the boundaries Γ of Ω
- $T = 0.5$ on $x = 0$ and $T = -0.5$ on $x = 1$
- $\partial T/\partial y = 0$ on $y = 0$ and $y = 1$

This problem with the fluid being gas ($Pr = 0.71$) is widely used as a model for testing new numerical schemes in CFD. The level of complexity in structure of the flow field is considerably increased when $Ra > 10^6$. Benchmark solutions can be found in (Davis, 1983) for $Ra \leq 10^6$ and in (Quéré, 1991) for $Ra \geq 10^6$. The former used finite-difference approximations and a Richardson extrapolation scheme, while the latter employed pseudo-spectral approximations with Chebyshev polynomials.

Because of the strong coupling between the flow and heat transfer, the momentum equation (fourth-order differential equation for ψ) and the energy equation (second-order differential equation for T) must be solved simultaneously. Details of 1D-IRBFN-based Galerkin discretisations of momentum equation and energy equation are presented in Section 4.3. We apply a Picard scheme to handle the nonlinearity of this heated cavity problem. The solution procedure involves the following main steps

1. Solve (4.42) for ψ using the latest available temperature and stream function fields.

   Relax the stream function field

2. Solve (4.43) for T using the stream function field from Step 1 and the temperature field from the previous iteration.
   Relax the temperature field

3. Check for convergence. If not converged, return to step 1. If converged, stop

This computational procedure is economical owing to: (i) the matrices to be handled are of minimal size because the temperature and stream function problems are solved as separate systems; and (ii) the system matrices remain unchanged with iteration and Ra.

A wide range of Ra, namely $(10^3, 10^4, 10^5, 10^6, 10^7)$, is considered. All calculations are carried out using a relaxation factor of 0.001. It is noted that using larger values of the relaxation factor is possible. The nearest lower Ra solution is used as an initial guess.

Convergence behaviour: Four uniform grids of centres, $(21\times21, 31\times31, 41\times41, 51\times51)$, are employed. Convergence for the temperature and stream function fields for $Ra = 10^7$ are given in Figures 4.4 and 4.5, respectively. It is noted that the fields obtained with 51×51 have structures that are similar to those by the benchmark spectral results. It can be seen that all fields (i.e. ψ and T) converge very fast with the MQ centre's density refinement. Figure 4.6 concerning velocity profiles on the horizontal and vertical centrelines indicates that velocity boundary layers significantly increase in strength when Ra increases.

Solution accuracy: Some important measures associated with this type of flow are

- Maximum horizontal velocity u_{x-max} on the vertical mid-plane and its location;

- Maximum vertical velocity u_{y-max} on the horizontal mid-plane and its location;

- The average Nusselt number throughout the cavity, which is defined as

$$\overline{Nu} = \int_0^1 Nu(x)dx, \tag{4.46}$$

where

$$Nu(x) = \int_0^1 (u_x T - \frac{\partial T}{\partial x})dy. \tag{4.47}$$

In (4.46) and (4.47), integrals are computed using Simpson rule. The results at 51×51 for various Ra values are given in Table 4.2. It can be seen they are in very good agreement with the benchmark solutions.

Table 4.2: Problem 4: Natural convection flow, 51×51.

	Ra	u_{y-max}	Error(%)	x	u_{x-max}	Error(%)	y	$\overline{Nu}$	Error(%)
Present	10^3	3.6978	0.02	0.1783	3.6499	0.02	0.8132	1.1176	0.03
Benchmark	10^3	3.697		0.178	3.649		0.813	1.118	
(Davis, 1983)									
Present	10^4	19.6373	0.10	0.1189	16.1944	0.10	0.8233	2.2441	0.04
Benchmark	10^4	19.617		0.119	16.178		0.823	2.243	
(Davis, 1983)									
Present	10^5	68.6867	0.14	0.0659	34.8203	0.26	0.8547	4.5188	0.00
Benchmark	10^5	68.59		0.066	34.73		0.855	4.519	
(Davis, 1983)									
Present	10^6	220.8393	0.10	0.0378	65.1827	0.54	0.8504	8.8116	0.15
Benchmark	10^6	220.6		0.038	64.83		0.850	8.825	
(Quéré, 1991)									
Present	10^7	693.3044	0.84	0.0213	149.4011	0.53	0.8772	16.3468	1.06
Benchmark	10^7	699.2		0.021	148.6		0.879	16.523	
(Quéré, 1991)									

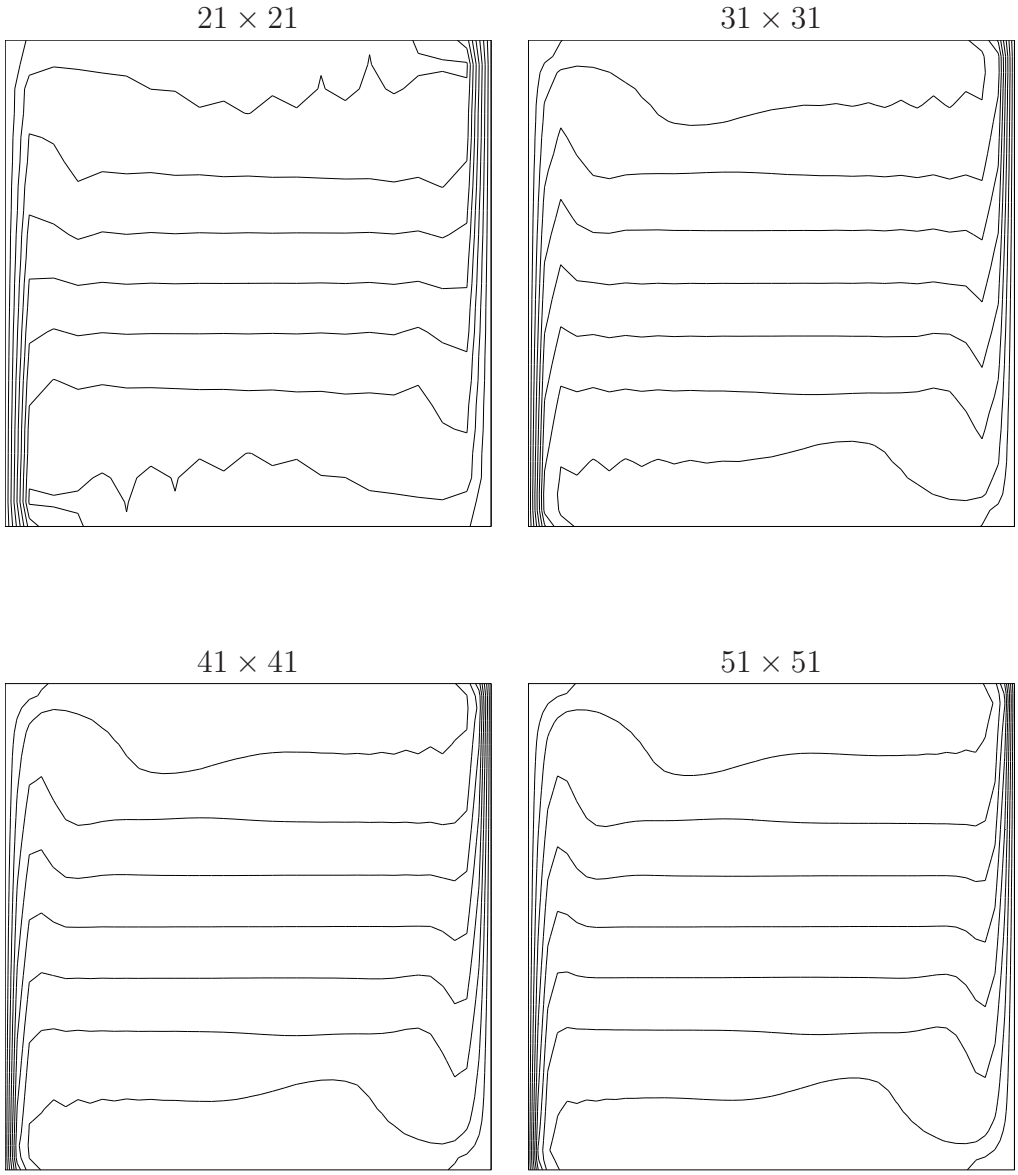

Figure 4.4: Problem 4, natural convection flow, $Ra = 10^7$: Convergence for the temperature field with respect to the MQ centre's density refinement. Iso-values used are $(-0.5 : 0.1 : 0.5)$ which are the same as those in (Quéré, 1991). The plot at 51×51 has a similar structure to that of the benchmark spectral result (Quéré, 1991).

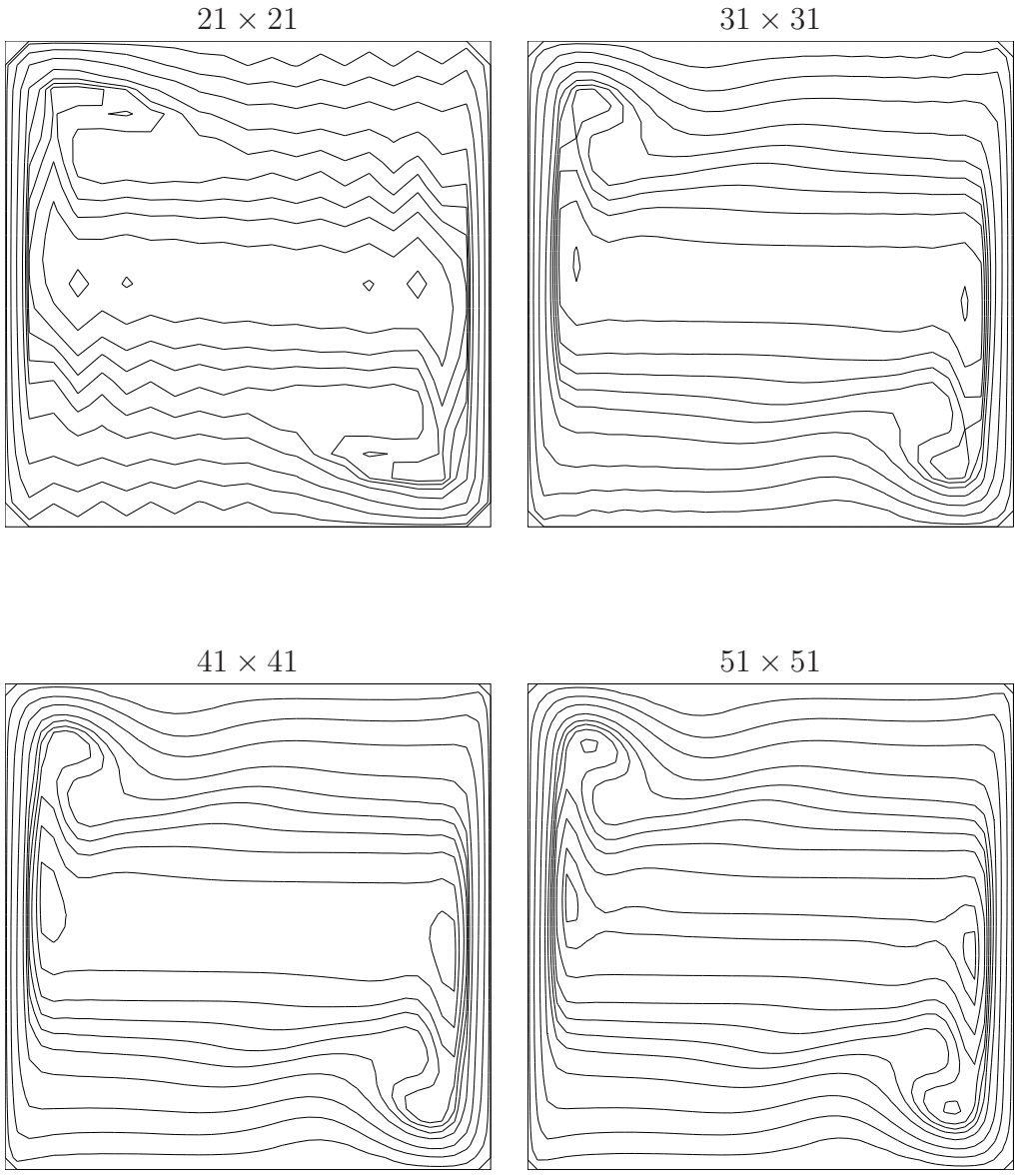

Figure 4.5: Problem 4, natural convection flow, $Ra = 10^7$: Convergence for the stream function field with respect to the MQ centre's density refinement. Isovalues used are $-1/\sqrt{Pr}$(0, 0.0005, 0.002, 0.004, 0.006, 0.007, 0.0075, 0.0079, 0.0083, 0.0088, 0.0092, 0.0094) which are the same as those in (Quéré, 1991). The plot at 51×51 has a similar structure to that of the benchmark spectral result (Quéré, 1991).

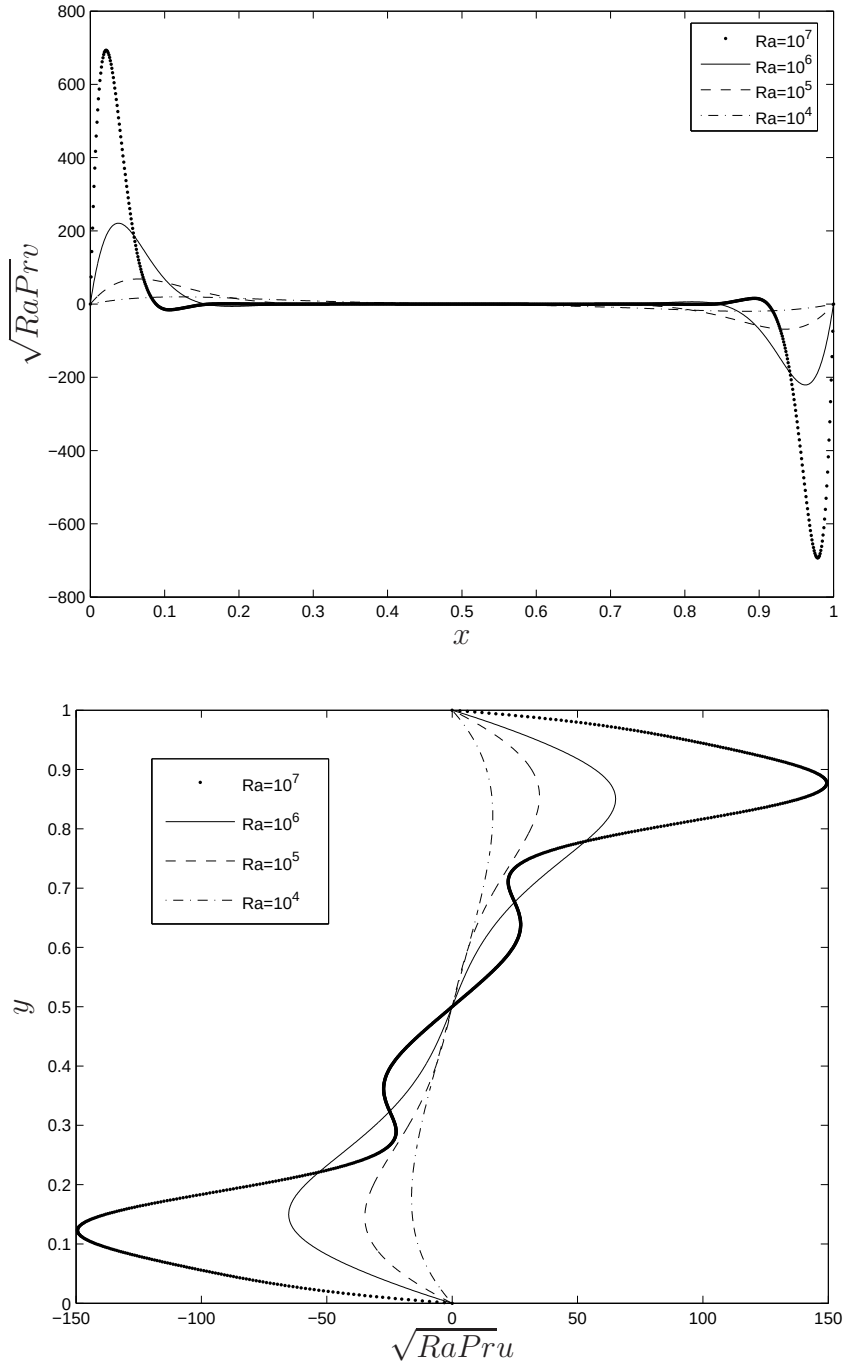

Figure 4.6: Problem 4, natural convection flow, 51×51: Velocity profiles on the horizontal and vertical centrelines for various Ra values.

4.5 Concluding Remarks

This chapter presents a 1D-IRBFN discretisation of Galerkin approximations for 2D viscous flows governed by the streamfunction-temperature formulation. The present approximate solution satisfies all boundary conditions (i.e. function and derivative values) in an exact manner. The Galerkin equation is considered for all weighting functions that are associated with the unknown nodal values. Moreover, for the biharmonic equation, homogeneous and non-homogeneous boundary conditions are implemented in a similar fashion. Unlike Galerkin spectral methods, the proposed method can work with uniform grids. Unlike Galerkin finite-element methods, all derivatives of the field variable are continuous over the problem domain. Numerical results show that the 1D-IRBFN-based Galerkin method achieves a high rate of convergence with increasing number of RBFs. For a benchmark thermally-driven flow in a square slot, accurate highly non-linear solutions are obtained using relatively-low data densities.

Chapter 5

1D-IRBFN-based Galerkin/Collocation methods for the streamfunction-vorticity formulation governing viscoelastic flows

In this chapter, integrated radial-basis-function networks in one dimension (1D-IRBFNs) are introduced into the Galerkin and point-collocation formulations to simulate viscoelastic flows. The computational domain is represented by a Cartesian grid and IRBFNs, which are constructed through integration, are employed on each grid line (i.e. 1D-IRBFNs) to approximate the field variables including stresses in the streamfunction-vorticity formulation. Two types of fluid, namely Oldroyd-B and CEF models, are considered. The proposed methods are validated through the numerical simulation of several benchmark test problems including flows in a rectangular duct and in a corrugated tube. Numerical results show that accurate results are obtained using relatively-coarse grids.

5.1 Introduction

Numerical simulation of viscoelastic flows still faces a lot of challenges. Main difficulties, which numerical methods have to deal with, are (i) complex material properties of fluids; (ii) mixed characters (elliptic for momentum equations and hyperbolic for constitutive equations); and (iii) high degrees of freedom (DOFs) (2D problems: 6 DOFs/node and 3D problems: 10 DOFs/node). In the case of large deformations, free/moving surfaces and complex geometries, further numerical difficulties will be added. One can classify discretisation methods into two categories: low order and high order. The former, e.g. traditional finite difference (FDMs), finite element (FEMs), finite volume (FVMs) and boundary element (BEMs) methods (possibly block-banded BEM), leads to a system matrix that is generally sparse and banded, while the latter, e.g. spectral and RBFN methods, can offer a significant saving on the computational cost owing to their high-order rates of convergence. Further details can be found in (Crochet and Walters, 1983; Crochet et al., 1984; Crochet, 1989; Tanner and Xue, 2002; Owens and Phillips, 2002).

The use of RBFNs for solving ordinary (ODEs) and partial (PDEs) differential equations including those governing fluid mechanics problems has been an active research area. RBFNs can be constructed through differentiation (the differential approach/DRBFNs) and through integration (the integral approach/IRBFNs). Pioneering numerical investigations (e.g. Mai-Duy and Tran-Cong, 2001a, 2003) and subsequent theoretical studies (Sarra, 2006) showed that IRBFN-based collocation methods yield better accuracy than DRBFN ones for the representation of functions and the solution of PDEs. In the early stages, the differential and integral approaches used every RBF to construct the approximations for the field variable at a nodal point, leading to a fully-populated system matrix. It was found that the matrix condition number grows rapidly with respect to the increase in the RBF width and/or the number of RBFs (Schaback, 1995). There were some reports on global RBF simulations of steady

viscoelastic flows (e.g. Tran-Cong, Mai-Duy and Phan-Thien, 2002; Tran-Canh and Tran-Cong, 2002; Mai-Duy and Tanner, 2006). Later on, local RBF techniques, where the approximations are constructed using only a few nodal points, have been developed (e.g. Atluri et al., 2003; Kosec and Šarler, 2008; Divo and Kassab, 2007; Mai-Duy and Tran-Cong, 2009a). The construction processes are thus conducted for a series of small matrices rather than for a large single matrix. In the context of IRBFNs, collocation schemes, based on 1D-IRBFNs and Cartesian grids, for the solution of 2D elliptic PDEs were reported in (e.g. Mai-Duy and Tran-Cong, 2007). The use of 1D-IRBFNs, where only nodal points on some relevant grid lines rather than on the whole grid are activated, requires much less memory and computational time than 2D-IRBFN schemes do. Therefore, the 1D-IRBFN approach achieves some degree of local approximation.

1D-IRBFNs were successfully introduced into the point-collocation and Galerkin formulations for the simulation of heat transfer and Newtonian-fluid flows (e.g. Mai-Duy and Tran-Cong, 2007; Mai-Duy et al., 2009; Ho-Minh et al., 2009). It was shown that those methods are stable, accurate and converge well. The 1D-IRBFN-based Galerkin method can obtain similar levels of accuracy for both types of boundary condition, i.e. Dirichlet only and Dirichlet-Neumann. In addition, its resultant system of algebraic equations is often symmetric and has a relatively-low condition number, which facilitates the employment of a much larger number of nodes.

In this chapter, we develop two methods (point collocation and Galerkin), which are based on 1D-IRBFNs and Cartesian grids, for the simulation of flows of viscoelastic fluids. The governing equations are taken in the streamfunction-vorticity formulation. A computational boundary condition for the vorticity is globally derived with the help of the constants of integration. Three benchmark test problems are considered to validate the proposed methods. In the first problem, fully-developed flows of a CEF fluid in a rectangular duct are

simulated. This problem is widely used to study secondary flows in a straight tube of non-circular cross-section. It is noted that CEF (Criminale et al., 1957) is seen as an attractive constitutive model in the numerical modelling of polymer flow systems owing to its low computational cost. The second problem is concerned with the simulation of Poiseuille flows in a straight tube of circular cross-section, where analytic solutions are available. The third problem is about the motion of an Oldroyd-B fluid in a corrugated tube - a standard test problem for numerical methods in non-Newtonian Fluid Mechanics (Burdette et al., 1989). In addition, this problem is also regarded as one of effective models in the study of viscoelastic flows in porous media. The obtained 1D-IRBFN results agree well with those produced by other techniques available in the literature.

The remainder of this chapter is organised as follows. In Section 5.2, a brief review of the governing equations for the motion of CEF and Oldroyd-B fluids is given. Section 5.3 presents the proposed 1D-IRBFN-based Galerkin/collocation methods. Three test problems are solved in Section 5.4. Section 5.5 concludes the chapter.

5.2 Governing equations

In this chapter, the working fluids are of the CEF and Oldroyd-B types. According to (1.3), the total stress tensors can be decomposed into two components, namely the pressure and the extra stress tensor.

For the CEF model, the extra stress tensor is defined as

$$\boldsymbol{\tau} = 2\mu\left(d\right)\boldsymbol{d} - \Phi_1 \overset{\nabla}{\boldsymbol{d}} + 4\Phi_2 \boldsymbol{d}\cdot\boldsymbol{d}, \tag{5.1}$$

where $\boldsymbol{d} = 1/2(\nabla\boldsymbol{u} + (\nabla\boldsymbol{u})^T)$ is the rate of deformation tensor, $d = \sqrt{2tr\left(\boldsymbol{d}\cdot\boldsymbol{d}\right)}$ the scalar magnitude of $\boldsymbol{d}$ (tr the trace operation), $\mu\left(d\right) = k|d|^{n-1}$ the viscosity (k the consistency factor and n the power law index), Φ_1 and Φ_2 the first and

the second normal stress coefficients, respectively, and $\overset{\nabla}{[\,]}$ the upper-convected derivative given by

$$\overset{\nabla}{[\,]} = \frac{\partial[\,]}{\partial t} + \boldsymbol{u}\cdot\nabla[\,] - (\nabla\boldsymbol{u})^T\cdot[\,] - [\,]\cdot\nabla\boldsymbol{u}. \tag{5.2}$$

For the Oldroyld-B model, the extra stress tensor is computed as

$$\begin{aligned} \boldsymbol{\tau} &= 2\mu_n\boldsymbol{d} + \boldsymbol{\tau_v}, & (5.3)\\ \boldsymbol{\tau_v} + \lambda\overset{\nabla}{\boldsymbol{\tau_v}} &= 2\mu_p\boldsymbol{d}, & (5.4) \end{aligned}$$

where μ_n is the "Newtonian-contribution" viscosity, μ_p the "polymer-contribution" viscosity, $\boldsymbol{\tau_v}$ the extra stress tensor due to viscoelasticity, and λ the relaxation time of the fluid. The Oldroyd-B model reduces to the UCM model when μ_n is set to zero and to the Newtonian model when $\lambda = 0$.

In this chapter, we consider the steady state of flows only and adopt the streamfunction-vorticity formulation. The equations for the conservation of momentum and mass of an incompressible fluid, (1.1) and (1.2), thus reduce to

$$\begin{aligned} \nabla^2\psi + \omega &= 0, & (5.5)\\ \nabla^2\omega &= F(\boldsymbol{u}\cdot\nabla\omega, \boldsymbol{\tau}, \mathbf{f}), & (5.6) \end{aligned}$$

where ψ is the streamfunction, ω the vorticity, and the RHS of (5.6) the function of $\boldsymbol{u}$, ω, $\boldsymbol{\tau}$ and $\mathbf{f}$. Numerical examples to be presented are solved in two coordinate systems, namely Cartesian and cylindrical.

The velocity components are related to the streamfunction via

$$u_x = \frac{\partial \psi}{\partial y}, \quad u_y = -\frac{\partial \psi}{\partial x} \quad \text{(Cartesian coordinates)}, \tag{5.7}$$

$$u_r = -\frac{1}{r}\frac{\partial \psi}{\partial z}, \quad u_z = \frac{1}{r}\frac{\partial \psi}{\partial r} \quad \text{(cylindrical coordinates)}. \tag{5.8}$$

For the CEF model, simulations are to be carried out using Cartesian coordinates and equation (5.1) is taken in the form

$$T_{xx} = 2\mu d_{xx} - \Phi_1 \left(u_x \frac{\partial d_{xx}}{\partial x} + u_y \frac{\partial d_{xx}}{\partial y} + \frac{\partial u_x}{\partial x} d_{xx} + \frac{\partial u_y}{\partial x} d_{xy} + \frac{\partial u_z}{\partial x} d_{xz} + d_{xx} \frac{\partial u_x}{\partial x} + d_{xy} \frac{\partial u_y}{\partial x} + d_{xz} \frac{\partial u_z}{\partial x} \right) + (\Phi_1 + 4\Phi_2) \left(d_{xx}^2 + d_{xy}^2 + d_{xz}^2 \right), \tag{5.9}$$

$$T_{xy} = 2\mu d_{xy} - \Phi_1 \left(u_x \frac{\partial d_{xy}}{\partial x} + u_y \frac{\partial d_{xy}}{\partial y} + \frac{\partial u_x}{\partial x} d_{xy} + \frac{\partial u_y}{\partial x} d_{yy} + \frac{\partial u_z}{\partial x} d_{yz} + d_{xx} \frac{\partial u_x}{\partial y} + d_{xy} \frac{\partial u_y}{\partial y} + d_{xz} \frac{\partial u_z}{\partial y} \right) + (\Phi_1 + 4\Phi_2) \left(d_{xx} d_{xy} + d_{xy} d_{yy} + d_{xz} d_{yz} \right), \tag{5.10}$$

$$T_{xz} = 2\mu d_{xz} - \Phi_1 \left(u_x \frac{\partial d_{xz}}{\partial x} + u_y \frac{\partial d_{xz}}{\partial y} + \frac{\partial u_x}{\partial x} d_{xz} + \frac{\partial u_y}{\partial x} d_{yz} + \frac{\partial u_z}{\partial x} d_{zz} + d_{xx} \frac{\partial u_x}{\partial z} + d_{xy} \frac{\partial u_y}{\partial z} + d_{xz} \frac{\partial u_z}{\partial z} \right) + (\Phi_1 + 4\Phi_2) \left(d_{xx} d_{xz} + d_{xy} d_{yz} + d_{xz} d_{zz} \right), \tag{5.11}$$

$$T_{yy} = 2\mu d_{yy} - \Phi_1 \left(u_x \frac{\partial d_{yz}}{\partial x} + u_y \frac{\partial d_{yz}}{\partial y} + \frac{\partial u_x}{\partial y} d_{yx} + \frac{\partial u_y}{\partial y} d_{yy} + \frac{\partial u_z}{\partial y} d_{yz} + d_{xy} \frac{\partial u_x}{\partial y} + d_{yy} \frac{\partial u_y}{\partial y} + d_{yz} \frac{\partial u_z}{\partial y} \right) + (\Phi_1 + 4\Phi_2) \left(d_{yx}^2 + d_{yy}^2 + d_{yz}^2 \right), \tag{5.12}$$

$$T_{yz} = 2\mu d_{yz} - \Phi_1 \left(u_x \frac{\partial d_{yz}}{\partial x} + u_y \frac{\partial d_{yz}}{\partial y} + \frac{\partial u_x}{\partial y} d_{xz} + \frac{\partial u_y}{\partial y} d_{yz} + \frac{\partial u_z}{\partial y} d_{zz} + d_{xy} \frac{\partial u_x}{\partial y} + d_{yy} \frac{\partial u_y}{\partial y} + d_{yz} \frac{\partial u_z}{\partial y} \right) + (\Phi_1 + 4\Phi_2) \left(d_{yx} d_{xz} + d_{yy} d_{yz} + d_{yz} d_{zz} \right), \tag{5.13}$$

where $T_{xx},\ T_{xy},\ T_{xz},\ T_{yy},\ T_{yz}$ are components of the extra stress $\boldsymbol{\tau}$;

$$\mu = k\left(2\left(\left(\frac{\partial u_x}{\partial x}\right)^2 + \left(\frac{\partial u_y}{\partial y}\right)^2\right) + \left(\frac{\partial u_x}{\partial y} + \frac{\partial u_y}{\partial x}\right)^2 + \left(\frac{\partial u_z}{\partial x}\right)^2 + \left(\frac{\partial u_z}{\partial y}\right)^2\right)^{\left(\frac{n-1}{2}\right)}; \tag{5.14}$$

and

$$\begin{bmatrix} d_{xx} & d_{xy} & d_{xz} \\ d_{yx} & d_{yy} & d_{yz} \\ d_{zx} & d_{zy} & d_{zz} \end{bmatrix} = \begin{bmatrix} \frac{\partial u_x}{\partial x} & \frac{1}{2}\left(\frac{\partial u_x}{\partial y} + \frac{\partial u_y}{\partial x}\right) & \frac{1}{2}\left(\frac{\partial u_x}{\partial z} + \frac{\partial u_z}{\partial x}\right) \\ \frac{1}{2}\left(\frac{\partial u_y}{\partial x} + \frac{\partial u_x}{\partial y}\right) & \frac{\partial u_y}{\partial y} & \frac{1}{2}\left(\frac{\partial u_y}{\partial z} + \frac{\partial u_z}{\partial y}\right) \\ \frac{1}{2}\left(\frac{\partial u_z}{\partial x} + \frac{\partial u_x}{\partial z}\right) & \frac{1}{2}\left(\frac{\partial u_z}{\partial y} + \frac{\partial u_y}{\partial z}\right) & \frac{\partial u_z}{\partial z} \end{bmatrix}. \tag{5.15}$$

The Oldroyd-B fluid flow is simulated using cylindrical coordinates and one thus has (5.4) in the form

$$T_{rr} + \lambda\left(u_r\frac{\partial T_{rr}}{\partial r} + u_z\frac{\partial T_{rr}}{\partial z} - 2\left(\frac{\partial u_r}{\partial r}T_{rr} + \frac{\partial u_r}{\partial z}T_{rz}\right)\right) = 2\mu_p\frac{\partial u_r}{\partial r}, \tag{5.16}$$

$$T_{rz} + \lambda\left(u_r\frac{\partial T_{rz}}{\partial r} + u_z\frac{\partial T_{rz}}{\partial z} - \frac{\partial u_r}{\partial r}T_{rz} - \frac{\partial u_r}{\partial z}T_{zz} - \frac{\partial u_z}{\partial r}T_{rr} - \frac{\partial u_z}{\partial z}T_{rz}\right) = \mu_p\left(\frac{\partial u_r}{\partial z} + \frac{\partial u_z}{\partial r}\right), \tag{5.17}$$

$$T_{zz} + \lambda\left(u_r\frac{\partial T_{zz}}{\partial r} + u_z\frac{\partial T_{zz}}{\partial z} - 2\left(\frac{\partial u_z}{\partial r}T_{rz} + \frac{\partial u_z}{\partial z}T_{zz}\right)\right) = 2\mu_p\frac{\partial u_z}{\partial z}, \tag{5.18}$$

$$T_{\theta\theta} + \lambda\left(u_r\frac{\partial T_{\theta\theta}}{\partial r} + u_z\frac{\partial T_{\theta\theta}}{\partial z} - 2\frac{u_r}{r}T_{\theta\theta}\right) = 2\mu_p\frac{u_r}{r}, \tag{5.19}$$

where $T_{rr},\ T_{rz},\ T_{zz},\ T_{\theta\theta}$ are components of the extra stress due to viscoelasticity $\boldsymbol{\tau_v}$.

5.3 Galerkin/Collocation 1D-RBFN technique

The computational domain is simply represented by a Cartesian grid. On each grid line, 1D-IRBFNs are employed to approximate the field variables, i.e. ψ,

ω, T_{xx}, T_{xy}, T_{yy}, T_{xz}, T_{yz}, T_{rr}, T_{rz}, T_{zz} and $T_{\theta\theta}$. The governing equations (5.5)-(5.6), (5.9)-(5.13) and (5.16)-(5.19) are discretised by means of point collocation (the residual set to zero at the collocation points) or Galerkin formulation (the residual set to zero in the mean). In the following, details are presented for three main parts of the proposed methods. In the first part, the use of 1D-IRBFNs to represent the field variables is discussed. In the second part, the implementation of boundary conditions is described. In the third part, 1D-IRBFs are incorporated into the Galerkin and point-collocation formulations as the trial functions.

5.3.1 One-dimensional IRBFN representation of the field variables

It can be seen that (5.5) - (5.6) involve second-order derivatives of the field variables including stresses. As a result, the second-order integral RBF scheme (Mai-Duy and Tran-Cong, 2003) is applied in this work. Processes of constructing the 1D-IRBFN approximations for the field variables can be conducted in a similar fashion. For brevity, we introduce the notation f to represent ψ, ω, T_{xx}, T_{xy}, T_{yy}, T_{xz}, T_{yz}, T_{rr}, T_{rz}, T_{zz} or $T_{\theta\theta}$, and the notation η to denote x or y (Cartesian coordinates) and r or z (cylindrical coordinates).

On an η grid line, the field variable f and its derivatives with respect to η can be represented as follows.

$$\frac{d^2 f(\eta)}{d\eta^2} = \sum_{i=1}^{N_\eta} w_i g_i(\eta) = \sum_{i=1}^{N_\eta} w_i I_i^{(2)}(\eta), \tag{5.20}$$

$$\frac{df(\eta)}{d\eta} = \sum_{i=1}^{N_\eta} w_i I_i^{(1)}(\eta) + C_1, \tag{5.21}$$

$$f(\eta) = \sum_{i=1}^{N_\eta} w_i I_i^{(0)}(\eta) + C_1\eta + C_2, \tag{5.22}$$

where N_η is the number of nodes on the grid line, $\{w_i\}_{i=1}^{N_\eta}$ the set of network weights, $\{g_i(\eta)\}_{i=1}^{N_\eta} \equiv \left\{I_i^{(2)}(\eta)\right\}_{i=1}^{N_\eta}$ the set of RBFs, $I_i^{(1)}(\eta) = \int I_i^{(2)}(\eta)d\eta$, $I_i^{(0)}(\eta) = \int I_i^{(1)}(\eta)\,d\eta$, and C_1 and C_2 are the constants of integration.

Evaluation of (5.20) - (5.22) at every node on the grid line leads to

$$\widehat{\frac{d^2f}{d\eta^2}} = \widehat{\mathcal{I}}^{(2)}\widehat{\alpha}, \tag{5.23}$$

$$\widehat{\frac{df}{d\eta}} = \widehat{\mathcal{I}}^{(1)}\widehat{\alpha}, \tag{5.24}$$

$$\widehat{f} = \widehat{\mathcal{I}}^{(0)}\widehat{\alpha}, \tag{5.25}$$

where superscript (.) is used to denote the order of the corresponding derivative function,

$$\widehat{\mathcal{I}}^{(2)} = \begin{bmatrix} I_1^{(2)}(\eta_1), & I_2^{(2)}(\eta_1), & \cdots, & I_{N_\eta}^{(2)}(\eta_1), & 0, & 0 \\ I_1^{(2)}(\eta_2), & I_2^{(2)}(\eta_2), & \cdots, & I_{N_\eta}^{(2)}(\eta_2), & 0, & 0 \\ \vdots & \vdots & \ddots & \vdots & \vdots & \vdots \\ I_1^{(2)}(\eta_{N_\eta}), & I_2^{(2)}(\eta_{N_\eta}), & \cdots, & I_{N_\eta}^{(2)}(\eta_{N_\eta}), & 0, & 0 \end{bmatrix},$$

$$\widehat{\mathcal{I}}^{(1)} = \begin{bmatrix} I_1^{(1)}(\eta_1), & I_2^{(1)}(\eta_1), & \cdots, & I_{N_\eta}^{(1)}(\eta_1), & 1, & 0 \\ I_1^{(1)}(\eta_2), & I_2^{(1)}(\eta_2), & \cdots, & I_{N_\eta}^{(1)}(\eta_2), & 1, & 0 \\ \vdots & \vdots & \ddots & \vdots & \vdots & \vdots \\ I_1^{(1)}(\eta_{N_\eta}), & I_2^{(1)}(\eta_{N_\eta}), & \cdots, & I_{N_\eta}^{(1)}(\eta_{N_\eta}), & 1, & 0 \end{bmatrix},$$

$$\widehat{\mathcal{I}}^{(0)} = \begin{bmatrix} I_1^{(0)}(\eta_1), & I_2^{(0)}(\eta_1), & \cdots, & I_{N_\eta}^{(0)}(\eta_1), & \eta_1, & 1 \\ I_1^{(0)}(\eta_2), & I_2^{(0)}(\eta_2), & \cdots, & I_{N_\eta}^{(0)}(\eta_2), & \eta_2, & 1 \\ \vdots & \vdots & \ddots & \vdots & \vdots & \vdots \\ I_1^{(0)}(\eta_{N_\eta}), & I_2^{(0)}(\eta_{N_\eta}), & \cdots, & I_{N_\eta}^{(0)}(\eta_{N_\eta}), & \eta_{N_\eta}, & 1 \end{bmatrix};$$

$$\widehat{\alpha} = \left(w_1, w_2, \cdots, w_{N_\eta}, C_1, C_2\right)^T;$$

and

$$\begin{aligned}\widehat{\frac{d^k f}{d\eta^k}} &= \left(\frac{d^k f_1}{d\eta^k}, \frac{d^k f_2}{d\eta^k}, \cdots, \frac{d^k f_{N_\eta}}{d\eta^k}\right)^T, \qquad k = \{1, 2\}, \\ \widehat{f} &= \left(f_1, f_2, \cdots, f_{N_\eta}\right)^T,\end{aligned}$$

in which $d^k f_j/d\eta^k = d^k f\left(\eta_j\right)/d\eta^k$ and $f_j = f\left(\eta_j\right)$ with $j = \{1, 2, \cdots, N_\eta\}$.

The relations between the RBF-coefficient space $\widehat{\alpha}$ and the physical space $\widehat{f}$ can be established as

$$\begin{pmatrix} \widehat{f} \\ \widehat{e} \end{pmatrix} = \begin{bmatrix} \widehat{\mathcal{I}}^{(0)} \\ \widehat{\mathcal{K}} \end{bmatrix} \widehat{\alpha} = \widehat{\mathcal{C}}\widehat{\alpha}, \tag{5.26}$$

$$\widehat{\alpha} = \widehat{\mathcal{C}}^{-1} \begin{pmatrix} \widehat{f} \\ \widehat{e} \end{pmatrix}, \tag{5.27}$$

where $\widehat{e} = \widehat{\mathcal{K}}\widehat{\alpha}$ is used to represent extra information (derivative data), which would otherwise be wasted resulting in less accurate solutions, and $\widehat{\mathcal{C}}$ the conversion matrix. In (5.26) - (5.27), owing to the presence of the two integration constants, the vector $\widehat{e}$ can have up to two entries. Since the conversion matrix $\widehat{\mathcal{C}}$ is not over-determined, extra values e_i are incorporated into the IRBFN approximations in an exact manner. We will utilise this capability to impose normal derivative values at the two end-points of the grid line as well as to derive a computational boundary condition for the vorticity.

Making use of (5.27), the values of f and its derivatives at an arbitrary point η

on the grid line will be computed by

$$f(\eta) = \left(I_1^{(0)}(\eta), I_2^{(0)}(\eta), \cdots, I_{N_\eta}^{(0)}(\eta), \eta, 1\right) \widehat{\mathcal{C}}^{-1} \begin{pmatrix} \widehat{f} \\ \widehat{e} \end{pmatrix}, \tag{5.28}$$

$$\frac{\partial f(\eta)}{\partial \eta} = \left(I_1^{(1)}(\eta), I_2^{(1)}(\eta), \cdots, I_{N_\eta}^{(1)}(\eta), 1, 0\right) \widehat{\mathcal{C}}^{-1} \begin{pmatrix} \widehat{f} \\ \widehat{e} \end{pmatrix}, \tag{5.29}$$

$$\frac{\partial^2 f(\eta)}{\partial \eta^2} = \left(I_1^{(2)}(\eta), I_2^{(2)}(\eta), \cdots, I_{N_\eta}^{(2)}(\eta), 0, 0\right) \widehat{\mathcal{C}}^{-1} \begin{pmatrix} \widehat{f} \\ \widehat{e} \end{pmatrix}. \tag{5.30}$$

They can be rewritten in compact form

$$f(\eta) = \sum_{i=1}^{N_\eta} \varphi_i(\eta) f_i + \varphi_{N_\eta+1}(\eta) e_1 + \varphi_{N_\eta+2}(\eta) e_2, \tag{5.31}$$

$$\frac{\partial f(\eta)}{\partial \eta} = \sum_{i=1}^{N_\eta} \frac{\partial \varphi_i(\eta)}{\partial \eta} f_i + \frac{\partial \varphi_{N_\eta+1}(\eta)}{\partial \eta} e_1 + \frac{\partial \varphi_{N_\eta+2}(\eta)}{\partial \eta} e_2, \tag{5.32}$$

$$\frac{\partial^2 f(\eta)}{\partial \eta^2} = \sum_{i=1}^{N_\eta} \frac{\partial^2 \varphi_i(\eta)}{\partial \eta^2} f_i + \frac{\partial^2 \varphi_{N_\eta+1}(\eta)}{\partial \eta^2} e_1 + \frac{\partial^2 \varphi_{N_\eta+2}(\eta)}{\partial \eta^2} e_2, \tag{5.33}$$

where $\{\varphi_i\}_{i=1}^{N_\eta+2}$ is the set of IRBFN basis functions in the physical space.

5.3.2 Imposition of boundary conditions

Dirichlet boundary conditions: Assume that f is given at η_1 and η_{N_η}. In the conversion process, (5.26) - (5.27), the matrix $\widehat{\mathcal{K}}$ and the vector $\widehat{e}$ are simply

set to null. The 1D-IRBFN expressions (5.31) - (5.33) thus reduce to

$$f(\eta) = \sum_{i=1}^{N_\eta} \varphi_i(\eta) f_i, \tag{5.34}$$

$$\frac{\partial f(\eta)}{\partial \eta} = \sum_{i=1}^{N_\eta} \frac{\partial \varphi_i(\eta)}{\partial \eta} f_i, \tag{5.35}$$

$$\frac{\partial^2 f(\eta)}{\partial \eta^2} = \sum_{i=1}^{N_\eta} \frac{\partial^2 \varphi_i(\eta)}{\partial \eta^2} f_i. \tag{5.36}$$

Neumann boundary conditions: Assume that $\partial f/\partial \eta$ is given at η_1 and η_{N_η}. The matrix $\widehat{\mathcal{K}}$ and the vector $\widehat{e}$ in (5.26) - (5.27) take the form

$$\widehat{\mathcal{K}} = \begin{bmatrix} I_1^{(1)}(\eta_1), & I_2^{(1)}(\eta_1), & \cdots, & I_{N_\eta}^{(1)}(\eta_1), & 1, & 0 \\ I_1^{(1)}(\eta_{N_\eta}), & I_2^{(1)}(\eta_{N_\eta}), & \cdots, & I_{N_\eta}^{(1)}(\eta_{N_\eta}), & 1, & 0 \end{bmatrix},$$

$$\widehat{e} = \begin{pmatrix} \frac{\partial f_1}{\partial \eta} \\ \frac{\partial f_{N_\eta}}{\partial \eta} \end{pmatrix}.$$

The 1D-IRBFN expressions (5.31) - (5.33) thus become

$$f(\eta) = \sum_{i=1}^{N_\eta} \varphi_i(\eta) f_i + \varphi_{N_\eta+1}(\eta) \frac{\partial f_1}{\partial \eta} + \varphi_{N_\eta+2}(\eta) \frac{\partial f_{N_\eta}}{\partial \eta}, \tag{5.37}$$

$$\frac{\partial f(\eta)}{\partial \eta} = \sum_{i=1}^{N_\eta} \frac{\partial \varphi_i(\eta)}{\partial \eta} f_i + \frac{\partial \varphi_{N_\eta+1}(\eta)}{\partial \eta} \frac{\partial f_1}{\partial \eta} + \frac{\partial \varphi_{N_\eta+2}(\eta)}{\partial \eta} \frac{\partial f_{N_\eta}}{\partial \eta}, \tag{5.38}$$

$$\frac{\partial^2 f(\eta)}{\partial \eta^2} = \sum_{i=1}^{N_\eta} \frac{\partial^2 \varphi_i(\eta)}{\partial \eta^2} f_i + \frac{\partial^2 \varphi_{N_\eta+1}(\eta)}{\partial \eta^2} \frac{\partial f_1}{\partial \eta} + \frac{\partial^2 \varphi_{N_\eta+2}(\eta)}{\partial \eta^2} \frac{\partial f_{N_\eta}}{\partial \eta}. \tag{5.39}$$

Dirichlet and Neumann boundary conditions: Assume that f and $\partial f/\partial \eta$ are given at η_1 and η_{N_η}, respectively. The latter is imposed by taking the matrix

$\widehat{\mathcal{K}}$ and the vector $\widehat{e}$ in (5.26) - (5.27) as

$$\begin{aligned} \widehat{\mathcal{K}} &= \left[I_1^{(1)}\left(\eta_{N_\eta}\right),\ I_2^{(1)}\left(\eta_{N_\eta}\right),\ \cdots,\ I_{N_\eta}^{(1)}\left(\eta_{N_\eta}\right),\ 1,\ 0 \right], \\ \widehat{e} &= \left(\frac{\partial f_{N_\eta}}{\partial \eta} \right). \end{aligned}$$

One thus has (5.31) - (5.33) in the form

$$f(\eta) = \sum_{i=1}^{N_\eta} \varphi_i(\eta) f_i + \varphi_{N_\eta+1}(\eta) \frac{\partial f_{N_\eta}}{\partial \eta}, \tag{5.40}$$

$$\frac{\partial f(\eta)}{\partial \eta} = \sum_{i=1}^{N_\eta} \frac{\partial \varphi_i(\eta)}{\partial \eta} f_i + \frac{\partial \varphi_{N_\eta+1}(\eta)}{\partial \eta} \frac{\partial f_{N_\eta}}{\partial \eta}, \tag{5.41}$$

$$\frac{\partial^2 f(\eta)}{\partial \eta^2} = \sum_{i=1}^{N_\eta} \frac{\partial^2 \varphi_i(\eta)}{\partial \eta^2} f_i + \frac{\partial^2 \varphi_{N_\eta+1}(\eta)}{\partial \eta^2} \frac{\partial f_{N_\eta}}{\partial \eta}. \tag{5.42}$$

5.3.3 Incorporating 1D-IRBFNs into Galerkin and point-collocation formulations

Each governing equation in (5.5) - (5.6), (5.9) - (5.13) and (5.16) - (5.19) can be rewritten in the following form

$$\mathcal{L}(f) = 0, \qquad \mathbf{x} \in \Omega, \tag{5.43}$$

where $\mathcal{L}$ is a differential operator. 1D-IRBFN expressions (5.31) - (5.33) are utilised here to construct the approximations for f over Ω. On a 2D rectangular domain, this construction process can simply be done by means of Kronecker

products. The use of tensor products leads to, for instance,

$$f(x,y) = \sum_{i=1}^{N_x}\sum_{j=1}^{N_y} \varphi_i^{[x]}(x)\varphi_j^{[y]}(y)\, f_{i,j}, \tag{5.44}$$

for the case of Dirichlet boundary conditions only, and

$$f(x,y) = \sum_{i=1}^{N_x} \varphi_i^{[x]}(x) \left(\sum_{j=1}^{N_y} \varphi_j^{[y]}(y)\, f_{i,j} + \varphi_{N_y+1}^{[y]}(y) \frac{\partial f_{i,1}}{\partial y} + \varphi_{N_y+2}^{[y]}(y) \frac{\partial f_{i,N_y}}{\partial y} \right). \tag{5.45}$$

for the case of Dirichlet and Neumann boundary conditions (Dirichlet conditions prescribed on the two vertical boundaries while Neumann conditions on the two horizontal boundaries). In (5.44) and (5.45), $f_{i,j}$ is the value of the variable f at the intersection of the ith horizontal grid line and jth vertical grid line, and $\partial f_{i,1}/\partial y$ and $\partial f_{i,N_y}/\partial y$ are nodal boundary derivative values. The products $\varphi_i^{(x)}\varphi_j^{(y)}$ are usually referred to as the trial/basis/approximating functions.

It is noted that the independent variables x and y in (5.44) - (5.45) will be replaced with r and z if cylindrical coordinates are employed.

One can find the unknown nodal values of f by constructing a scheme to minimise the following residual

$$R = L(f). \tag{5.46}$$

This process can be stated mathematically as

$$\int_\Omega W R d\Omega = 0, \tag{5.47}$$

where W is the weighting function to be chosen. In the point-collocation approach, the weighting function is chosen as the Dirac delta function, i.e. $W_i = \delta(x - x_i)$. In the Galerkin approach, the weighting function is chosen from the set of trial functions, i.e. $W_i = \phi_i(\mathbf{x})$, and the volume integrals in (5.47) can be numerically evaluated using Gauss quadrature.

As mentioned earlier, Neumann boundary conditions are presently imposed in an exact manner. This is numerically demonstrated here through the solution of the following ODE

$$\frac{d^2 f}{dx^2} + f + x = 0, \quad 0 \leq x \leq 1, \tag{5.48}$$

subject to a Dirichlet and Neumann boundary condition at $x = 0$ and $x = 1$, respectively.

In the case of conventional Galerkin methods, the approximation for f can be constructed to satisfy the Dirichlet condition at $x = 0$. The Neumann boundary condition $df/dx = \overline{q}$ at $x = 1$ is imposed through the following statement

$$\int_0^1 \left(\frac{df}{dx}\frac{dW}{dx} - (f + x)\, W \right) dx = \left[\overline{q} W\right]_{x=1}, \tag{5.49}$$

which is obtained by applying integration by parts on (5.47). As shown in (Brebbia et al., 1984), by differentiating the approximate function f, one has

$$\left.\frac{df}{dx}\right|_{x=1} = 1.22\text{E-}1 + (1 + 1.22\text{E-}1)\overline{q},$$

which clearly indicates that the Neumann boundary condition is imposed in an approximate manner.

In the present Galerkin technique, the IRBFN approximation is constructed to satisfy not only the Dirichlet condition at $x = 0$ but also the Neumann boundary

condition $df/dx = \overline{q}$ at $x = 1$. Using (5.40), the solution f is expressed as

$$f(x) = \sum_{i=1}^{N_x} \varphi_i(x) f_i + \varphi_{N_x+1}(x)\bar{q}. \tag{5.50}$$

This approximation is then forced to satisfy the ODE through

$$\int_0^1 \left(\frac{d^2 f}{dx} + f + x\right) W dx = 0, \tag{5.51}$$

from which one is able to obtain the nodal values of f. By differentiating (5.50), one has

$$\left.\frac{df}{dx}\right|_{x=1} = \sum_{i=1}^{N_x} \frac{d\varphi_i\,(x=1)}{dx} f_i + \frac{d\varphi_{N_x+1}\,(x=1)}{dx}\bar{q}.$$

With $N_x = 5$, it reduces to

$$\left.\frac{df}{dx}\right|_{x=1} = \text{(-1.87E-14)} + (1 + \text{5.07E-14})\overline{q} \simeq \overline{q},$$

which clearly shows that the Neumann boundary condition is imposed in an exact manner.

5.4 Numerical results

The proposed methods are validated through the simulation of viscoelastic flows in rectangular ducts (with Galerkin formulation), and in straight and corrugated tubes (point collocation) with circular cross sections. Fluid models under consideration here are CEF and Oldroyd-B. We employ uniform Cartesian grids to represent the computational domain and implement 1D-IRBFNs with the multiquadric (MQ) function

$$g_i\,(\eta) = \sqrt{(\eta - c_i)^2 + a_i^2}, \tag{5.52}$$

where c_i and a_i are the centre and the width/shape-parameter of the ith MQ-RBF, respectively. The latter is simply chosen to be the grid size.

5.4.1 Problem 1: Fully-developed flows of CEF fluid in rectangular ducts

The flow of a viscoelastic fluid in a rectangular duct has received a great deal of attention because of its fundamental and practical importance. Such a flow was simulated with different constitutive models, e.g., Reiner-Rivlin (Green and Rivlin, 1956), CEF (Gervang and Larsen, 1991; Mai-Duy and Tanner, 2006) and modified PTT (MPTT) (Xue et al., 1995). Results by Gervang and Larsen (1991), where the CEF model is employed and simulations are conducted both numerically and experimentally, are often cited in the literature for comparison purposes. In this study, we also consider the CEF model and its parameters are taken to be the same as those in (Gervang and Larsen, 1991). The governing equations are expressed in terms of streamfunction, vorticity, pressure and primary velocity as

$$\frac{\partial^2 \psi}{\partial x^2} + \frac{\partial^2 \psi}{\partial y^2} + \omega = 0, \tag{5.53}$$

$$\mu \left(\frac{\partial^2 \omega}{\partial x^2} + \frac{\partial^2 \omega}{\partial y^2} \right) = \rho \left(\frac{\partial \psi}{\partial y} \frac{\partial \omega}{\partial x} - \frac{\partial \psi}{\partial x} \frac{\partial \omega}{\partial y} \right) - \frac{\partial^2 T_{xy}}{\partial x^2} + \frac{\partial^2 \left(T_{xx} - T_{yy} \right)}{\partial x \partial y} + \frac{\partial^2 T_{xy}}{\partial y^2}, \tag{5.54}$$

$$\mu \left(\frac{\partial^2 u_z}{\partial x^2} + \frac{\partial^2 u_z}{\partial y^2} \right) = \frac{\partial p}{\partial z} + \rho \left(\frac{\partial \psi}{\partial y} \frac{\partial u_z}{\partial x} - \frac{\partial \psi}{\partial x} \frac{\partial u_z}{\partial y} \right) - \frac{\partial T_{zx}}{\partial x} - \frac{\partial T_{zy}}{\partial y}, \tag{5.55}$$

where the function F in (5.6) is now given explicitly. The flow is generated by a pressure drop $\partial p/\partial z$ and the computation domain is only a 2D region (cross-section) on the $x-y$ plane. Let χ be the aspect ratio. Four values of χ, namely 1, 1.56, 4 and 6.25, are considered.

Non-slip boundary conditions lead to $\psi = 0$, $u_z = 0$ and $\partial \psi / \partial n = 0$ on the wall

(n is the coordinate direction normal to the wall). The condition $\partial\psi/\partial n = 0$ is used to derive a computational boundary condition for ω. This process is carried out here with the help of the integration constants; the detailed implementation is presented in Section 3.3.2. Equations (5.53) - (5.55) for ψ, ω and u_z are thus all subject to Dirichlet boundary conditions.

We apply the Galerkin formulation to discretise the governing equations and a Picard iterative scheme to handle the resultant nonlinear system of algebraic equations. All the terms on the RHS of (5.54) and (5.55) are lumped together in the "pseudo-body forces". The solution procedure can be summarised as follows.

1. Discretise spatial derivatives using 1D-IRBFNs, resulting in a high-order approximation scheme in space
2. Guess values of ψ, ω and u_z, and their first-order spatial derivatives
3. Compute the pseudo-body forces and the boundary values for ω. It is noted that the CEF stress components are simply obtained through direct calculation of (5.9) - (5.13)
4. Solve the coupled linearised governing equations (5.53) - (5.55), where the system matrix is generated from the linear terms on their LHS
5. Check to see whether the solution has reached a steady state

$$\frac{\sqrt{\sum_{i=1}^{N}\left(\psi_i^{(k)}-\psi_i^{(k-1)}\right)^2+\sum_{i=1}^{N}\left(\omega_i^{(k)}-\omega_i^{(k-1)}\right)^2+\sum_{i=1}^{N}\left(u_{zi}^{(k)}-u_{zi}^{(k-1)}\right)^2}}{\sqrt{\sum_{i=1}^{N}\left(\psi_i^{(k)}\right)^2+\sum_{i=1}^{N}\left(\omega_i^{(k)}\right)^2+\sum_{i=1}^{N}\left(u_{zi}^{(k)}\right)^2}}<\epsilon, \tag{5.56}$$

where k indicates the iteration number and ϵ is a prescribed tolerance

6. If it is not satisfied, for every interior node, relax the solution fields

$$\psi_i = \gamma\psi_i^{(k)} + (1-\gamma)\,\psi_i^{(k-1)}, \tag{5.57}$$

$$\omega_i = \gamma\omega_i^{(k)} + (1-\gamma)\,\omega_i^{(k-1)}, \tag{5.58}$$

$$u_{zi} = \gamma u_{zi}^{(k)} + (1-\gamma)\,u_{zi}^{(k-1)}, \tag{5.59}$$

where γ is the relaxation factor ($0 < \gamma < 1$), and then repeat from step 3. Otherwise, stop the computation and output the results.

Computations are carried out using $\gamma = 0.01$ and grids of $\{11 \times 11, 21 \times 21, \cdots, 61 \times 61\}$. Figures 5.1 and 5.2 show the convergence behaviour of the streamfunction and vorticity fields at $\chi = 1$, respectively. It can be seen that the flow is symmetric about the vertical and horizontal centreline and the two fields converge very fast with grid refinement. There are eight vortices in total, where secondary circulations have the same magnitude but different signs (i.e. one vortex is in opposite direction to its two adjacent vortices). Figures 5.3 and 5.4 show patterns of the secondary flow for $\chi = \{1.56, 4, 6.25\}$ on one quarter of the cross-section. Each quadrant has two vortices, whose patterns and strength strongly depend on the aspect ratio for a given mean primary velocity. Unlike the case of $\chi = 1$, where the two vortices are symmetric about the diagonal plane, the case of $\chi > 1$ produces two vortices of different sizes. The vortex near the long wall moves towards the short wall with increasing χ, while the vortex near the short wall is reduced in size. Figures 5.5 and 5.6 show patterns of the primary flow and the second normal stress difference for all aspect ratios. The 1D-IRBFN Galerkin results are similar to those reported in (Gervang and Larsen, 1991; Xue et al., 1995).

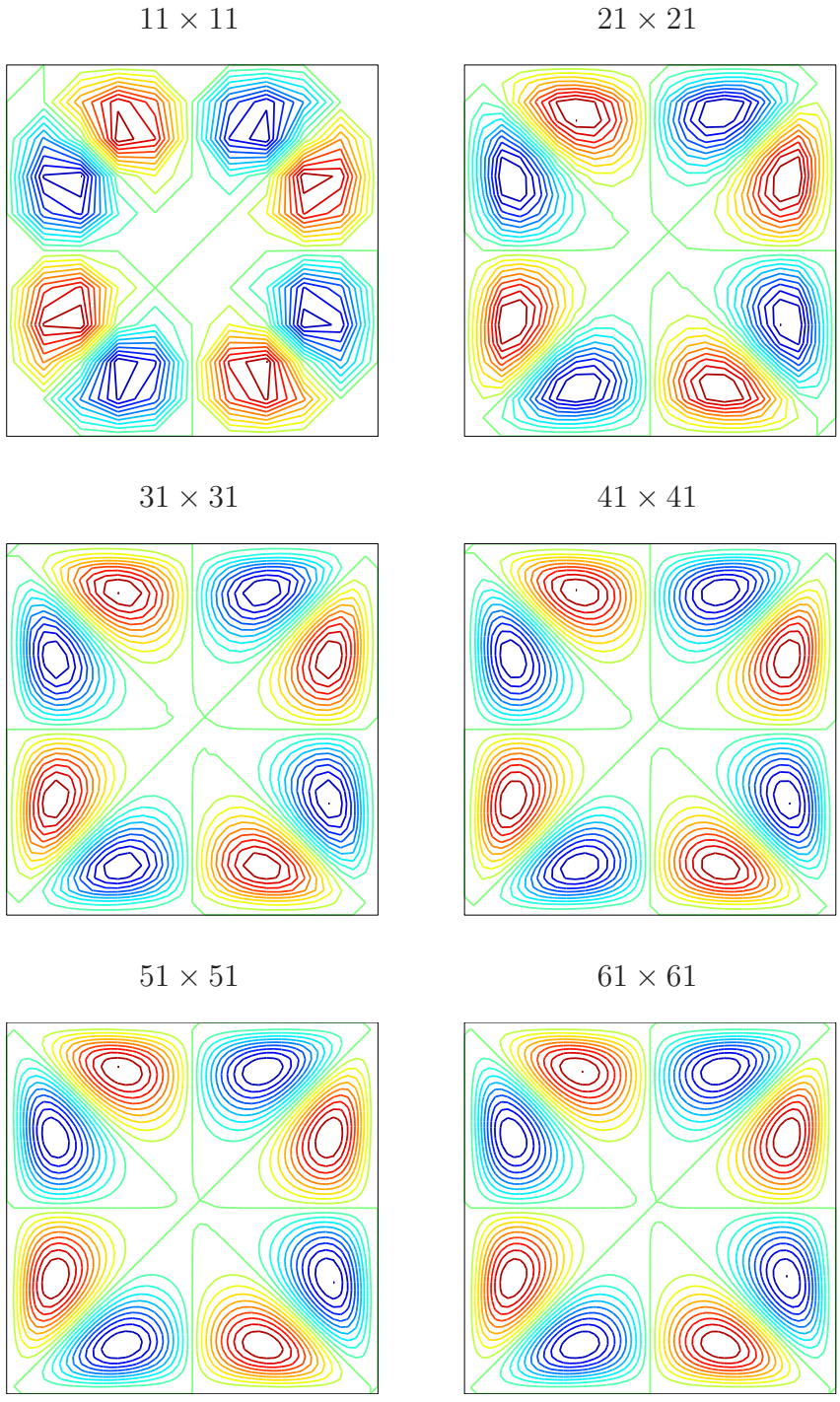

Figure 5.1: Problem 1: Convergence behaviour of the streamfunction field with respect to grid refinement.

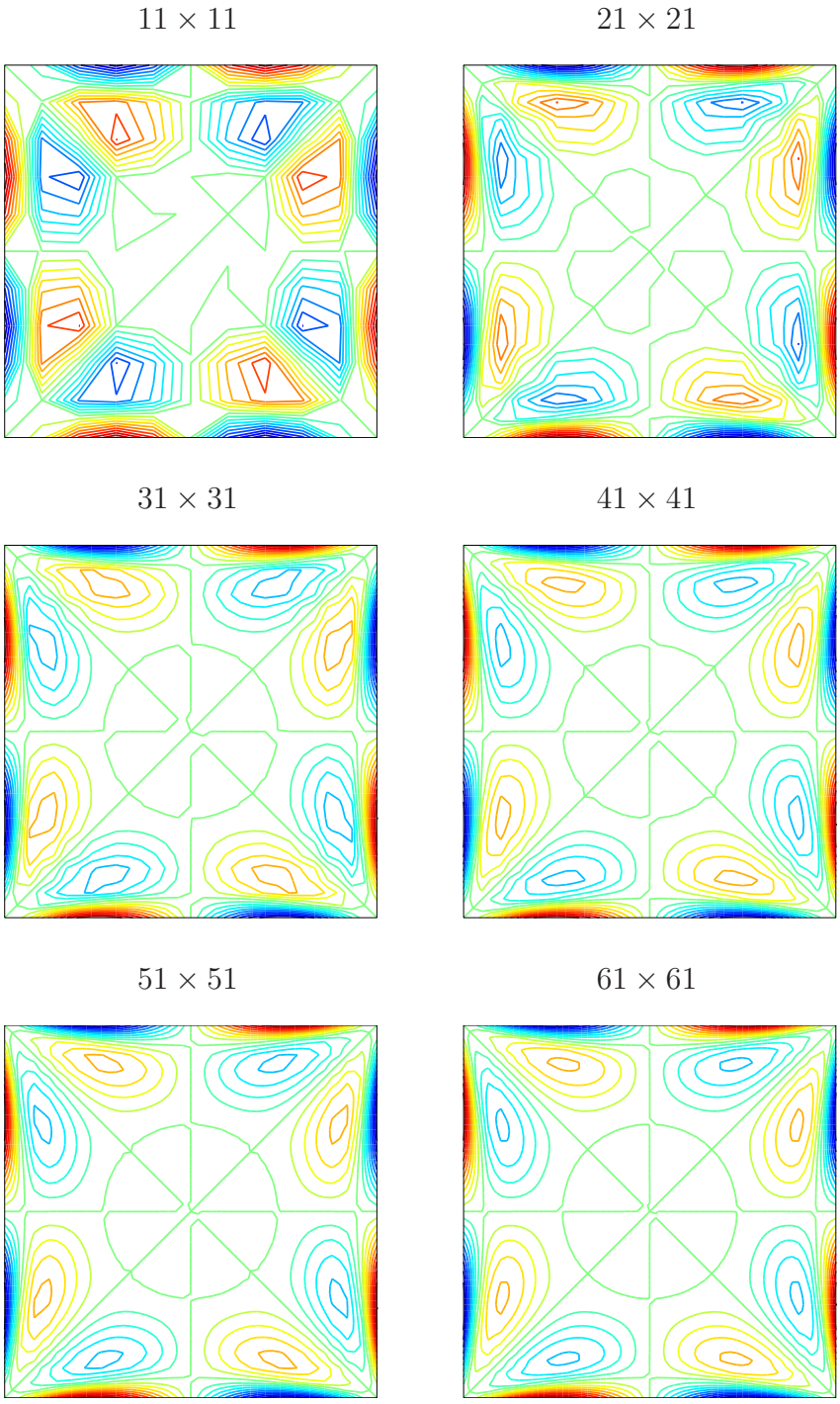

Figure 5.2: Problem 1: Convergence behaviour of the vorticity field with respect to grid refinement.

a) $\chi = 1.56$, 61×61

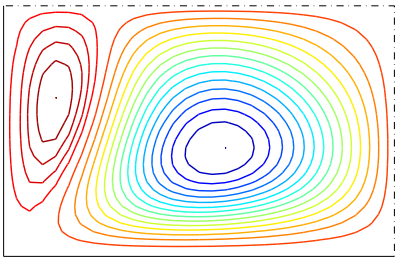

b) $\chi = 4$, 81×61

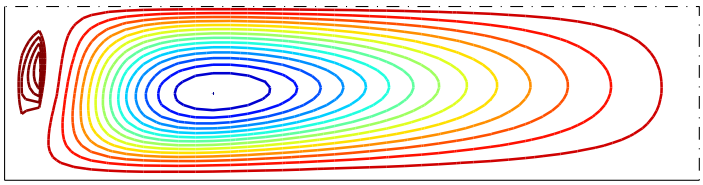

c) $\chi = 6.25$, 81×61

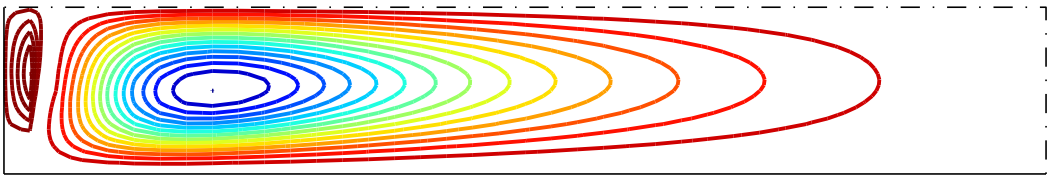

Figure 5.3: Problem 1: Streamlines of the secondary flow in one quarter of the cross section for several values of the aspect ratio.

a) $\chi = 1.56$, 61×61

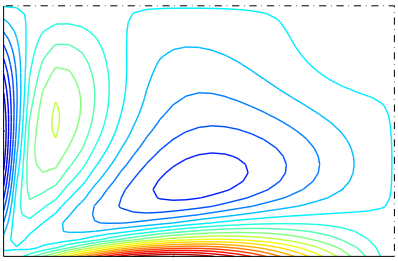

b) $\chi = 4$, 81×61

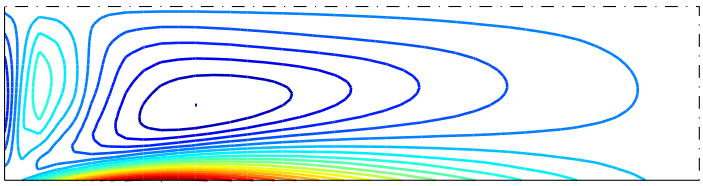

c) $\chi = 6.25$, 81×61

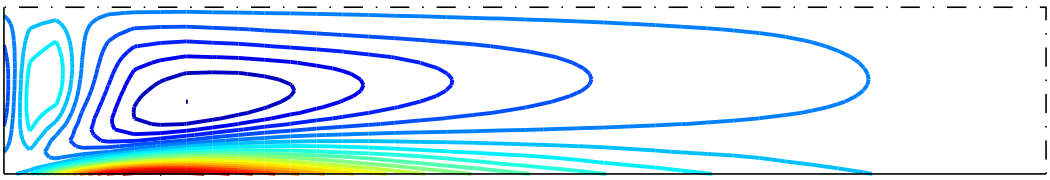

Figure 5.4: Problem 1: Contour plots for the vorticity in one quarter of the cross-section computed for several values of the aspect ratio.

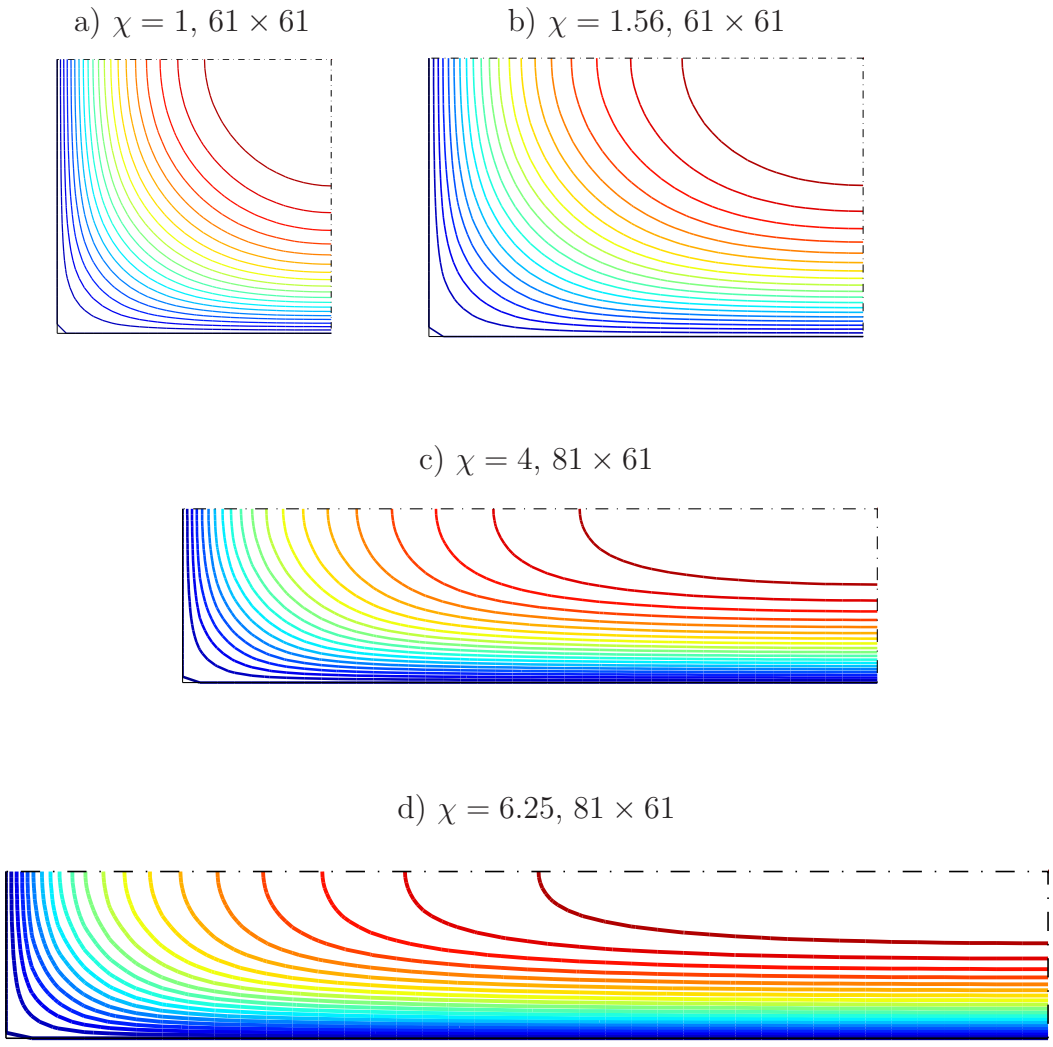

Figure 5.5: Problem 1: Contour plots for the primary velocity in one quarter of the cross-section computed for several values of the aspect ratio.

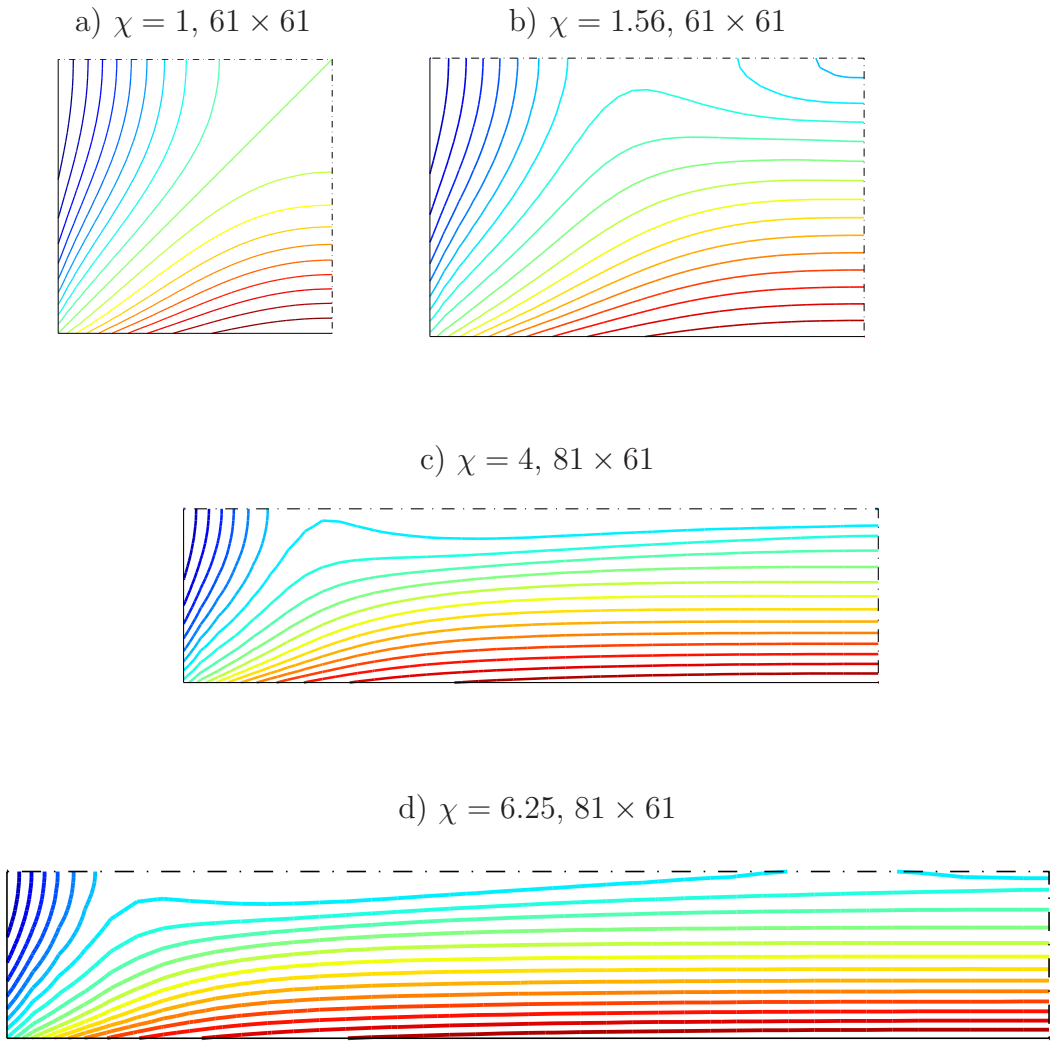

Figure 5.6: Problem 1: Contour plots for the second normal stress difference in one quarter of the cross-section computed for several values of the aspect ratio.

5.4.2 Problem 2: Fully-developed flows of Oldroyd-B fluid in circular tubes

This problem is concerned with the so-called Poiseuille flow in a circular tube. Let R be the radius of the tube. The governing equations (1.1) - (1.2) and (5.16) - (5.19) are made dimensionless by scaling lengths by R, velocity components by Q/R^2, and stress components and pressure by $(\mu_n + \mu_p)Q/R^3$ in which Q is the flow rate. In a cylindrical coordinate system, the non-dimensional form of (5.5) - (5.6) for the motion of an Oldroyd-B fluid is given by (Pilitsis and Beris, 1989)

$$\left(\frac{\partial^2\psi}{\partial r^2} + \frac{\partial^2\psi}{\partial z^2} - \frac{1}{r}\frac{\partial\psi}{\partial r}\right) + \omega = 0, \tag{5.60}$$

$$\alpha\left(\frac{\partial^2\omega}{\partial r^2} + \frac{1}{r}\frac{\partial\omega}{\partial r} - \frac{\omega}{r^2} + \frac{\partial^2\omega}{\partial z^2}\right) = \frac{\partial^2 T_{rz}}{\partial r^2} - \frac{\partial^2 T_{rr}}{\partial z\partial r} - \frac{\partial^2 T_{rz}}{\partial z^2} - \frac{1}{r}\left(\frac{\partial T_{rr}}{\partial z} - \frac{\partial T_{\theta\theta}}{\partial z}\right) + \frac{\partial^2 T_{zz}}{\partial r\partial z} - \frac{1}{r^2}T_{rz} + \frac{1}{r}\frac{\partial T_{rz}}{\partial r}, \tag{5.61}$$

where $\alpha = \mu_n/(\mu_n + \mu_p)$ and the inertia terms are set aside. The velocity and stress fields can be obtained analytically and their exact forms are

$$\widetilde{u}_z = 1 - r^2,\ \widetilde{u}_r = 0, \tag{5.62}$$

$$\widetilde{T}_{zz} = We(1-\alpha)\left(\tfrac{\partial\widetilde{u}_z}{\partial r}\right)^2,\ \widetilde{T}_{rz} = (1-\alpha)\tfrac{\partial\widetilde{u}_z}{\partial r},\ \widetilde{T}_{rr} = 0, \tag{5.63}$$

where $We = \lambda Q/R^3$ is the Weissenberg number. In the present simulation, the length and the radius of the tube are all chosen to be 1. Boundary conditions are prescribed as follows.

- On the centreline:

$$\psi = \omega = T_{rz} = \frac{\partial T_{rr}}{\partial r} = \frac{\partial T_{zz}}{\partial r} = \frac{\partial T_{\theta\theta}}{\partial r} = 0 \quad \text{(symmetrical conditions)}$$

- On the wall: Through (5.8) ($u_z = 1/r(\partial\psi/\partial r)$), the streamfunction value is determined as $\psi = Q/2\pi$. Given $Q = \pi/2$, one has $\psi = 1/4$. The vorticity value can be obtained using the same procedure as in Problem 1.

- On the inlet and the outlet:

$$\psi^i = \psi^o, \quad \frac{\partial \psi^i}{\partial n} = \frac{\partial \psi^o}{\partial n}, \quad \omega^i = \omega^o, \quad \frac{\partial \omega^i}{\partial n} = \frac{\partial \omega^o}{\partial n},$$

$$T^i_{rr} = T^o_{rr}, \quad T^i_{rz} = T^o_{rz}, \quad T^i_{zz} = T^o_{zz}, \quad T^i_{\theta\theta} = T^o_{\theta\theta},$$

  where periodicity is taken into account, and superscripts i and o denote the inlet and outlet, respectively.

Unlike Problem 1, the point-collocation formulation is employed here. We take $\alpha = 0.85$ and also apply a Picard iterative scheme to handle the nonlinearity of the system. Results obtained are presented in Table 5.1 and Figure 5.7. Table 5.1 is concerned with the study of grid convergence at $We = 9$. Errors are consistently reduced as the grid density increases. Figure 5.7 shows profiles of the velocity, the shear stress and the first normal stress difference on the middle plane ($z = 0.5$) for the Weissenberg number in the range of 0.5 to 10. It can be seen that the 1D-IRBFN collocation results agree well with the analytic solutions.

Table 5.1: Problem 2: Grid-convergence study at $We = 9$.

Grid	Relative L_2 norm of the error, N_e		
	$N_e(u_z)$	$N_e(T_{zz})$	$N_e(T_{rz})$
11×11	5.6228E-04	2.6259E-03	1.0973E-03
21×21	1.5928E-04	8.9349E-04	3.6454E-04
31×31	7.4343E-05	3.6953E-04	1.5495E-04
41×41	4.2581E-05	2.1614E-04	9.4571E-05
51×51	2.7541E-05	1.4178E-04	6.4001E-05

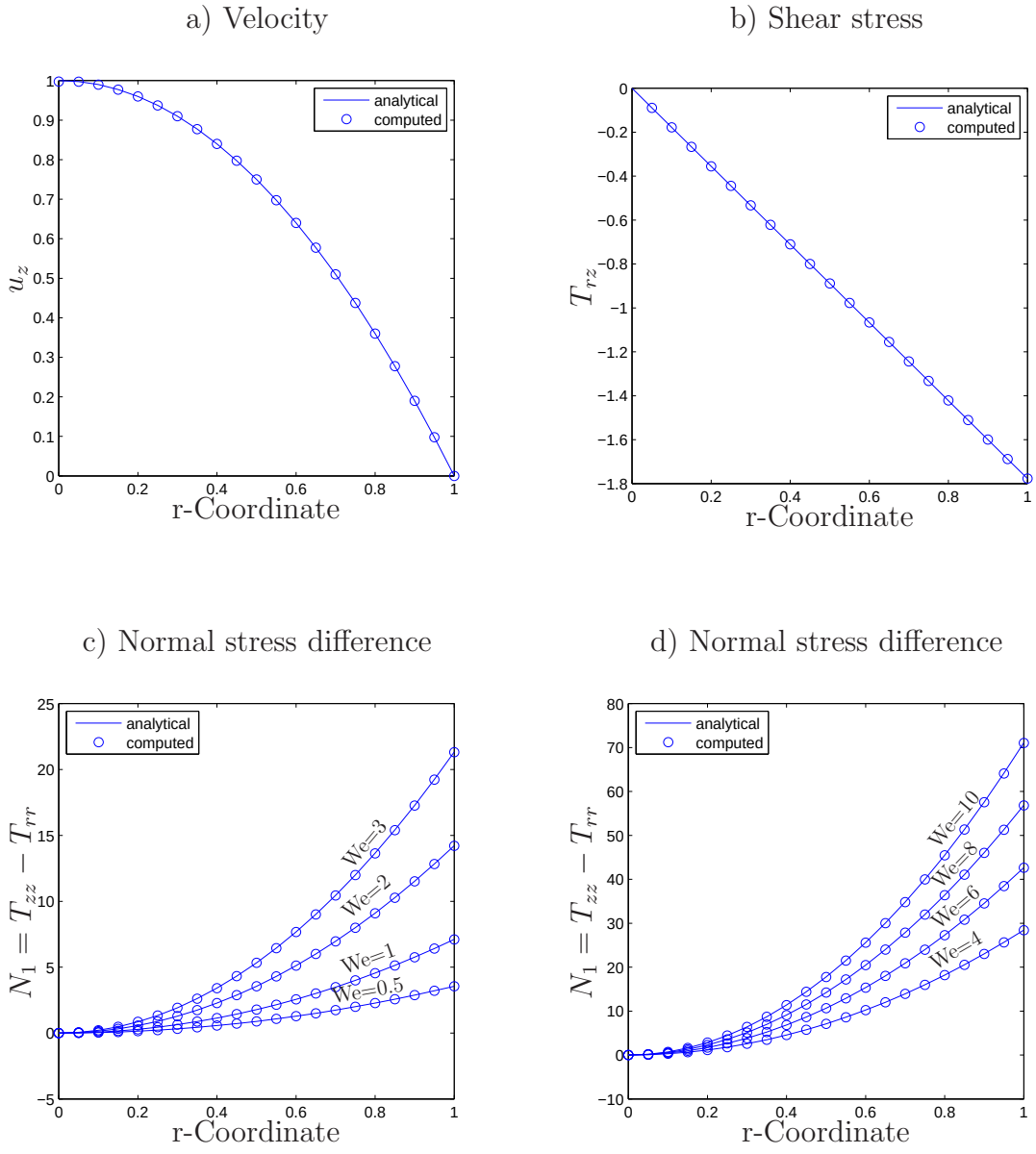

Figure 5.7: Problem 2: Profiles of velocity and stress on the middle plane $z = 0.5$ computed at several values of We using grid of 21×21. It is noted that u_z and T_{rz} are independent of We and their corresponding computed results are indistinguishable.

5.4.3 Problem 3: Flows of Oldroyd-B fluid in corrugated tubes

The 1D-IRBFN collocation method is further validated through the simulation of flows in corrugated tubes. It is well known that such flows, where their solutions are smooth and there are no inflow/outflow boundary conditions applied, are chosen as a benchmark test problem for validating new solvers in computational rheology. Solutions to these flows were reported for several numerical methods, e.g. the pseudospectral finite difference method (PSFD), pseudo-spectral cylindrical finite difference method (PCFD) and full pseudo-spectral method (FCC) by Pilitsis and Beris (1989, 1991, 1992), the spectral method (SM) by Momeni-Masuleh and Phillips (2004), EEME/FEM by Burdette et al. (1989); Rajagopalan et al. (1990), EVSS/FEM by Szady et al. (1995), BEM by Zheng et al. (1990), and 2D-IRBFN by Mai-Duy and Tanner (2006).

Figure 5.8a shows the flow geometry, where the radius of the corrugated tube along the z axis is given by

$$r_w = R(1 - \varepsilon \cos(2\pi z/L)), \tag{5.64}$$

where R is the average radius of an equivalent straight tube, ε the amplitude of the corrugation and L the wavelength. In addition to ε, two more characteristic dimensionless numbers are also used. They are the aspect ratio $N = R/L$ and the wave number l; their relation is $N = l/(2\pi)$. Since the flow is axisymmetric and periodic, only a reduced domain (Figure 5.8b) needs be considered for the numerical study.

The streamfunction and vorticity equations as well as the boundary conditions here are similar to those in Problem 2. The governing equations are solved in a stretched cylindrical coordinate system $(\widehat{r}, \theta, \widehat{z})$, where $\widehat{r} \equiv r/r_w$ and $\widehat{z} \equiv z$. One important measure for corrugated tube flows is the flow resistance defined

as

$$f\mathrm{Re} = \frac{2\pi\Delta P R^4}{L(\mu_n + \mu_p)Q}, \tag{5.65}$$

where ΔP is the constant pressure drop per unit cell.

Newtonian fluid

The proposed method is first tested with the case of a Newtonian fluid. With the presence of the inertial term, the vorticity equation (5.6) becomes (Pilitsis and Beris, 1991)

$$\left(\frac{\partial^2\omega}{\partial r^2} + \frac{1}{r}\frac{\partial\omega}{\partial r} - \frac{\omega}{r^2} + \frac{\partial^2\omega}{\partial z^2}\right) = \frac{\pi Re}{2}\left(u_z\frac{\partial\omega}{\partial z} + u_r\frac{\partial\omega}{\partial r} - \frac{u_r}{r}\omega\right), \tag{5.66}$$

where Re is the Reynolds number defined as

$$Re = \frac{2\rho Q}{\pi R\mu}. \tag{5.67}$$

Results concerning $f\mathrm{Re}$ for $Re = 0$ employed with several geometries by the present method and by SM, FCC, PSFD and PCFD are presented in Table 5.2. It can be seen that a good agreement is achieved for all cases. Figure 5.9 shows streamlines for $\varepsilon = 0.5$ and $N = 0.5$, whose structure can be seen to be similar to that in (Pilitsis and Beris, 1991). As expected, the streamfunction field is symmetric about the widest cross-section of the tube, i.e. $z = 1/2$.

For $Re > 0$, we consider the tube with ($\varepsilon = 0.16, N = 0.3$) and Re up to a value of 783. Table 5.3 reports $f\mathrm{Re}$ for a wide range of Re. Results obtained by the global spectral method (Lahbabi and Chang, 1986), and by the Galerkin finite element method (GFE) and FCC (Pilitsis and Beris, 1992) are also included for comparison purposes. The 1D-IRBFN results approach the FCC ones as the grid is refined. Furthermore, they are in better agreement with the FCC results than the GFE ones. Contour plots for the streamfunction and vorticity are

shown in Figure 5.10, which look feasible in comparison with those reported in (Lahbabi and Chang, 1986; Mai-Duy and Tanner, 2006). It can be seen that the flows are no longer symmetric. There appears a recirculation. As Re increases, its size grows and its centre moves towards the tube axis.

Oldroyd-B fluid

The Oldroyd-B model is implemented with $\alpha = 0.85$ that is widely used in the literature (e.g. Pilitsis and Beris, 1989). Like in (Pilitsis and Beris, 1989), we only consider creeping flows. Taking non-slip and symmetrical boundary conditions into account, the constitutive equations reduce to algebraic equations on the wall and to ODEs on the centreline, respectively. As a result, the stress equations on these boundary lines can be solved separately from the set of stress equations associated with the interior nodes. On the other hand, the value of u_z on the centreline can be obtained by means of L'Hospital's rule.

In this work, instead of considering ODEs, the values of T_{rr}, T_{zz} and $T_{\theta\theta}$ on the centreline are computed by directly employing 1D-IRBFNs (function interpolation). Those values are regarded as nodal unknowns and they can be found using the symmetric conditions. On each radial grid line z_i with $i = (2, \cdots, N_z - 1)$, through (5.35), one has

$$\frac{\partial T_{rr}(z_i, r=0)}{\partial r} = \sum_{j=1}^{N_r} \frac{\partial \varphi_j\,(r=0)}{\partial r} \left(T_{rr}\right)_{i,j} = 0, \tag{5.68}$$

$$\frac{\partial T_{zz}(z_i, r=0)}{\partial r} = \sum_{j=1}^{N_r} \frac{\partial \varphi_j\,(r=0)}{\partial r} \left(T_{zz}\right)_{i,j} = 0, \tag{5.69}$$

$$\frac{\partial T_{\theta\theta}(z_i, r=0)}{\partial r} = \sum_{j=1}^{N_r} \frac{\partial \varphi_j\,(r=0)}{\partial r} \left(T_{\theta\theta}\right)_{i,j} = 0. \tag{5.70}$$

Equations (5.68) - (5.70) need be solved in conjunction with the set of stress

equations associated with the interior nodes. The advantage of this approach is that one can avoid computing velocity derivatives in the constitutive equations on the centreline. We apply a coupled approach to handle the governing equations, in which the resultant nonlinear algebraic set is solved by means of Newton-based method (trust region techniques with the brief procedure given in Appendix B).

In the case of moderate corrugation amplitude and small wave length ($\varepsilon = 0.1$, $N = 0.5$), simulations are carried out with four grids of 11×11, 21×21, 31×31 and 41×41. The obtained results are shown in Figure 5.11 for velocity, Figure 5.12 and Figure 5.13 for stress, and Figure 5.14a for flow resistance. In Figure 5.11, the distribution of u_r at $We = 2$ is plotted showing the influence of the grid size. As the grid is refined, the smoothness of the computed field is improved and the maximum and minimum values of u_r remain unchanged. A grid density of 21×21 appears to be sufficient for computing u_r at $We = 2$. Figure 5.12 shows the behaviour of T_{rz} with increasing We. At high values of We, steep layers are formed in the area close to the wall. This behaviour can also be seen for T_{zz} as shown in Figure 5.13. In Figure 5.14a, the 1D-IRBFN solution is shown to converge up to $We = 6$ and the values of $f\mathrm{Re}$ are in good agreement with the benchmark solution (Pilitsis and Beris, 1992) (solutions in (Pilitsis and Beris, 1992) reported only for three values of We, namely 0, 1.2071 and 3.6213). Denser grids are required for higher-We solutions. It is noted that the two coarse grids, 11×11 and 21×21, fail to yield a convergent solution for high values of We.

In the case of moderate corrugation amplitude and moderate wave length ($\varepsilon = 0.1$, $N = 0.16$), three grids of 11×11, 21×21 and 31×31 are employed. The plot of $f\mathrm{Re}$ versus We is shown in Figure 5.14b. It can be seen that a convergent $f\mathrm{Re}$ solution is obtained up to $We = 7$ using 11×11, $We = 8$ using 21×21, and $We = 18$ using 31×31. Other remarks here are similar to those in the previous case ($\varepsilon = 0.1$, $N = 0.5$).

Table 5.2: Problem 3, Newtonian fluid: Comparison of the flow resistance $f\mathrm{Re}$ for $Re = 0$ computed for several values of ε and N

ε	0.1	0.1	0.2	0.286	0.3	0.5
N	0.5	0.1592	0.1042	0.2333	0.1592	0.5
	Present method					
21×21	17.71385	16.91518	19.75360	26.33921	26.40423	95.18132
41×41	17.73548	16.92656	19.76213	26.37003	26.42937	95.51616
61×61	17.74106	16.92760	19.76351	26.37759	26.43378	95.61778
SM [a]	17.7514	16.9290	19.7658	26.3724	26.437	95.6363
FCC [b]			19.765	26.383	26.437	
PSFD [c]			19.765	26.383	26.436	
PCFD [d]			19.761	26.377	26.432	

[a] Spectral method (Phillips and Owens, 1997)
[b] Fourier-Chebyshev Collocation (Pilitsis and Beris, 1991)
[c] Pseudospectral/finite difference method (Pilitsis and Beris, 1989)
[d] Modified PSFD in a stretched cylindrical coordinate (Pilitsis and Beris, 1989)

Table 5.3: Problem 3, Newtonian fluid, $\varepsilon = 0.3$, $N = 0.16$: comparison of the flow resistance $f\mathrm{Re}$ for a wide range of Re

	Re									
	0	12	22.6	51	73	132	207.4	264	387.2	783
	Present method									
21×21	26.49503	27.22021	28.59313	31.80464	33.48944	36.61126	39.04828	40.34471	42.48868	46.02994
31×31	26.47991	27.20798	28.57514	31.78472	33.46705	36.56876	39.00632	40.29224	42.40401	45.66516
41×41	26.46953	27.19921	28.56523	31.77200	33.45333	36.53881	38.99009	40.27630	42.38337	45.62292
51×51	26.46298	27.19314	28.55838	31.76329	33.44396	36.51618	38.97686	40.26089	42.37057	45.60680
2D IRBFN [a]	26.4445	27.1773	28.5535	31.7511	33.4538	36.5424	38.996	40.3044	42.4595	45.7402
GFE [b]	26.4193	27.0911	28.4433	31.6984	33.4039	36.5392	38.933	40.1544	42.1112	45.0734
FCC [c]	26.4484	27.1791	28.5536	31.7484	33.4488	36.5264	38.9607	40.2446	42.3479	45.5828

[a] 2D-Integated Radial basis function network (Mai-Duy and Tanner, 2006)
[b] Galerkin finite element method (Pilitsis and Beris, 1992)
[c] Fourier-Chebyshev Collocation (Pilitsis and Beris, 1992)

a) Geometry

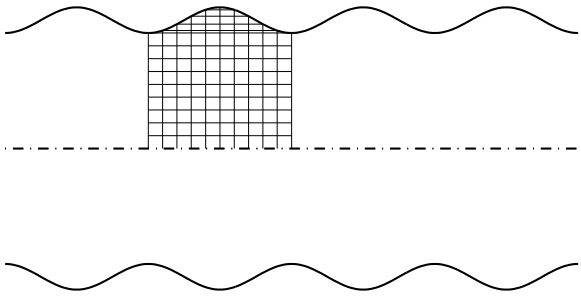

b) Reduced domain and discretisation

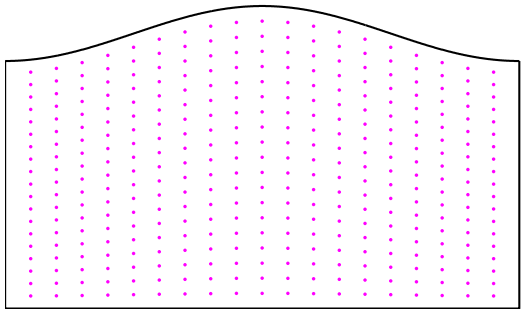

Figure 5.8: Problem 3: problem definition

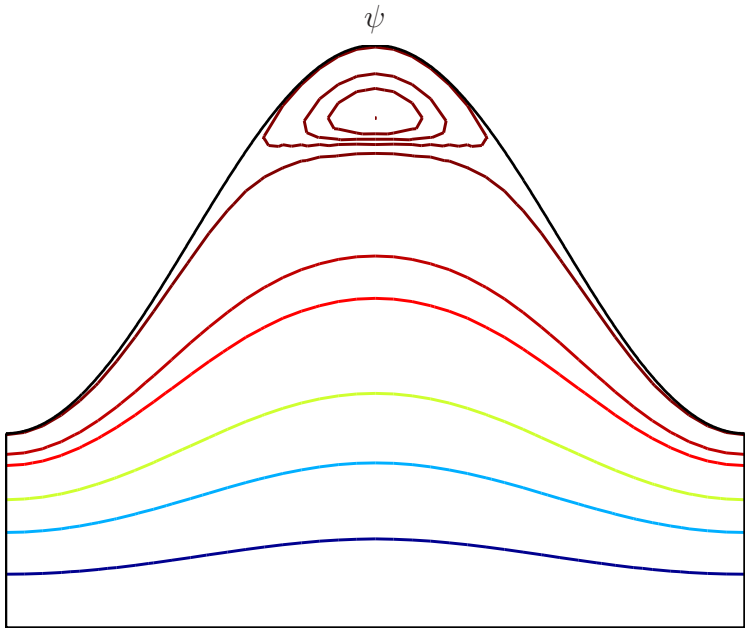

Figure 5.9: Problem 3, Newtonian fluid, $\varepsilon = 0.5$, $N = 0.5$, grid size of 41×41: Streamlines for $Re = 0$. Iso-values used are (0, 0.02, 0.06, 0.1, 0.14, 0.15, 0.159). For $0.159157 \leq \psi \leq 0.15933$, an increment of 5.767×10^{-5} is used to resolve the recirculation region, which are the same as those in (Pilitsis and Beris, 1991).

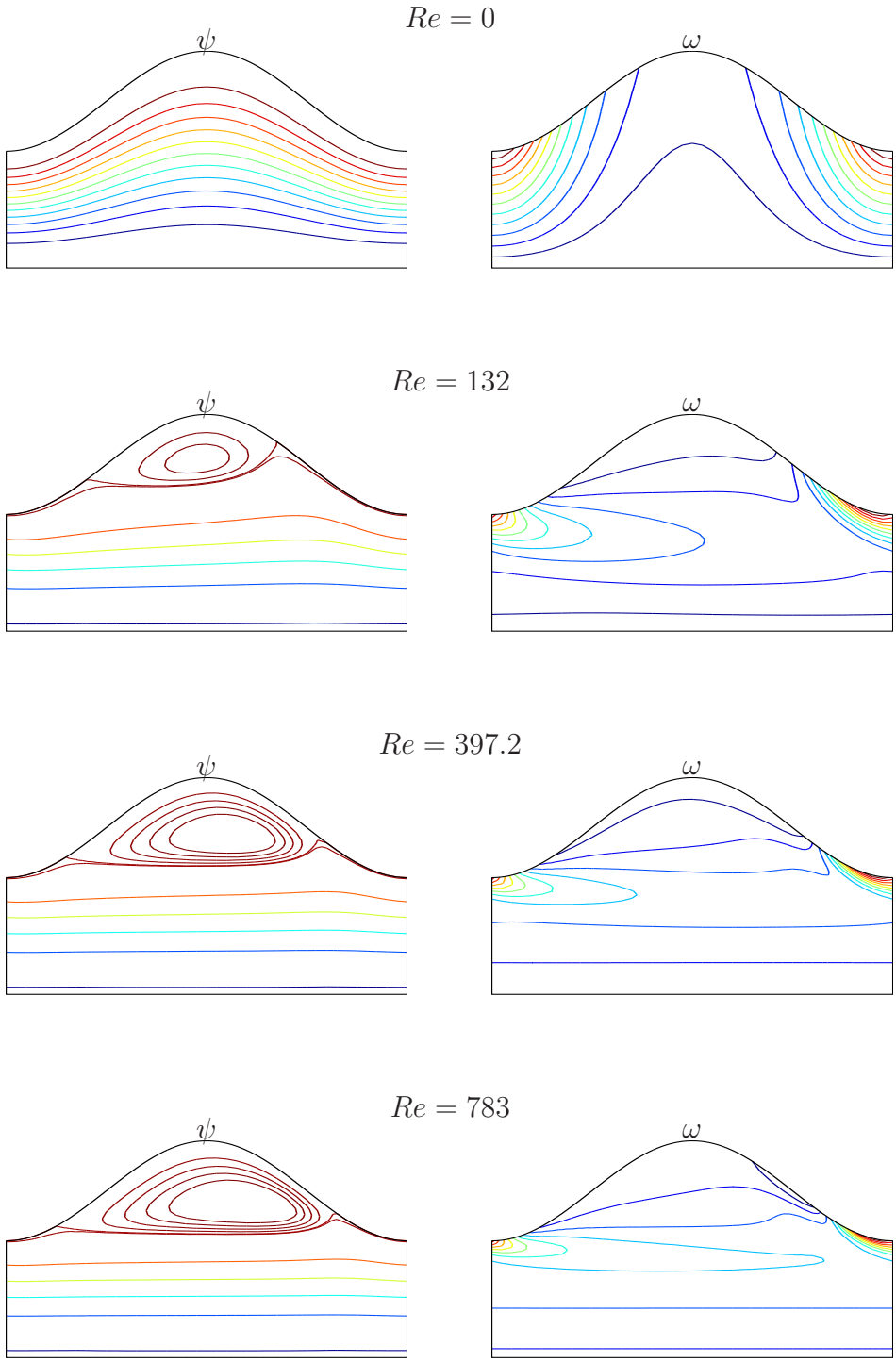

Figure 5.10: Problem 3, Newtonian fluid, $\varepsilon = 0.3$, $N = 0.16$, grid size of 41×41: Contour plots of the streamfunction and vorticity for a wide range of Re.

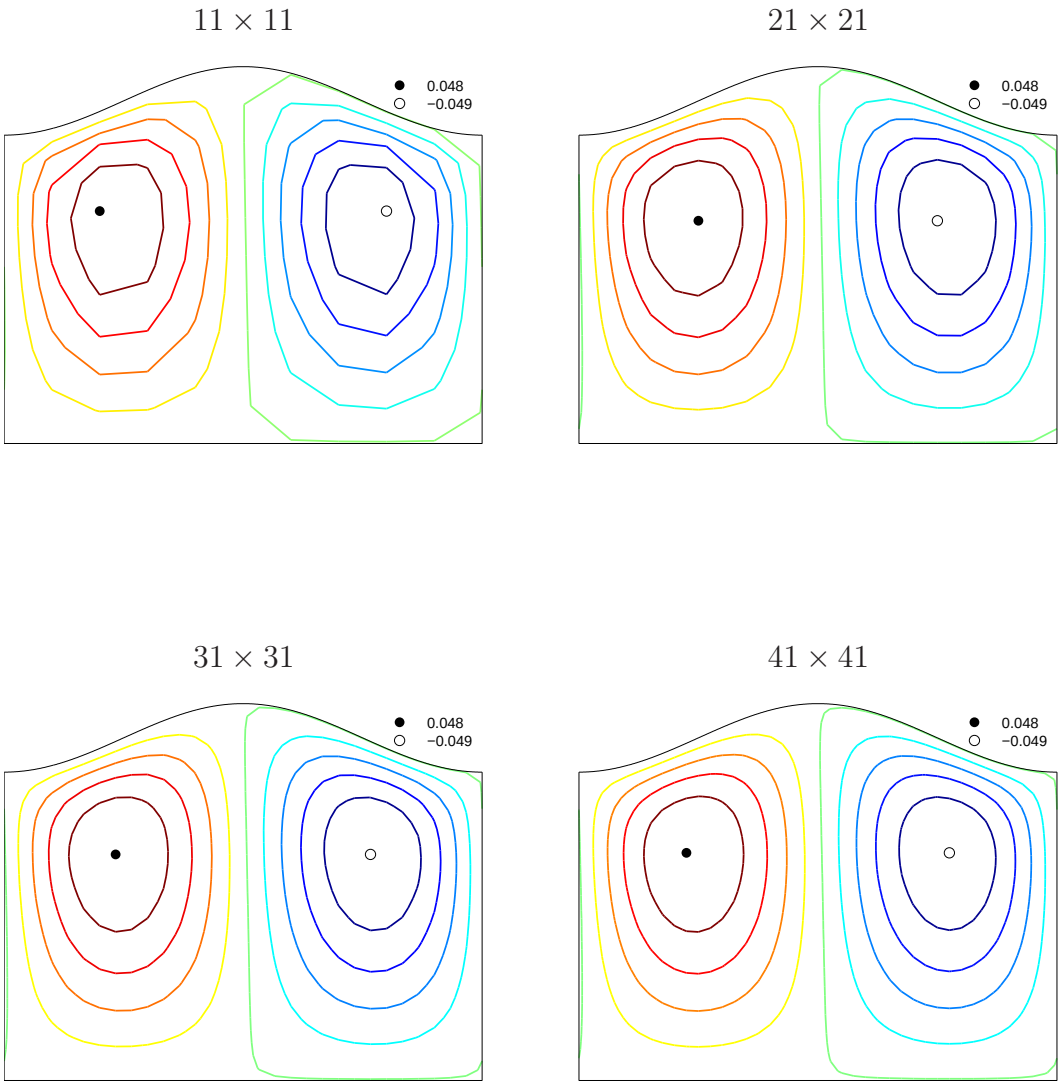

Figure 5.11: Problem 3, Oldroyd-B fluid, $\varepsilon = 0.1$, $N = 0.5$: Contour plots for u_r at $We = 2$ using several grids. The maximum and minimum values of u_r and their locations are also displayed.

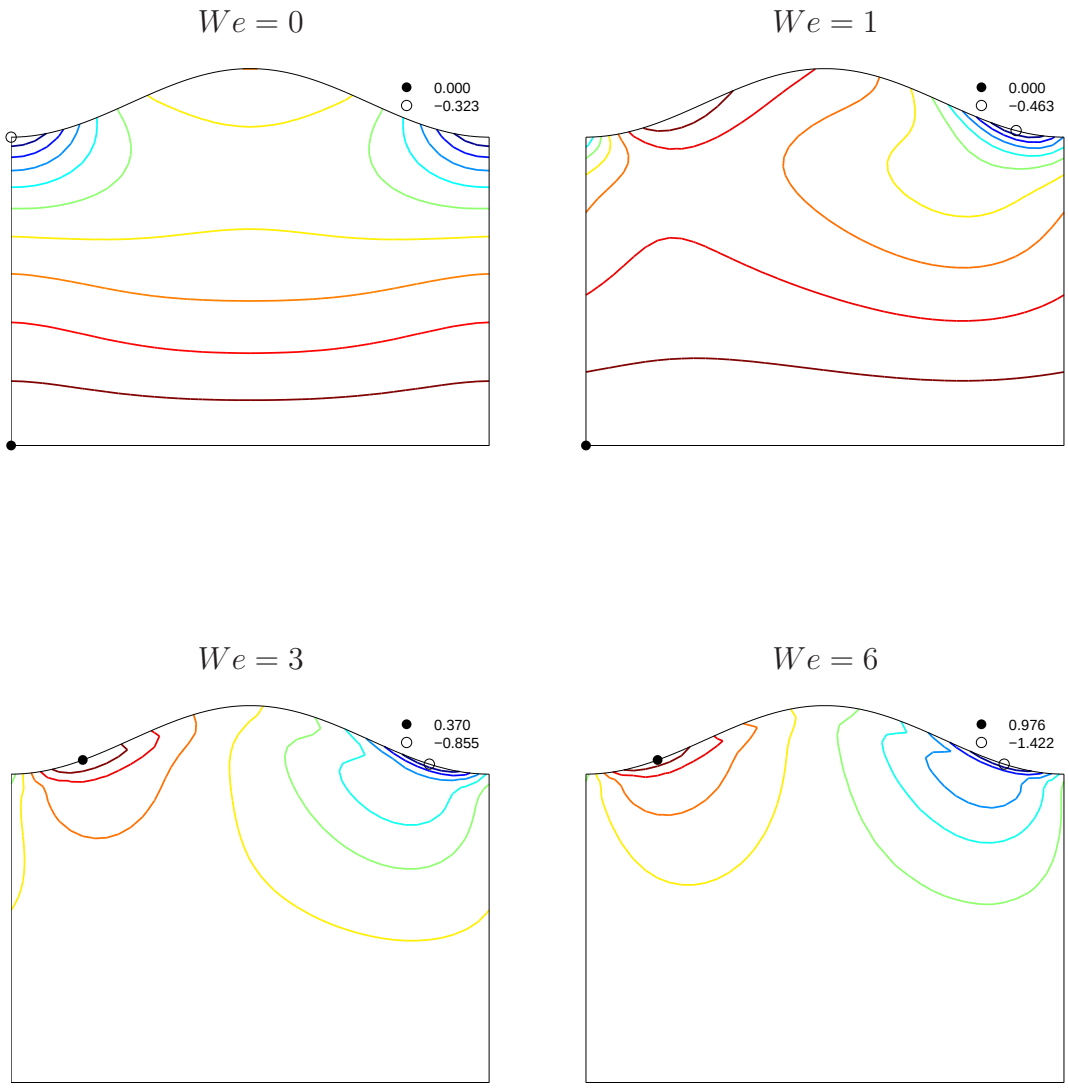

Figure 5.12: Problem 3, Oldroyd-B fluid, $\varepsilon = 0.1$, $N = 0.5$: Contour plots for T_{rz} at four values of We using a grid of 41×41. The maximum and minimum values of T_{rz} and their locations are also displayed.

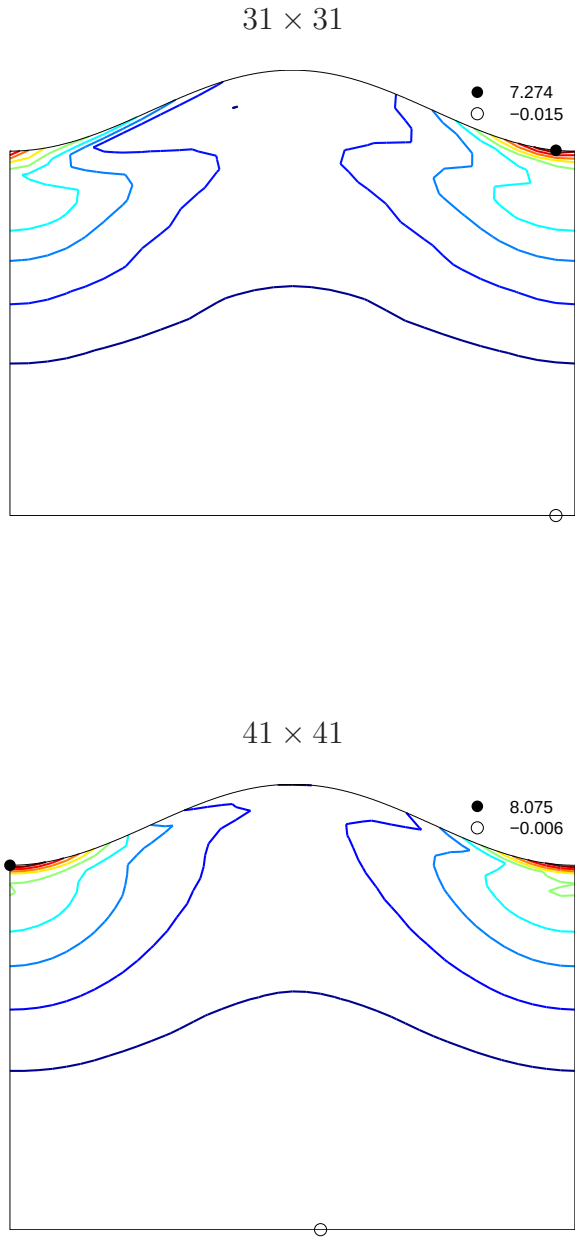

Figure 5.13: Problem 3, Oldroyd-B fluid, $\varepsilon = 0.1$, $N = 0.5$: Contour plots for T_{zz} at $We = 6$ using grids of 31×31 and 41×41. The maximum and minimum values of T_{zz} and their locations are also displayed.

a) $\varepsilon = 0.1$, $N = 0.5$

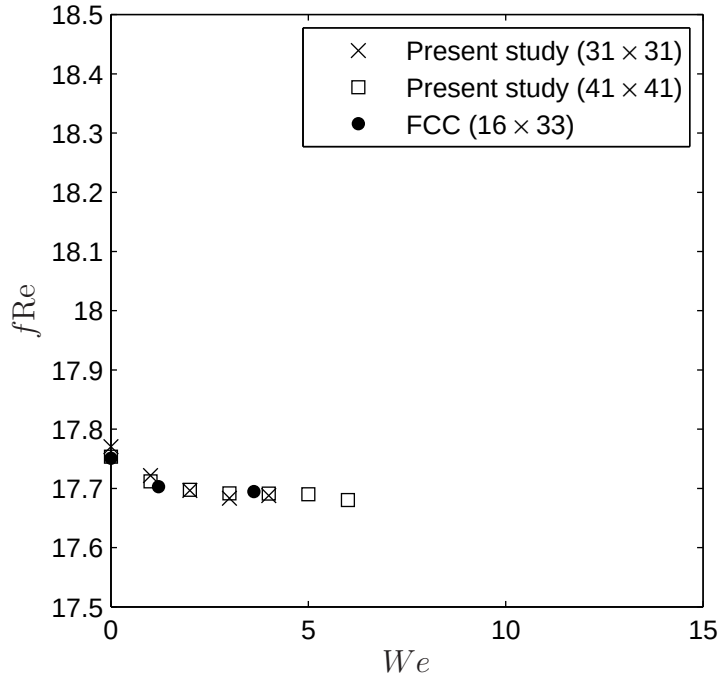

b) $\varepsilon = 0.1$, $N = 0.16$

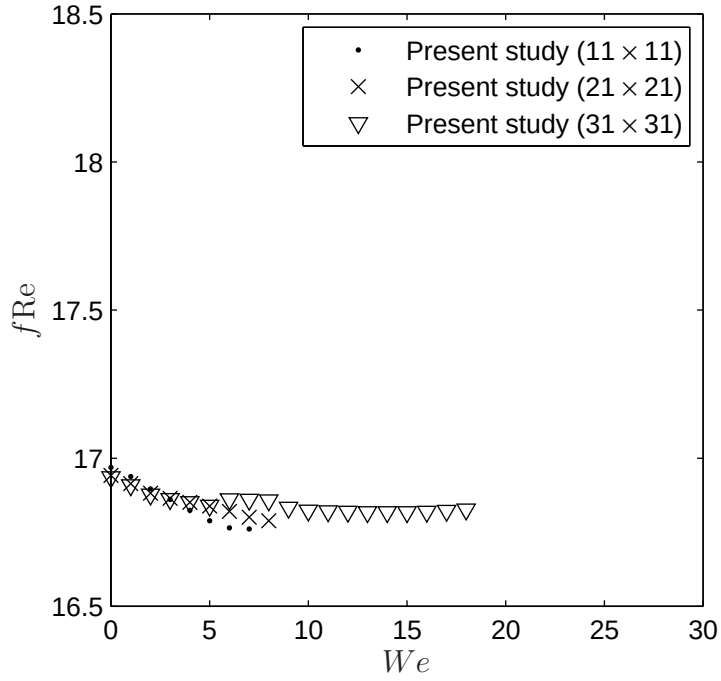

Figure 5.14: Problem 3, Oldroyd-B fluid: The variation of the flow resistance with respect to the Weissenberg number for two geometrical configurations.

5.5 Concluding remarks

In this chapter, viscoelastic flows in rectangular ducts and in straight and corrugated tubes are simulated with 1D-IRBFN-based Galerkin/Collocation techniques. Instead of using low-order polynomials, the trial functions in the Galerkin and point-collocation formulations are presently implemented with 1D-IRBFNs. Boundary treatments especially for those on the centreline using 1D-IRBFNs are discussed in detail. The 1D-IRBFN results, which are obtained for a wide range of the Weissenberg number, are in good agreement with the exact/numerical solutions available in the literature.

Chapter 6

Conclusions

This thesis reports attempts to develop numerical methods based on 1D-IRBFNs for the simulation of Newtonian and non-Newtonian fluid flows. Main features of the methods include (i) the field variables are represented by high-order approximators in one dimension (i.e. 1D-IRBFNs); (ii) the governing equations are discretised by means of Galerkin and point-collocation formulations; and (iii) double and Neumann boundary conditions are imposed with the help of the integration constants. It was found numerically from function interpolation that (i) equally-spaced grids can be used with 1D-IRBFNs without suffering from Runge's phenomenon; and (ii) the constants of integration arising from the construction of 1D-IRBFNs provide an effective means to utilise all available information in certain cases, for example, where both function and derivative values are given at a point. These properties of 1D-IRBFNs were then exploited successfully for the solution of PDEs by (i) generating the trial and test functions on uniform spaces for the Galerkin formulation; (ii) imposing double boundary conditions for the streamfunction formulation; and (iii) deriving a computational boundary condition for the vorticity.

In Chapters 3 and 4, we have presented a 1D-IRBFN-based Galerkin method for the simulation of flows of a Newtonian fluid. For the streamfunction-vorticity-

temperature formulation (Chapter 3), a new way to derive a computational boundary condition for the vorticity was proposed. This boundary vorticity scheme is global and has a strong influence on the overall accuracy of the approximate solution. For the streamfunction formulation (Chapter 4), two well-known issues, which numerical methods have to confront, were addressed. The first lies in the representation of high-order derivatives. Integration rather than differentiation is employed here to construct the approximations, which helps avoid the reduction in convergence rate caused by differentiation. The second lies in the imposition of double boundary conditions. Derivative boundary conditions are implemented in an exact manner through the process of converting the RBF space into the physical space. As a result, there is no need to introduce fictitious points or to reduce the number of nodes used for collocating the PDE. Results obtained showed that the 1D-IRBFN-based Galerkin method achieves a high rate of convergence with respect to the number of RBFs for linear problems and produces accurate solutions using relatively-low data densities for highly nonlinear flows. It is noted that the work presented in Section 3.4.2 appears to be one of the earliest RBF reports which have successfully simulated the thermally-driven flow in a square slot at the Rayleigh number of 10^8.

In Chapter 5, we have presented Galerkin/collocation methods for the simulation of viscoelastic flows. The trial functions in the Galerkin and point-collocation formulations were implemented with 1D-IRBFNs. Stress boundary conditions on the centreline are computed by directly employing 1D-IRBFNs. Viscoelastic flows in straight tubes with non-circular and circular cross-sections were considered. For the former, flows of CEF fluids in rectangular ducts were simulated, demonstrating the capability of the method to capture secondary circulations of relatively low strength. In the latter, flows of Oldroyd-B fluids in corrugated tubes were simulated, showing the capability of the method to handle fluids modelled by hyperbolic PDEs.

These achievements indicate that 1D-IRBFN-based Galerkin and point-collocation

methods are useful tools in CFD. In the future, the following works are suggested for improvement and enhancement of the methods

- *Extension of the 1D-IRBFN-based Galerkin method to flows in irregular geometries*

  Tensor products are presently employed to construct the approximations over the whole domain from 1D-IRBFNs defined on grid lines. It is possible to implement hybrid 1D-IRBFN schemes, where point-collocation formulation is used for subregions containing irregular geometries and Galerkin formulation is employed for the remaining subregions of the problem domain. It is noted that the 1D-IRBFN-based point-collocation method is applicable to flows in irregular geometries.

- *Validation of the methods with other constitutive models*

  The present methods are presently validated with Newtonian, CEF and Oldroyld-B models. It is possible to replace these models with other non-ideal fluids occurring in industries for further applications.

- *Implementation of the constitutive equations at higher values of the Weissenberg number in their matrix logarithm forms*

  It has been recently discovered that the transformation of the constitutive equations into matrix logarithm forms is capable of resolving the well-known high Weissenberg number problem (Fattal and Kupferman, 2004, 2005). This breakthrough is made, owing to the facts that (i) the corresponding stress tensor is now guaranteed to be positive definite; and (ii) steep boundary layers where the variations of stresses grow exponentially can be captured more accurately. It is possible to incorporate such logarithm forms into the present methods to produce a converged solution at higher values of the Weissenberg number.

Appendix A

Antiderivatives of multiquadric function in one dimension

This appendix provides analytical expressions for antiderivatives of the multiquadric (MQ) function in one dimension. Let η, c, a be the coordinate, the MQ's centre and the MQ's width/shape-parameter, respectively. The MQ function is defined as

$$g(\eta) = \sqrt{(\eta - c)^2 + a^2}. \tag{A.1}$$

Antiderivatives of (A.1), which are employed in this thesis, are given below.

$$\int g(\eta) d\eta = \frac{1}{2}(\eta - c)\sqrt{(\eta - c)^2 + a^2} + \frac{1}{2}a^2 \ln\left((\eta - c) + \sqrt{(\eta - c)^2 + a^2}\right), \tag{A.2}$$

$$\begin{aligned}\iint g(\eta) d\eta = &\left(\frac{1}{6}(\eta - c)^2 - \frac{1}{3}a^2\right)\sqrt{(\eta - c)^2 + a^2} \\ &+ \frac{1}{2}a^2\sqrt{(\eta - c)^2 + a^2}\ln\left((\eta - c) + \sqrt{(\eta - c)^2 + a^2}\right),\end{aligned} \tag{A.3}$$

$$\iint g(\eta)d\eta = \left(\frac{1}{24}(\eta-c)^2 - \frac{13}{48}(\eta-c)a^2\right)\sqrt{(\eta-c)^2+a^2} - \frac{1}{16}a^4 n\left((\eta-c)+\sqrt{(\eta-c)^2+a^2}\right) + \frac{1}{4}a^2(\eta-c)^2\ln\left((\eta-c)+\sqrt{(\eta-c)^2+a^2}\right), \tag{A.4}$$

$$\iiint g(\eta)d\eta = \left(\frac{1}{120}(\eta-c)^4 - \frac{83}{720}(\eta-c)^2a^2 + \frac{1}{45}a^4\right)\sqrt{(\eta-c)^2+a^2} + \frac{1}{48}a^2(\eta-c)^2\left(4(\eta-c)^2-3a^2\right)\ln\left((\eta-c)+\sqrt{(\eta-c)^2+a^2}\right). \tag{A.5}$$

Appendix B

Iterative methods for nonlinear equations

This appendix gives a brief review of iterative methods for solving a set of nonlinear equations in the form of

$$\mathbf{K}(\mathbf{u})\mathbf{u} = \mathbf{F}(\mathbf{u}), \tag{B.1}$$

and

$$\mathbf{M}\dot{\mathbf{u}} + \mathbf{K}(\mathbf{u})\mathbf{u} = \mathbf{F}(\mathbf{u}), \tag{B.2}$$

where $\mathbf{M}$ and $\mathbf{K}$ are matrices; $\dot{\mathbf{u}}$, $\mathbf{u}$ and $\mathbf{F}$ vectors; $\mathbf{u}$ is the unknown vector to be found; and a superposed dot on $\mathbf{u}$ denotes a derivative with time ($\dot{u} = \partial u/\partial t$). It is noted that (B.1)/(B.2) is written in a general form to which any nonlinear system can be transformed by appropriately defining $\mathbf{M}$, $\mathbf{K}$ and $\mathbf{F}$.

B.1 Picard methods

Picard methods are used for solving (B.1) which arises from Chapters 4 and 5. The Picard algorithm can be simply described as

$$\mathbf{K}(\mathbf{u}^{(n)})\mathbf{u}^{(n+1)} = \mathbf{F}(\mathbf{u}^{(n)}), \tag{B.3}$$

where the superscript (.) indicates the iteration number. To obtain a converged solution, $\mathbf{u}^{(n+1)}$ usually needs be relaxed according to the following relation

$$\mathbf{u}^{(n+1)} = \gamma\mathbf{u}^{(n)} + (1-\gamma)\mathbf{u}^{(n+1)}, \tag{B.4}$$

where $0 < \gamma < 1$.

B.2 Newton-based methods

Newton-based methods are used for solving (B.1) which arises from Chapter 5. Equation (B.1) can be rewritten as

$$\mathbf{R}(\mathbf{u}) = \mathbf{K}(\mathbf{u})\mathbf{u} - \mathbf{F}(\mathbf{u}) = \mathbf{0}. \tag{B.5}$$

Instead of finding a solution to (B.1), Newton-based methods try to find the roots of the function $\mathbf{R}(\mathbf{u})$. Expanding $\mathbf{R}(\mathbf{u})$ in a Taylor series and then discarding high-order terms, one obtains

$$\mathbf{R}\left(\mathbf{u}^{(n)}\right) = -\left.\frac{\partial \mathbf{R}}{\partial \mathbf{u}}\right|_{\mathbf{u}^{(n)}} \left(\mathbf{u}^{(n+1)} - \mathbf{u}^{(n)}\right) \equiv -\mathcal{J}\left(\mathbf{u}^{(n)}\right)\left(\mathbf{u}^{(n+1)} - \mathbf{u}^{(n)}\right), \tag{B.6}$$

where $\mathcal{J}$ is the Jacobian matrix. Solving (B.6) for $\mathbf{u}^{(n+1)}$, we have

$$\mathbf{u}^{(n+1)} = \mathbf{u}^{(n)} - \mathcal{J}^{-1}\mathbf{R}\left(\mathbf{u}^{(n)}\right). \tag{B.7}$$

To avoid computing the inverse of $\mathcal{J}$, one can apply trust region techniques

$$\mathbf{u}^{(n+1)} = \mathbf{u}^{(n)} + \mathbf{d}^{(n)}, \tag{B.8}$$

where $\mathbf{d}^{(n)}$ is computed at every iteration through the following optimisation subproblem

$$\min_{\mathbf{d}} \left\| \mathbf{R}\left(\mathbf{u}^{(n)}\right) + \mathcal{J}\left(\mathbf{u}^{(n)}\right)\mathbf{d}^{(n)} \right\|^2, \qquad \text{such that} \qquad \left\|\mathbf{d}^{(n)}\right\| \leq \Delta^{(n)}, \tag{B.9}$$

where $\Delta^{(n)} > 0$ is the trust region radius. To decide whether the trial $\mathbf{d}^{(n)}$ is acceptable, the techniques use the following parameter

$$r^{(n)} = \frac{\left\|\mathbf{R}\left(\mathbf{u}^{(n)}\right)\right\|^2 - \left\|\mathbf{R}\left(\mathbf{u}^{(n)} + \mathbf{d}^{(n)}\right)\right\|^2}{\left\|\mathbf{R}\left(\mathbf{u}^{(n)}\right)\right\|^2 - \left\|\mathbf{R}\left(\mathbf{u}^{(n)}\right) + \mathcal{J}\left(\mathbf{u}^{(n)}\right)\mathbf{d}^{(n)}\right\|^2}. \tag{B.10}$$

- if $r^{(n)} \geq c_0$ with $0 \leq c_0 < 1$, set $\mathbf{u}^{(n+1)} = \mathbf{u}^{(n)} + \mathbf{d}^{(n)}$.
- otherwise, set $\mathbf{u}^{(n+1)} = \mathbf{u}^{(n)}$, reduce the trust region radius $\Delta^{(n)}$, and resolve (B.9).

B.3 Time-marching methods

Time-marching methods are used for solving (B.2) which arises from Chapter 3. The forward Euler (or semi-implicit) scheme is applied in this thesis. Its algorithm can be described as

$$\mathbf{M}\mathbf{u}^{(n+1)} = \mathbf{M}\mathbf{u}^{(n)} + \triangle t \left(\mathbf{F}(\mathbf{u}^{(n)}) - \mathbf{K}(\mathbf{u}^{(n)})\mathbf{u}^{(n+1)}\right), \tag{B.11}$$

where $\triangle t = t^{(n+1)} - t^{(n)}$ is the time step.

Equation (B.11) can be rewritten in the form which is more suitable for computation,

$$\left(\frac{1}{\triangle t}\mathbf{M} + \mathbf{K}(\mathbf{u}^{(n)})\right)\mathbf{u}^{(n+1)} = \frac{1}{\triangle t}\mathbf{M}\mathbf{u}^{(n)} + \mathbf{F}(\mathbf{u}^{(n)}). \tag{B.12}$$

References

Araujo, B. J., Teixeira, J. C. F., Cunha, A. M. and Groth, C. P. T. (2009). Paralel three-dimensional simulation of the injection molding process, *International Journal for Numerical Methods in Fluids* **59**: 801–815.

Atluri, S. N., Han, Z. D. and Rajendran, A. M. (2004). A New Implementation of the Meshless Finite Volume Method, Through the MLPG "Mixed" Approach, *CMES: Computer Modeling in Engineering & Sciences* **6 (6)**: 491–514.

Atluri, S. N., Han, Z. D. and Shen, S. (2003). Meshless Local Petrov-Galerkin (MLPG) Approaches for Solving the Weakly-Singular Traction & Displacement Boundary Integral Equations, *CMES: Computer Modeling in Engineering & Sciences* **4 (5)**: 507–518.

Atluri, S. and Zhu, T. (1998). A new meshless local Petrov-Galerkin (MLPG) approach to nonlinear problems in computational modeling and simulation, *Modeling Simulation in Engineering* **3**: 187–196.

Belytschko, T., Krongauz, Y., Organ, D., Fleming, M. and Krysl, P. (1996). Meshless method: an overview and recent developments, *Computer Methods in Applied Mechanics and Engineering* **139**: 3–47.

Belytschko, T., Lu, Y. Y. and Gu, L. (1994). Element-Free Galerkin Methods, *International Journal for Numerical Methods in Engineering* **37**: 229–256.

Boyd, J. P. (2010). Six strategies for defeating the Runge Phenomenon in Gaus-

sian radial basis functions on a finite interval star, *Computers & Mathematics with Applications* **60 (12)**: 3108–3122.

Brebbia, C. A., Telles, J. C. F. and Wrobel, L. C. (1984). *Boundary Element Techniques: Theory and Applications in Engineering* , Spring-Verlag Berlin, Heidelberg.

Buhmann, M. and Dyn, N. (1993). Spectral converence of multiquadric interpolation, *Proceedings of the Edinburgh Mathematical Society* **36**: 319–333.

Burdette, S. R., Coates, P. J., Armstrong, R. C. and Brown, R. A. (1989). Calculations of viscoelastic flow through an axisymmetric corrugated tube using the explicitly elliptic momentum equation formulation (EEME), *Journal of Non-Newtonian Fluid Mechanics* **33**: 1–23.

Canuto, C., Hussaini, M., Quarteroni, A. and Zang, T. A. (1988). *Spectral Methods in Fluid Dynamics*, New York, Springer-Verlag.

Chang, R. Y. and Yang, W. H. (2001). Numerical simulation of mold filling in injection molding using a three-dimensional finite volume approach, *International Journal for Numerical Methods in Fluids* **37**: 125–148.

Cheng, A. H. D., Golberg, M. A. and Zammito, E. J. K. G. (2003). Exponential Convergence and H-c Multiquadric Collocation Method for Partial Differential Equations, *Numerical Methods for Partial Differential Equations* **19 (5)**: 571–594.

Cover, T. M. (1965). Geometrical and Statistical Properties of Systems of Linear Inequalities with Applications in Pattern Recognition, *IEEE Transactions on In Electronic Computers* **EC-14 (3)**: 326–334.

Criminale, W. O. J., Ericksen, J. L. and Filbey, G. L. J. (1957). Steady shear flow of non-Newtonian Fluids, *Archive for Rational Mechanics and Analysis* **1(1)**: 410–417.

Crochet, M. J. (1989). Numerical simulation of viscoelastic flow: A review, *Rubber Chemistry and Technology* **62**: 426–455.

Crochet, M. J., Davies, A. R. and Walters, K. (1984). *Numerical simulation of non-Newtonian flow*, Elsevier Science Publishers.

Crochet, M. J. and Walters, K. (1983). Numerical methods in non-Newtonian fluid mechanics, *Annual Review of Fluid Mechanics* **15**: 241–260.

Davis, G. D. V. (1983). Natural convection of air in a square cavity: a bench mark numerical solution, *International Journal of Numerical Method Fluids* **3**: 249–264.

Divo, E. and Kassab, A. J. (2005). A meshless method for conjugate heat tranfer problems, *Engineering Analysis with Boundary Elements* **29**: 136–149.

Divo, E. and Kassab, A. J. (2006). Iterative domain decomposition meshless method modeling of incompressible viscous flows and conjugate heat transfer, *Engineering Analysis with Boundary Elements* **30 (6)**: 465–478.

Divo, E. and Kassab, A. J. (2007). An Efficient Localized Radial Basis Function Meshless Method for Fluid Flow and Conjugate Heat Transfer, *Journal of Heat Transfer* **129 (2)**: 124–136.

Divo, E. and Kassab, A. J. (2008). Localized Meshless Modeling of Natural-Convective Viscous Flows, *Numerical Heat Transfer, Part B: Fundamentals* **53 (6)**: 487–509.

El-Zahab, Z., Divo, E. and Kassab, A. J. (2009). A localized collocation meshless method (LCMM) for incompressible flows CFD modeling with applications to transient hemodynamics, *Engineering Analysis with Boundary Elements* **33 (8–9)**: 1045–1061.

Ellero, M. and Tanner, R. I. (2005). SPH simulations of transient viscoelastic flows at low Reynoyd number, *Journal of Non-Newtonian Fluid Mechanic* **132**: 61–72.

Erhart, K., Divo, E. and Kassab, A. J. (2008). An evolutionary-based inverse approach for the identification of non-linear heat generation rates in living tissues using a localized meshless method, *International Journal of Numerical Methods for Heat & Fluid Flow* **18 (3/4)**: 401–414.

Fasshauer, G. (2007). *Meshfree approximation methods with Matlab*, World Scientific Publishing.

Fattal, R. and Kupferman, R. (2004). Constitutive laws for the matrix-logarithm of the conformation tensor, *Journal of Non-Newtonian Fluid Mechanics* **123**: 281–285.

Fattal, R. and Kupferman, R. (2005). Time-dependent simulation of viscoelastic flows at high Weissenberg number using the log-conformation representation, *Journal of non-Newtonian Fluid Mechanics* **126**: 23–37.

Fornberg, B., Flyer, N. and Russell, J. M. (2010). Comparisons between pseudospectral and radial basis function derivative approximations, *IMA Journal of Numerical Analysis* **30 (1)**: 149–172.

Fornberg, B. and Zuev, J. (2007). The Runge Phenomenon and spatially variable shape parameters in RBF interpolation, *Computers and Mathematics with Applications* **54**: 379–398.

Franke, C. and Schaback, R. (1998). Convergence order estimates of meshless collocation methods using radial basis functions, *Advances in Computational Mathematics* **8**: 381–399.

Franke, R. (1982). Scattered data interpolation: tests of some methods, *Mathematics of Computation* **38**: 181–200.

Gervang, B. and Larsen, P. (1991). Secondary flows in straight ducts of rectangular cross section, *Journal of Non-Newtonian Fluid Mechanics* **39**: 217–237.

Green, G. E. and Rivlin, R. S. (1956). Steady flow of non-Newtonian fluids through tubes, *Quaterfly of Applied Mathematics* **14**: 299–308.

Haykin, S. (1999). *Neural networks - A comprehensive foundation*, Prentice Hall.

Ho-Minh, D., Mai-Duy, N. and Tran-Cong, T. (2009). A Galerkin-RBF approach for the streamfunction-vorticity-temperature formulation of natural convection in 2D enclosured domains, *CMES: Computer Modeling in Engineering & Sciences* **44**: 219–248.

Huerta, A., Vidal, Y. and Villon, P. (2004). Pseudo-divergence-free element free Galerkin method for incompressible fluid flow, *Computer Methods in Applied Mechanics and Engineering* **193 (12-14)**: 1119–1136.

Kansa, E. J. (1990a). Multiquadrics - A scattered data approximation scheme with applications to computational fluid dynamics I. Surface approximations and partial derivative estimates, *Computers and Mathematics with Applications* **19**: 127–145.

Kansa, E. J. (1990b). Multiquadrics-A scattered data approximation scheme with applications to computational fluid-dynamics-II solutions to parabolic, hyperbolic and elliptic partial differential equations, *Computers and Mathematics with Applications* **19 (8-9)**: 147–161.

Kosec, G. and Šarler, B. (2007). Solution of thermo-fluid problems by collocation with local pressure correction, *International Journal of Numerical Methods for Heat and Fluid Flow* **18**: 868–882.

Kosec, G. and Šarler, B. (2008). Local RBF CollocationMethod for Darcy Flow, *CMES: Computer Modeling in Engineering & Sciences* **25 (3)**: 197–207.

Kovačvić, I. and Šarler, B. (2005). Solution of a phase-field model for dissolution of primary particles in binary aluminum alloys by an r-adaptive mesh-free method, *Materials Science and Engineering: A* **413-414**: 423–428.

Kuehn, T. H. and Glodstein, R. J. (1976). An experimental and theoretical study of natural convection in the annulus between horizontal concentric cylinders, *Journal of Fluids Mechanics* **74**: 695–719.

Lahbabi, A. and Chang, H. C. (1986). Flow in periodically constricted tubes: Transition to inertial and nonsteady flows, *Chemical Engineering Science* **41 (10)**: 2487–2505.

Larson, E. and Fornberg, B. (2003). A numerical study of some radial basis function based solution methods for elliptic PDEs, *Computers and Mathematics with Applications* **46**: 891–902.

Le-Cao, K., Mai-Duy, N. and Tran-Cong, T. (2009). An Effective Integrated-RBFN Cartesian-Grid Discretization for the Stream Function-Vorticity-Temperature Formulation in Nonrectangular Domains, *Numerical Heat Transfer, Part B: Fundamentals* **55 (6)**: 480 – 502.

Le, P. B. H., Mai-Duy, N., Tran-Cong, T. and Baker, G. (2010). A Cartesian-grid collocation technique with integrated radial basis functions for mixed boundary value problems, *International Journal for Numerical Methods in Engineering* **82 (4)**: 403–536.

Lee, C. K., Liu, X. and Fan, S. C. (2003). Local multiquadric approximation for solving boundary value problems, *Computational Mechanics* **30**: 396–409.

Li, J., Cheng, A. H. D. and Chen, C. (2003). A comparison of efficiency and error convergence of multiquadric collocation method and finite element method, *Engineering Analysis with Boundary Elements* **27**: 251–257.

Li, J. and Hon, Y. C. (2004). Domain decomposition for radial basis meshless methods, *Numerical Methods for Partial Differential Equations* **20 (3)**: 450–462.

Ling, L. and Kansa, E. J. (2004). Aleast-squares preconditioner for radial basis functions collocation methods, *Advances in Computational Mathematics* **23**: 31–54.

Ling, L. and Kansa, E. J. (2005). A least-squares preconditioner for radial basis functions collocation methods, *Advances in Computational Mathematics* **23**: 31–54.

Ling, L. and Trummer, M. R. (2004). Multiquadric Collocation Method with Integral Formulation for Boundary Layer Problems, *Computers and Mathematics with Applications* **48**: 927–941.

Liu, G. R. and Gu, Y. T. (2005). *An Introduction to meshfree methods and their programming*, Springer, Netherlands.

Liu, W. K., Jun, S. and Zhang, Y. (1995). Reproducing kernel particle methods, *International Journal for numerical Methods in Fluids* **20**: 1081–1106.

Madych, W. R. and Nelson, S. A. (1988). Multivariate interpolation and conditionally positive definite functions, *Approximation Theory and its Applications* **4**: 77–89.

Mai-Duy, N. (2001). *Mesh-free radial basis function networks methods for some problems in continuum mechanics*, PhD thesis, University of Southern Queensland, Australia.

Mai-Duy, N., Ho-Minh, D. and Tran-Cong, T. (2009). A Galerkin approach incorporating integrated radial basis function networks for the solution of biharmonic equations in two dimensions, *International Journal of Computer Mathematics* **86 (10-11)**: 1746–1759.

Mai-Duy, N., Mai-Cao, L. and Tran-Cong, T. (2007). Computation of transient viscous flows using indirect radial basis function networks, *CMES: Computer Modeling in Engineering & Sciences* **18**: 59–77.

Mai-Duy, N. and Tanner, R. I. (2006). Computing non-Newtonian fluid flow with radial basis function networks, *International Journal for Numerical Methods in Fluids* **48**: 1309–1336.

Mai-Duy, N. and Tran-Cong, T. (2001a). Numerical solution of differential equations using multiquadric radial basis function networks, *Neural Networks* **14**: 185–199.

Mai-Duy, N. and Tran-Cong, T. (2001b). Numerical solution of Navier-Stokes equations using multiquadric radial basis function networks, *International Journal for Numerical Methods in Fluids* **37 (1)**: 65–86.

Mai-Duy, N. and Tran-Cong, T. (2003). Approximation of function and its derivatives using radial basis function network methods, *Applied Mathematical Modelling* **27**: 197–220.

Mai-Duy, N. and Tran-Cong, T. (2005). An efficient indirect RBFN-based method for numerical solution of PDEs, *Numerical Methods for Partial Differetial Equa- tions* **21**: 770–790.

Mai-Duy, N. and Tran-Cong, T. (2007). A Cartesian-grid collocation method based on radial basis function networks for solving PDEs in irregular domains, *Numerical Methods for Partial Differential Equations* **23**: 1192–1210.

Mai-Duy, N. and Tran-Cong, T. (2009a). A Cartesian-Grid Discretisation Scheme Based on Local Integrated RBFNs for Two-Dimensional Elliptic Problems, *CMES: Computer Modeling in Engineering & Sciences* **51 (3)**: 213–238.

Mai-Duy, N. and Tran-Cong, T. (2009b). A Numerical Study of 2D Integrated RBFNs Incorporating Cartesian Grids for Solving 2D Elliptic Differential Problems, *Numerical Methods for Partial Differential Equations* **26 (6)**: 1443–1462.

Mai-Duy, N. and Tran-Cong, T. (2009c). An integrated-RBF technique based on Galerkin formulation for elliptic differential equation, *Engineering Analysis with Boundary Elements* **33**: 191–199.

Manzari, M. T. (1999). An explicit finite element algorithm for convective heat transfer problems, *International Journal of Numerical Methods for Heat and Fluid Flow* **9**: 860–877.

Mayne, D. A., Usmani, A. S. and Crapper, M. (2000). h-Adaptive finite element solution of high Rayleigh number thermally driven cavity problem, *International Journal of Numerical Methods for Heat and Fluid Flow* **10**: 598–615.

Mayne, D. A., Usmani, A. S. and Crapper, M. (2001). h-Adaptive finite element solution of unsteady thermally driven cavity problem, *International Journal of Numerical Methods for Heat and Fluid Flow* **11**: 172–194.

Micchelli, C. (1986). Interpolation of scattered data: Distance matrices and conditionally positive definite functions, *Constructive Approximation* **2**: 11–22.

Momeni-Masuleh, S. H. and Phillips, T. N. (2004). Viscoelastic flow in an undulating tube using spectral methods, *Computers & Fluids* **33**: 1075–1095.

Monaghan, J. J. (1990). Smoothed particle hydrodynamics, *Annual review of astronomy and astrophysics* **30**: 543–574.

Monaghan, J. J. (1994). Simulating free surface flows with SPH, *Journal of Computational Physics* **110**: 399–406.

Owens, R. G. and Phillips, T. N. (2002). *Computational Rheology*, Imperial College Press.

Phillips, T. N. and Owens, R. G. (1997). A mass conserving multi-domain spectral collocation method for the Stokes problem, *Computers & Fluids* **8**: 825–840.

Pilitsis, S. and Beris, A. N. (1989). Calculation of steady-state viscoelastic flow in an undulating tube, *Journal of Non-Newtonian Fluid Mechanics* **31**: 231–287.

Pilitsis, S. and Beris, A. N. (1991). Viscoelastic flow in an undulating tube. Part II. Effects of high elasticity, large amplitude of undulation and inertia, *Journal of Non-Newtonian Fluid Mechanics* **39**: 375–405.

Pilitsis, S. and Beris, A. N. (1992). Pseudospectral calculations of viscoelastic flow in a periodically constricted tube, *Computer Methods in Applied Mechanics and Engineering* **98 (3)**: 307–328.

Poggio, T. and Girosi, F. (1990). Networks for approximation and learning, *Proceedings of the IEEE* **78 (9)**: 1481–1497.

Powell, M. J. D. (1988). Radial basis function approximation to polynomials, *Numerical Analysis 1987 proceeding* pp. 223–441.

Quéré, P. L. (1991). Accuracy solutions to the square thermally driven cavity at high Rayleigh number, *Computers and Fluids* **20**: 29–41.

Rahaim, C. P. and Kassab, A. J. (1996). Pressure correction DRBEM solution for heat transfer and fluid flow in incompressible viscous flow, *Engineering Analysis with Boundary Elements* **18**: 265–272.

Rajagopalan, D., Armstrong, R. C. and Brown, R. A. (1990). Finite element methods for calculation of steady, viscoelastic flow using constitutive equations with a Newtonian viscosity, *Journal of Non-Newtonian Fluid Mechanics* **36**: 159–192.

Reddy, J. and Gartling, D. (1994). *The Finite Element Method in Heat Transfer and Fluid Dynamics*, CRC Press, USA.

Roache, P. J. (1982). *Computational Fluid Dynamics*, Hermosa Publishers, Albuquerque, New Mexico.

Sadat, H. and Couturier, S. (2000). Performance and accuracy of meshless method for laminar natural convection, *Numerical Heat Transfer, Part B* **37**: 455–467.

Saitoh, T. and Hirose, K. (1989). High-accuracy benchmark solutions to natural convection in a square cavity, *Computation Mechanics* **4**: 417–427.

Šarler, B. (2005). A Radial Basis Function Collocation Approach in Computational Fluid Dynamics, *CMES: Computer Modeling in Engineering & Sciences* **7 (2)**: 185–193.

Šarler, B. (2007). From Global to Local Radial Basis Function Collocation Method for Transport Phenomena, *Advances in Meshfree Techniques* **5**: 257–282.

Šarler, B., Gobin, D., Goyeau, B., Perko, J. and Power, H. (2000). Natural convection in porous media-dual reciprocity boundary element method solution of the Darcy model, *International Journal for Numerical Methods in Fluids* **33 (2)**: 279–312.

Šarler, B., Perko, J. and Chen, C. S. (2004). Radial basis function collocation method solution of natural convection in porous media, *International Journal of Numerical Methods for Heat & Fluid Flow* **14 (2)**: 187–212.

Šarler, B., Perko, J., Chen, C. S. and Kuhn, G. (2001). A meshless approach to natural convection, *International Conference on Computational Engineering and Sciences -2001, CD-rom Proceedings*.

Šarler, B., Perko, J., Gobin, D., Goyeau, B. and Power, H. (2004). Dual reciprocity boundary element method solution of natural convection in Darcy–Brinkman porous media, *Engineering Analysis with Boundary Elements* **28**: 23–41.

Šarler, B. and Vertnik, R. (2006). Meshfree explicit local radial basis function collocation method for diffusion problems, *Computers & Mathematics with Applications* **51 (8)**: 1269–1282.

Sarra, S. A. (2006). Integrated Multiquadric Radial Basis Function Approximation Methods, *Computers and Mathematics with Applications* **51**: 1283–1296.

Schaback, R. (1995). Error estimates and condition numbers for radial basis function interpolation, *Advances in Computational Mathematics* **3**: 251–264.

Selvadurai, A. P. S. (2000). *Partial Differential Equations in Mechanics 2: The Biharmonic Equation, Poisson's Equation*, Springer.

Selvadurai, A. P. S. (2002). The advective transport of a chemical from a cavity in a porous medium, *Computers and Geotechnics* **29 (7)**: 525–546.

Shu, C. (1999). Application of differential quadrature method to simulate natural convection in a concentric annulus, *International Journal of Numerical Method Fluids* **30**: 977–993.

Shu, C., Ding, H., Chen, H. Q. and Wang, T. G. (2005). An upwind local RBF-DQ method for simulation of inviscid compressible flows, *Computer Methods in Applied Mechanics and Engineering* **194**: 2001–2017.

Shu, C., Ding, H. and Yeo, K. (2003). Local radial basis function-based differential quadrature method and its application to solve two-dimensional incompressible Navier-Stokes equations, *Computer Methods in Applied Mechanics and Engineering* **192**: 941–954.

Shu, C. and Wu, Y. L. (2007). Integrated radial basis functions-based differential quadrature method and its performance, *International Journal of Numerical Method Fluids* **53**: 969–984.

Sladek, J., Sladek, V. and Atluri, S. (2004). Meshless local Petrov-Galerkin method for heat conduction problem in an anisotropic medium, *CMES: Computer Modeling in Engineering & Sciences* **6**: 309–318.

Sladek, J., Sladek, V., Hellmich, C. and Eberhardsteiner, J. (2007). Heat conduction analysis of 3D axisymmetric and anisotropic FGM bodies by meshless local Petrov-Galerkin method, *Computation Mechanics* **39**: 323–333.

Spotz, W. F. (1998). Accuracy and performance of numerical wall boundary conditions for steady, 2D, incompressible streamfunction vorticity, *International Journal of Numerical Methods Fluid* **28**: 737–757.

Stevens, D., Power, H., Lees, M. and Morvan, H. (2009). The use of PDE centres in the local RBF Hermitian method for 3D convective-diffusion problems, *Journal of Computational Physics* **228 (12)**: 4606–4624.

Szady, M. J., Salamon, T. R., Liu, A. W., Bornside, D. E. and Armstrong, R. C. (1995). A new mixed finite element method for viscoelastic flows governed by differential constitutive equations, *Journal of Non-Newtonian Fluid Mechanic* **59**: 215–243.

Tanner, R. I. and Xue, S.-C. (2002). Computing transient flows with high elasticity, *Korea-Australia Rheology Journal* **14**: 143–159.

Tran-Canh, D. and Tran-Cong, T. (2002). Computation of viscoelastic flow using neural networks and stochastic simulation, *Korea-Australia Rheology Journal* **14 (4)**: 161–174.

Tran-Cong, T., Mai-Duy, N. and Phan-Thien, N. (2002). BEM-RBF approach for viscoelastic flow analysis, *Engineering Analysis with Boundary Elements* **26 (9)**: 757–762.

Vertnik, R. and Šarler, B. (2006). Meshless local radial basis function collocation method for convective-diffusive solid-liquid phase change problems, *International Journal of Numerical Methods for Heat & Fluid Flow* **16 (5)**: 617–640.

Vertnik, R., Založnik, M. and Šarler, B. (2006). Solution of transient direct-chill aluminium billet casting problem with simultaneous material and interphase moving boundaries by a meshless method, *Engineering Analysis with Boundary Elements* **30 (10)**: 847–855.

Wan, D. C., Patnail, B. S. V. and Wei, G. W. (2001). A new benchmark quality solution for the buoyancy-driven cavity by discrete singular convolution, *Numerical Heat Transfer, Part B* **40**: 199–228.

Weinan, E. and Liu, J.-G. (1996). Vorticity boundary condition and related issues for finite difference schemes, *Journal of Computational Physics* **124**: 368–382.

Wendland, H. (1995). Piecewise polynomial, positive definite and compactly supported radial functions of minimal degree, *Advances in Computational Mathematics* **4 (1)**: 389–396.

Wendland, H. (1999). Meshless Galerkin methods using radial basis functions, *Mathematics of Computation* **68**: 1521–1531.

Wright, G. and Fornberg, B. (2006). Scattered node compact finite difference-type formulas generated from radial basis functions, *Journal of Computational Physics* **212**: 99–123.

Wu, Y. L. and Liu, G. R. (2003). A meshfree formulation of local radial point interpolation method (LRPIM) for incompressible flow simulation, *Computational Mechanics* **30**: 355–365.

Wu, Z. (1995). Compactly supported positive definite radial functions, *Advances in Computational Mathematics* **4**: 283–292.

Xue, S. C., Phan-Thien, N. and Tanner, R. I. (1995). Numerical study of secondary flows of viscoelastic fluid in strait pipes by an implicit finite volume method, *Journal of Non-Newtonian Fluid Mechanic* **59**: 191–213.

Yao, G., Islam, S. and Šarler, B. (2010). A Comparative Study of Global and Local Meshless Methods for Diffusion-Reaction Equation, *CMES: Computer Modeling in Engineering & Sciences* **59 (2)**: 127–154.

Zheng, R., Phan-Thien, N., Tanner, R. I. and Bush, M. B. (1990). Numerical analysis of viscoelastic flow through a sinusoidally corrugated tube using a boundary element method, *Journal of Rheology* **34 (1)**: 79–102.

Zhou, X., Hon, Y. C. and Li, J. (2003). Overlapping domain decomposition method by radial basis functions, *Applied Numerical Mathematics* **44 (1-2)**: 241–255.

Zienkiewicz, O. C. and Taylor, R. L. (1991). *The Finite Element Method*, McGraw-Hill, London.